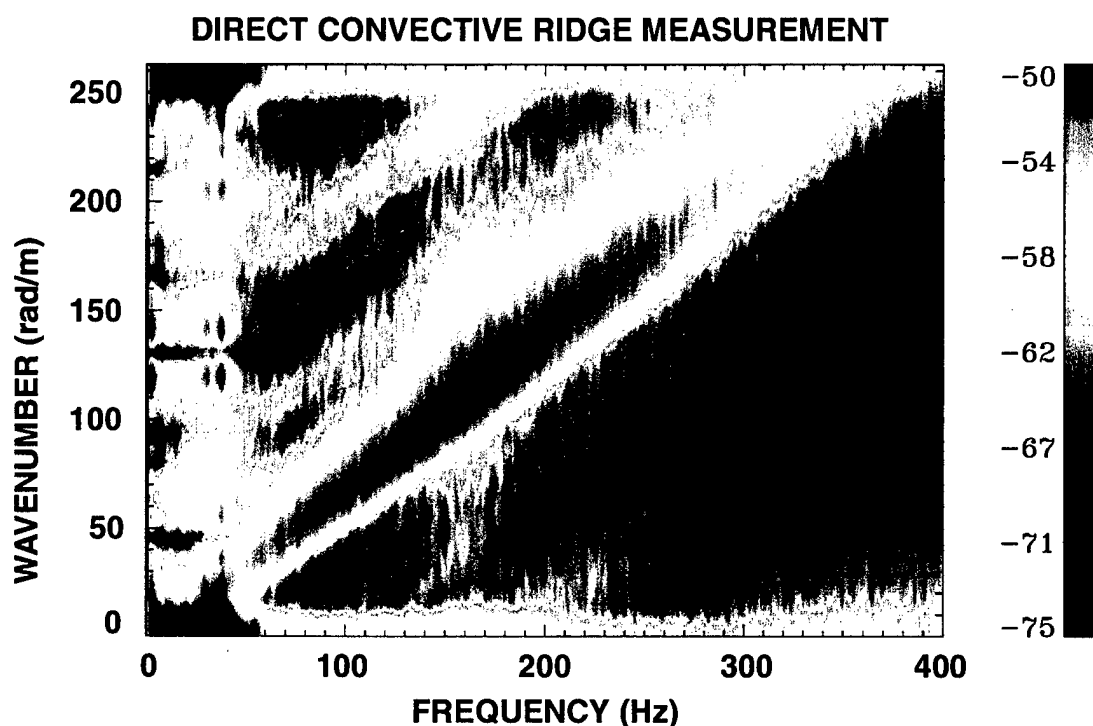


Direct Measurement of the Mode 0 Turbulent Boundary Layer Wall Pressure and Wall Shear Stress Spectra Using Air-Backed and Oil-Filled Multichannel Wavenumber Filters

Mark S. Peloquin
Submarine Sonar Department



**Naval Undersea Warfare Center Division
Newport, Rhode Island**

Approved for public release; distribution is unlimited.

DTIC QUALITY INSPECTED 2

19991213 087

REPORT DOCUMENTATION PAGE

Form Approved
OMB No. 0704-0188

Public reporting for this collection of information is estimated to average 1 hour per response, including the time for reviewing instructions, searching existing data sources, gathering and maintaining the data needed, and completing and reviewing the collection of information. Send comments regarding this burden estimate or any other aspect of this collection of information, including suggestions for reducing this burden, to Washington Headquarters Services, Directorate for Information Operations and Reports, 1215 Jefferson Davis Highway, Suite 1204, Arlington, VA 22202-4302, and to the Office of Management and Budget, Paperwork Reduction Project (0704-0188), Washington, DC 20503.

1. AGENCY USE ONLY (Leave blank)		2. REPORT DATE 10 May 1999		3. REPORT TYPE AND DATES COVERED Final	
4. TITLE AND SUBTITLE Direct Measurement of the Mode 0 Turbulent Boundary Layer Wall Pressure and Wall Shear Stress Spectra Using Air-Backed and Oil-Filled Multichannel Wavenumber Filters				5. FUNDING NUMBERS PE 0602314N	
6. AUTHOR(S) Mark S. Peloquin					
7. PERFORMING ORGANIZATION NAME(S) AND ADDRESS(ES) Naval Undersea Warfare Center Division 1176 Howell Street Newport, RI 02841-1708				8. PERFORMING ORGANIZATION REPORT NUMBER TR 11,012	
9. SPONSORING/MONITORING AGENCY NAME(S) AND ADDRESS(ES) Office of Naval Research 800 North Quincy Street Arlington, VA 22217-5000				10. SPONSORING/MONITORING AGENCY REPORT NUMBER	
11. SUPPLEMENTARY NOTES					
12a. DISTRIBUTION/AVAILABILITY STATEMENT Approved for public release; distribution is unlimited.				12b. DISTRIBUTION CODE	
13. ABSTRACT (Maximum 200 words) This report describes research that resulted in the first direct multichannel measurements of the wall pressure and wall shear stress spectra beneath a turbulent boundary layer formed over a long, thin cylinder in an axial flow field. These measurements, processed as wavenumber-frequency spectra, were made with a multichannel array composed of an air-backed cylinder structure and a 32-channel aperture of PVDF film sensors having an axisymmetric response with respect to the array circumference. The measurements resolve the wavenumber spectrum in the ± 131 -rad/m range. Unexpected results were observed at a 5-knot freestream flow speed, where the magnitude of the wall shear stress convective ridge level exceeded the magnitude of the wall pressure convective ridge level. From 10 to 20 knots, the traditional relationship was observed, in which the wall pressure magnitude exceeds the wall shear stress magnitude in the vicinity of the convective ridge. Additionally, accurate resolution of the shape of the convective ridge as a function of wavenumber was accomplished with the air-backed cylinder array. An experimental calibration of the "hose transfer function" for pressure was obtained by using data from an array of ceramic hydrophones mounted interior to an oil-filled cylinder in unison with data from the air-backed cylinder array. Theoretical dynamic elasticity simulations were required to remove the effects of the surface-generated pressure fields, which were different for each structure. Previous to this research, a mathematical model of the hose transfer function was used without the aid of experimental data or verification of any kind. The oil-filled array measurements spanned the wavenumber spectrum in the ± 206 -rad/m range and included measurements at $k = 0$ that were free from acoustic contamination.					
14. SUBJECT TERMS Flow Noise Reduction Passive Sonar Turbulent Wall Pressure Wavenumber Filters Hull Arrays Submarine Sonar Turbulent Wall Shear Stress					15. NUMBER OF PAGES 162
					16. PRICE CODE
17. SECURITY CLASSIFICATION OF REPORT Unclassified	18. SECURITY CLASSIFICATION OF THIS PAGE Unclassified	19. SECURITY CLASSIFICATION OF ABSTRACT Unclassified	20. LIMITATION OF ABSTRACT SAR		

TABLE OF CONTENTS

	Page
LIST OF ILLUSTRATIONS	iv
LIST OF TABLES	x
INTRODUCTION	1
TOWED ARRAY MODELING OVERVIEW	3
EXPERIMENT DESIGN.....	5
Regions of Direct Measurement—Partition of the k, ω Plane	5
Tailored Structural Responses.....	7
Sensitivity of PVDF Film/Stiff Elastic Air-Backed Cylinder.....	8
Sensitivity to Wall Pressure and Longitudinal Wall Shear Stress	11
Experimental Test Configuration	16
Air-Backed Cylinder	17
High-Wavenumber Aperture	17
Oil-Filled Cylinder.....	18
High-Wavenumber Aperture	18
Medium-Wavenumber Aperture	19
Low-Wavenumber Aperture.....	19
CALIBRATIONS.....	21
Frequency Calibration.....	21
Broadside Calibration ($k = 0$).....	21
Air-Backed Cylinder	21
Oil-Filled Cylinders	22
Wavenumber Calibration	23
Anechoic Chamber (Air Endfire).....	23
Theoretical Field Calibration (k, ω) Plane	27
Assumptions and Limitations	27
Pressure Field Components.....	29
Surface-Generated Pressure	29
Corrected Pressure	29

TABLE OF CONTENTS (Cont'd)

	Page
Inner Pressure.....	35
EXPERIMENTAL RAW DATA	39
Air-Backed Cylinder	39
Oil-Filled Cylinder.....	39
CALIBRATED DATA FROM DIRECT TURBULENT BOUNDARY	
LAYER PRESSURE FIELD MEASUREMENTS.....	55
Low-Wavenumber Oil-Filled Cylinder Data.....	55
Comparison of Wavenumber Filters—Spectral Levels	55
Comparison of Convective Ridge and Low-Wavenumber Levels	58
Convective Ridge Levels.....	60
HOSE WALL TRANSFER FUNCTION CALIBRATION.....	69
SELF-NOISE MODEL PREDICTIONS USING EXISTING	
TURBULENCE SOURCE MODEL	73
Comparison of Experimental Data and Model Predictions (Air-	
Backed Cylinder)	73
20 Knots	73
Wall Pressure Excitation.....	73
Shear Stress Excitation	76
10 Knots	80
Wall Pressure Excitation	80
Shear Stress Excitation	83
5 Knots	87
Wall Pressure Excitation	87
Shear Stress Excitation	90
Comparison of Experimental Data and Model Predictions (Oil-	
Filled Cylinder).....	94
20-Knot Freestream Velocity	99
Wall Pressure Excitation	99
Shear Stress Excitation	104

TABLE OF CONTENTS (Cont'd)

	Page
10-Knot Freestream Velocity	110
Wall Pressure Excitation	110
Shear Stress Excitation	116
5-Knot Freestream Velocity	121
Wall Pressure Excitation	121
Shear Stress Excitation	126
CONCLUSIONS.....	131
RECOMMENDATIONS FOR FUTURE RESEARCH	135
REFERENCES	137
APPENDIX A—FREQUENCY CALIBRATIONS	A-1
APPENDIX B— WAVENUMBER CALIBRATIONS.....	B-1

LIST OF ILLUSTRATIONS

Figure		Page
1	Partition of the Wavenumber-Frequency Plane	5
2	Three-Dimensional Representation of the TBL Wavenumber-Frequency Surface from Figure 1	6
3	Tailored Structural Responses of the OFC and ABC	7
4	ABC/PVDF Sensitivity to a Wall Pressure Excitation Normalized by -225.8 dB (Magnitude = dB)	13
5	ABC/PVDF Sensitivity to a Longitudinal Wall Shear Stress Excitation Normalized by -225.8 dB (Magnitude = dB)	13
6	Comparison of ABC/PVDF Beamformed Response Surfaces for Radial and Longitudinal Excitations at 9.3 m/sec (Magnitude = $10 \log(P_o)^2$ re $\mu\text{Pa}^2/\text{Hz}/\text{rad}/\text{m}$)	14
7	Comparison of ABC/PVDF Beamformed Response Surfaces at a Frequency Cut of 50 Hz (Magnitude = $10 \log(P_o)^2$ re $\mu\text{Pa}^2/\text{Hz}/\text{rad}/\text{m}$)	15
8	Experimental Test Configuration for All Wavenumber Filters	16
9	ABC/PVDF Absolute Sensitivity to Wall Pressure Excitation (Magnitude = dB re $\text{volt}^2/\mu\text{Pa}^2$)	25
10	Cut in Frequency at 450 Hz for Figure 9 Showing ABC/PVDF Absolute Sensitivity to Wall Pressure Excitation (Magnitude = dB re $\text{volt}^2/\mu\text{Pa}^2$)	26
11	Signal Path Within the ABC Structure	28
12	OFC Surface-Generated Pressure Field at $r = 0.327$ in. (Magnitude = $10 \log(P_s(r)/P_o)^2$)	31
13	ABC Surface-Generated Pressure Field at $r = 0.327$ in. (Magnitude = $10 \log(P_s(r)/P_o)^2$)	31
14	Cut in Frequency for Figures 12 and 13 Showing Surface-Generated Pressure Field Comparison at $r = 0.327$ in. and $f = 100$ Hz (Magnitude = $10 \log(P_s(r)/P_o)^2$)	32
15	Theoretical Field Correction Surface for the ABC Normalization Constant of -14.2 dB at $f = 200$ Hz and $k = 0$ rad/m (Magnitude = dB re Equation (20))	33
16	Cuts Through Figure 15 Showing Corrections to the Convective Ridge for Three Different Flow Speeds (Magnitude = dB)	34
17	Signal Path Across the OFC	35

LIST OF ILLUSTRATIONS (Cont'd)

Figure		Page
18	ABC Experimental Raw Data $P_o(k, \omega)$ at a 5-knot Flow Speed	41
19	ABC Experimental Raw Data $P_o(k, \omega)$ at a 10-knot Flow Speed	42
20	ABC Experimental Raw Data $P_o(k, \omega)$ at a 20-knot Flow Speed	43
21	OFC Experimental Raw Data $P_i(k, \omega)$ from the High- k Wavenumber Filter at a 5-knot Flow Speed.....	44
22	OFC Experimental Raw Data $P_i(k, \omega)$ from the High- k Wavenumber Filter at a 10-knot Flow Speed.....	45
23	OFC Experimental Raw Data $P_i(k, \omega)$ from the High- k Wavenumber Filter at a 20-knot Flow Speed.....	46
24	OFC Experimental Raw Data $P_i(k, \omega)$ from the Medium- k Wavenumber Filter at a 5-knot Flow Speed.....	47
25	OFC Experimental Raw Data $P_i(k, \omega)$ from the Medium- k Wavenumber Filter at a 10-knot Flow Speed.....	48
26	OFC Experimental Raw Data $P_i(k, \omega)$ from the Medium- k Wavenumber Filter at a 15-knot Flow Speed.....	49
27	OFC Experimental Raw Data $P_i(k, \omega)$ from the Medium- k Wavenumber Filter at a 20-knot Flow Speed.....	50
28	OFC Experimental Raw Data $P_i(k, \omega)$ from the Medium- k Wavenumber Filter at a 25-knot Flow Speed.....	51
29	OFC Medium- k Wavenumber-Filter Frequency Cut from Figure 24 at 9.16 Hz and a 5-knot Flow Speed for Uncorrected Surface-Generated Pressure Effects (Magnitude = $10 \log(P_i^2)$ re $\mu\text{Pa}^2/\text{Hz}/\text{rad}/\text{m}$)	52
30	OFC Experimental Raw Data $P_i(k, \omega)$ from the Medium- k Wavenumber Filter at a 20-knot Flow Speed Showing the Dual Convective Ridge (Color Image).....	53
31	OFC Experimental Raw Data $P_i(k, \omega)$ from the Medium- k Wavenumber Filter at a 20-knot Flow Speed Showing the Dual Convective Ridge (Wire Frame)	54
32	Comparison of OFC Low-Wavenumber Pressure Levels from Wavenumber Filters at a 20-knot Flow Speed (Magnitude = $10 \log(P_i^2)$ re $\mu\text{Pa}^2/\text{Hz}/\text{rad}/\text{m}$)	57
33	Comparison of OFC Low-Wavenumber Pressure Levels and ABC Convective Ridge Levels from Wavenumber Filters at a 20-knot Flow Speed	

LIST OF ILLUSTRATIONS (Cont'd)

Figure	Page
(OFC Magnitude = $10 \log(P_i^2)$ re $\mu\text{Pa}^2/\text{Hz}/\text{rad}/\text{m}$ and ABC Magnitude = $10 \log(P_o^2)$ re $\mu\text{Pa}^2/\text{Hz}/\text{rad}/\text{m}$)	59
34 ABC Calibrated Pressure Level at a Flow Speed of 20 knots (Magnitude = $10 \log(P_o^2)$ re $\mu\text{Pa}^2/\text{Hz}/\text{rad}/\text{m}$)	61
35 Comparison of Fully Calibrated Convective Ridge Pressure Levels at Various Flow Speeds (Magnitude = $10 \log(P_o^2)$ re $\mu\text{Pa}^2/\text{Hz}/\text{rad}/\text{m}$)	62
36 Comparison of Fully Calibrated Convective Ridge Pressure Levels for the Wall Pressure Component Only (Magnitude = $10 \log(P_o^2)$ re $\mu\text{Pa}^2/\text{Hz}/\text{rad}/\text{m}$)	63
37 Cut in Frequency at 44 Hz for Fully Calibrated Wall Pressure Component at a 5-knot Flow Speed (Magnitude = $10 \log(P_o^2)$ re $\mu\text{Pa}^2/\text{Hz}/\text{rad}/\text{m}$)	64
38 Cut in Frequency at 45 Hz for Fully Calibrated Wall Pressure Component at a 10-knot Flow Speed (Magnitude = $10 \log(P_o^2)$ re $\mu\text{Pa}^2/\text{Hz}/\text{rad}/\text{m}$)	65
39 Cut in Frequency at 59 Hz for Fully Calibrated Wall Pressure Component at a 15-knot Flow Speed (Magnitude = $10 \log(P_o^2)$ re $\mu\text{Pa}^2/\text{Hz}/\text{rad}/\text{m}$)	66
40 Cut in Frequency at 94 Hz for Fully Calibrated Wall Pressure Component at a 20-knot Flow Speed (Magnitude = $10 \log(P_o^2)$ re $\mu\text{Pa}^2/\text{Hz}/\text{rad}/\text{m}$)	67
41 Outer (ABC) and Inner (OFC) Corrected Pressure Levels Used for the Hose Transfer Function Calibration, with Cuts Through the Surfaces at 100 Hz (Magnitude = $10 \log(P^2)$ re $\mu\text{Pa}^2/\text{Hz}/\text{rad}/\text{m}$, Where $P = P_o$ and P_i for the Outer and Inner Pressure Fields, Respectively)	71
42 Comparison of Experimental and Theoretical Hose Transfer Function Calibrations at 8.2 m/sec Using the Bending Shell and Elasticity Models (Magnitude = $10 \log(P_i / P_o)^2$)	72
43 Comparison of Experimental Data $P_o(k, \omega)$ and Wall Pressure Simulation at a Flow Speed of 10.11 m/sec	74
44 Convective Ridge Magnitude Comparison of Experimental Data and Wall Pressure Simulation at a Flow Speed of 10.11 m/sec (Magnitude = $10 \log(P_o(k, \omega)^2)$ re $\mu\text{Pa}^2/\text{Hz}/\text{rad}/\text{m}$)	75
45 Comparison of Experimental Data $P_o(k, \omega)$ and Wall Shear Stress Simulation at a Flow Speed of 10.11 m/sec	77
46 Convective Ridge Magnitude Comparison of Experimental Data and Wall Shear Stress Simulation at a Flow Speed of 10.11 m/sec (Magnitude = $10 \log(P_o(k, \omega)^2)$ re $\mu\text{Pa}^2/\text{Hz}/\text{rad}/\text{m}$)	78

LIST OF ILLUSTRATIONS (Cont'd)

Figure	Page
47 Convective Ridge Magnitude Comparison of Experimental Data with Wall Pressure and Wall Shear Stress Simulations at a Flow Speed of 10.11 m/sec (Magnitude = $10 \log(P_o(k, \omega)^2)$ re $\mu\text{Pa}^2/\text{Hz}/\text{rad}/\text{m}$)	79
48 Comparison of Experimental Data $P_o(k, \omega)$ and Wall Pressure Simulation at a Flow Speed of 5.26 m/sec	81
49 Convective Ridge Magnitude Comparison of Experimental Data and Wall Pressure Simulation at a Flow Speed of 5.26 m/sec (Magnitude = $10 \log(P_o(k, \omega)^2)$ re $\mu\text{Pa}^2/\text{Hz}/\text{rad}/\text{m}$)	82
50 Comparison of Experimental Data $P_o(k, \omega)$ and Wall Shear Stress Simulation at a Flow Speed of 5.26 m/sec	84
51 Convective Ridge Magnitude Comparison of Experimental Data and Wall Shear Stress Simulation at a Flow Speed of 5.26 m/sec (Magnitude = $10 \log(P_o(k, \omega)^2)$ re $\mu\text{Pa}^2/\text{Hz}/\text{rad}/\text{m}$)	85
52 Convective Ridge Magnitude Comparison of Experimental Data with Wall Pressure and Wall Shear Stress Simulations at a Flow Speed of 5.26 m/sec (Magnitude = $10 \log(P_o(k, \omega)^2)$ re $\mu\text{Pa}^2/\text{Hz}/\text{rad}/\text{m}$)	86
53 Comparison of Experimental Data $P_o(k, \omega)$ and Wall Pressure Simulation at a Flow Speed of 2.62 m/sec	88
54 Convective Ridge Magnitude Comparison of Experimental Data and Wall Pressure Simulation at a Flow Speed of 2.62 m/sec (Magnitude = $10 \log(P_o(k, \omega)^2)$ re $\mu\text{Pa}^2/\text{Hz}/\text{rad}/\text{m}$)	89
55 Comparison of Experimental Data $P_o(k, \omega)$ and Wall Shear Stress Simulation at a Flow Speed of 2.62 m/sec	91
56 Convective Ridge Magnitude Comparison of Experimental Data and Wall Shear Stress Simulation at a Flow Speed of 2.62 m/sec (Magnitude = $10 \log(P_o(k, \omega)^2)$ re $\mu\text{Pa}^2/\text{Hz}/\text{rad}/\text{m}$)	92
57 Convective Ridge Magnitude Comparison of Experimental Data with Wall Pressure and Wall Shear Stress Simulations at a Flow Speed of 2.62 m/sec (Magnitude = $10 \log(P_o(k, \omega)^2)$ re $\mu\text{Pa}^2/\text{Hz}/\text{rad}/\text{m}$)	93
58 High- k Array Beamformed Surface Simulation of the Inner Pressure $P_i(k, \omega)$ Using the Bending Shell and Elasticity Models at a Flow Speed of 8.9 m/sec	96
59 Comparison of the Elasticity and Bending Shell Models from Figure 58 at 246 Hz (Magnitude = $10 \log(P_i(k, \omega)^2)$ re $\mu\text{Pa}^2/\text{Hz}/\text{rad}/\text{m}$)	97

LIST OF ILLUSTRATIONS (Cont'd)

Figure	Page
60 Comparison of the Elasticity and Bending Shell Models from Figure 58 at -215 m/sec (Magnitude = $10 \log(P_i(k, \omega)^2) \text{ re } \mu\text{Pa}^2/\text{Hz/rad/m}$)	98
61 Comparison of Experimental Data $P_i(k, \omega)$ and Model Simulation Using a Wall Pressure Excitation at a Flow Speed of 10.3 m/sec	101
62 Comparison of Levels in Figure 61 at 204 Hz and a Flow Speed of 10.3 m/sec (Magnitude = $10 \log(P_i(k, \omega)^2) \text{ re } \mu\text{Pa}^2/\text{Hz/rad/m}$)	102
63 Convective Ridge Magnitude Comparison of Experimental Data and Bending Shell Model Simulation from Figure 61 at a Convective Velocity of 9.5 m/sec (Magnitude = $10 \log(P_i(k, \omega)^2) \text{ re } \mu\text{Pa}^2/\text{Hz/rad/m}$)	103
64 Comparison of Experimental Data $P_i(k, \omega)$ and Model Simulation Using a Longitudinal Shear Stress Excitation at a Flow Speed of 10.3 m/sec	106
65 Comparison of Levels in Figure 64 at 204 Hz and a Flow Speed of 10.3 m/sec (Magnitude = $10 \log(P_i(k, \omega)^2) \text{ re } \mu\text{Pa}^2/\text{Hz/rad/m}$)	107
66 Convective Ridge Magnitude Comparison of Experimental Data and Bending Shell Model Simulation from Figure 64 at a Convective Velocity of 9.5 m/sec (Magnitude = $10 \log(P_i(k, \omega)^2) \text{ re } \mu\text{Pa}^2/\text{Hz/rad/m}$)	108
67 Extensional Wave Magnitude Comparison of Experimental Data and Bending Shell Model Simulation from Figure 64 with a Beam Cut at 775 m/sec (Magnitude = $10 \log(P_i(k, \omega)^2) \text{ re } \mu\text{Pa}^2/\text{Hz/rad/m}$)	109
68 Comparison of Experimental Data $P_i(k, \omega)$ and Model Simulation Using a Wall Pressure Excitation at a Flow Speed of 4.9 m/sec	111
69 Comparison of Levels in Figure 68 at 84 Hz and a Flow Speed of 4.9 m/sec (Magnitude = $10 \log(P_i(k, \omega)^2) \text{ re } \mu\text{Pa}^2/\text{Hz/rad/m}$)	112
70 Comparison of Levels in Figure 68 at 345 Hz and a Flow Speed of 4.9 m/sec (Magnitude = $10 \log(P_i(k, \omega)^2) \text{ re } \mu\text{Pa}^2/\text{Hz/rad/m}$)	113
71 Comparison of Levels in Figure 68 at 445 Hz and a Flow Speed of 4.9 m/sec (Magnitude = $10 \log(P_i(k, \omega)^2) \text{ re } \mu\text{Pa}^2/\text{Hz/rad/m}$)	114
72 Convective Ridge Magnitude Comparison of Experimental Data and Bending Shell Model Simulation from Figure 68 at a Convective Velocity of 4.5 m/sec (Magnitude = $10 \log(P_i(k, \omega)^2) \text{ re } \mu\text{Pa}^2/\text{Hz/rad/m}$)	115
73 Comparison of Experimental Data $P_i(k, \omega)$ and Model Simulation Using a Longitudinal Shear Stress Excitation at a Flow Speed of 4.9 m/sec	117

LIST OF ILLUSTRATIONS (Cont'd)

Figure	Page
74 Comparison of Levels in Figure 73 at 445 Hz and a Flow Speed of 4.9 m/sec (Magnitude = $10 \log(P_i(k, \omega)^2) \text{ re } \mu\text{Pa}^2/\text{Hz/rad/m}$)	118
75 Convective Ridge Magnitude Comparison of Experimental Data and Bending Shell Model Simulation from Figure 73 at a Convective Velocity of 4.5 m/sec (Magnitude = $10 \log(P_i(k, \omega)^2) \text{ re } \mu\text{Pa}^2/\text{Hz/rad/m}$)	119
76 Extensional Wave Magnitude Comparison of Experimental Data and Bending Shell Model Simulation from Figure 73 with a Beam Cut at 775 m/sec (Magnitude = $10 \log(P_i(k, \omega)^2) \text{ re } \mu\text{Pa}^2/\text{Hz/rad/m}$)	120
77 Comparison of Experimental Data $P_i(k, \omega)$ and Model Simulation Using a Wall Pressure Excitation at a Flow Speed of 2.5 m/sec	121
78 Comparison of Levels in Figure 77 at 117 Hz and a Flow Speed of 2.5 m/sec (Magnitude = $10 \log(P_i(k, \omega)^2) \text{ re } \mu\text{Pa}^2/\text{Hz/rad/m}$)	122
79 Comparison of Levels in Figure 77 at 245 Hz and a Flow Speed of 2.5 m/sec (Magnitude = $10 \log(P_i(k, \omega)^2) \text{ re } \mu\text{Pa}^2/\text{Hz/rad/m}$)	123
80 Comparison of Levels in Figure 77 at 345 Hz and a Flow Speed of 2.5 m/sec (Magnitude = $10 \log(P_i(k, \omega)^2) \text{ re } \mu\text{Pa}^2/\text{Hz/rad/m}$)	124
81 Comparison of Levels in Figure 77 at 445 Hz and a Flow Speed of 2.5 m/sec (Magnitude = $10 \log(P_i(k, \omega)^2) \text{ re } \mu\text{Pa}^2/\text{Hz/rad/m}$)	125
82 Comparison of Experimental Data $P_i(k, \omega)$ and Model Simulation Using a Longitudinal Shear Stress Excitation at a Flow Speed of 2.5 m/sec	127
83 Comparison of Levels in Figure 82 at 445 Hz and a Flow Speed of 2.5 m/sec (Magnitude = $10 \log(P_i(k, \omega)^2) \text{ re } \mu\text{Pa}^2/\text{Hz/rad/m}$)	128
84 Convective Ridge Magnitude Comparison of Experimental Data and Bending Shell Model Simulation from Figure 82 at a Convective Velocity of 2.3 m/sec (Magnitude = $10 \log(P_i(k, \omega)^2) \text{ re } \mu\text{Pa}^2/\text{Hz/rad/m}$)	129
85 Extensional Wave Magnitude Comparison of Experimental Data and Bending Shell Model Simulation from Figure 82 with a Beam Cut at 775 m/sec (Magnitude = $10 \log(P_i(k, \omega)^2) \text{ re } \mu\text{Pa}^2/\text{Hz/rad/m}$)	130
A-1 Signal Amplification Diagram.....	A-1

LIST OF TABLES

Table	Page
1 Piezo Film Constants.....	8
2 Piezo Film Geometry.....	8
3 Sensor Calibration Files	22
4 Sensor Aperture Corrections for Spectral Level Normalization	55
A-1 ABC Calibrations at Dodge Pond	A-2
A-2 ABC Calibrations in the Anechoic Chamber	A-3
A-3 Calibrations of OFC Single-Channel Hydrophone (EDO) at Dodge Pond.....	A-4
A-4 Calibrations of OFC Medium- k Array at Dodge Pond.....	A-5
A-5 Calibrations of OFC High- k Array at Dodge Pond	A-6
B-1 Comparison of Endfire and Broadside Measurements in the Anechoic Chamber for the ABC Array	B-1
B-2 Sensitivity of an Acoustic Plane Wave Arrival Angle (35 degrees) Measured in the Anechoic Chamber for the ABC Array	B-1

DIRECT MEASUREMENT OF THE MODE 0 TURBULENT BOUNDARY LAYER WALL PRESSURE AND WALL SHEAR STRESS SPECTRA USING AIR-BACKED AND OIL-FILLED MULTICHANNEL WAVENUMBER FILTERS

INTRODUCTION

This research has resulted in direct measurements of the wall pressure and wall shear stress spectra existing beneath a turbulent boundary layer (TBL) that has formed over a long, thin cylinder in an axial flow field. The cylinder length-to-diameter ratio at the point where the measurements are made is 1600.

Separate and distinct mechanical structures are used to house the multichannel arrays that make the wall pressure measurements as a function of wavenumber and frequency. Each structure is designed to provide a transparent transfer function to wall pressure over its intended measurement range and to mechanically filter unwanted energy outside of its measurement range.

Accurate, unaliased measurements of the wall pressure spectra are made in the low-wavenumber region with two arrays, composed of 32 channels each, housed in oil-filled cylinders (OFCs). A single 56.6-foot-long hydrophone is used in a third OFC to provide a measure of the pressure fluctuations at a wavefront arrival angle parallel to the longitudinal axis of the array (broadside).

Wall pressure measurements of the convective ridge are made with a composite array constructed of a compliant air-backed cylinder (ABC) and bonded polyvinylidene fluoride (PVDF) piezo film sensors. This type of patented¹ array technology is the first of its kind to be employed for this use. Calibration of the ABC is accomplished in an experimental phase and in a theoretical phase, with the latter based on mathematical model predictions. It is necessary to base part of the calibration on mathematical model predictions because a wavenumber calibrator

capable of generating a pressure field of broadband wavenumber content does not yet exist.

The data from the OFC and the ABC arrays are used in unison to produce a calibration of the OFC's transfer function for pressure, otherwise known as the "hose transfer function." This is the first time that a calibration of the hose transfer function has been obtained. Previous to this research, a mathematical model of the hose transfer function was used (without experimental verification).

Finally, the experimental data for both the OFC and the ABC arrays are compared to theoretical predictions using currently available models for wall pressure and longitudinal wall shear stress. A careful analysis reveals that the ABC has measured longitudinal wall shear stress fluctuations at low wavenumbers and quite possibly wall shear stress fluctuations in the vicinity of the convective ridge at low freestream velocities, typically on the order of 5 m/sec. At freestream velocities greater than 5 m/sec, the ABC array has measured the wall pressure component of the TBL.

TOWED ARRAY MODELING OVERVIEW

The physical foundation for this research is based on an understanding of towed array self-noise modeling. Let us begin by stating the governing equations in order to organize the discussion and then move on to the advantages and disadvantages of employing the OFC and the ABC for measurements in the different regions of the wavenumber-frequency plane.

The integral equation for the beam level pressure measured by an array steered to a wavenumber, k_s , is given by equation (1) as

$$P_s^2(k_s, \omega) = \frac{1}{(Beamwidth)} \int_{-\infty}^{\infty} P_{TBL}^2(k, \omega) T^2(k, \omega) H^2(k) A^2(k - k_s) dk. \quad (1)$$

Throughout this report, pressure will be given in the form of a decibel normalized on a per-Hertz/per-radian/per-meter basis, with units of dB re $\mu\text{Pa}^2/\text{Hz}/\text{rad}/\text{m}$; therefore,

$$P_s^2(k_s, \omega) \rightarrow 10 \log(P_s^2(k_s, \omega)) . \quad (2)$$

The symbol ω is used instead of f to remain faithful to the nomenclature used at NUWC Division Newport, as well as to the references cited herein. If it is desirable to convert spectral level pressure $P_s^2(k_s, \omega)$ (given in this report) to beam level pressure $P_B^2(k_s, \omega)$, $10 \log(Beamwidth)$ is added as follows:

$$P_B^2(k_s, \omega) = P_s^2(k_s, \omega) + 10 \log(Beamwidth) . \quad (3)$$

In equation (1), $P_{TBL}^2(k, \omega)$ is the pressure induced by the TBL at the wall. The hydrophone wavenumber response, $H^2(k)$, is given by equation (4) as

$$H^2(k) = \left(\frac{\sin\left(\frac{kL}{2}\right)}{\frac{kL}{2}} \right)^2, \quad (4)$$

where L is the hydrophone length and k is the trace wavenumber impressed on the hydrophone.

The array response for N sensors steered to wavenumber k_s is

$$A^2(k - k_s) = \left(\frac{\sin\left(\frac{N(k - k_s)d}{2}\right)}{N \sin\left(\frac{(k - k_s)d}{2}\right)} \right)^2. \quad (5)$$

Additionally, the equation relating steered wavenumber k_s , angular frequency ω , and steered wave speed c_s is

$$k_s = \frac{\omega}{c_s}. \quad (6)$$

The magnitude of the mechanical structure transfer function, $T^2(k, \omega)$, will vary greatly, depending on whether the structure is the OFC or the ABC. This transfer function either acts as a lowpass resonant filter with respect to wavenumber (the case of the OFC) or as an all-pass resonant filter (the case of the ABC). Intelligent manipulation of $T^2(k, \omega)$ will facilitate the direct measurement of the wall pressure without the need for excessive correction due to unwanted filter effects.

The goal of this research is to obtain an accurate measurement of $P_{TBL}^2(k, \omega)$ in the wavenumber-frequency plane. Such measurements will enable the accuracy of current semi-empirical models to be assessed and eventually improved.

EXPERIMENT DESIGN

REGIONS OF DIRECT MEASUREMENT—PARTITION OF THE k, ω PLANE

Figure 1 depicts the major features of the wall pressure plane, $P_{TBL}^2(k, \omega)$. The convective ridge, indicated in red, is the region that will be measured principally by the ABC array. As seen in a later section, the ABC array also measures wall shear stress in the low-wavenumber region.

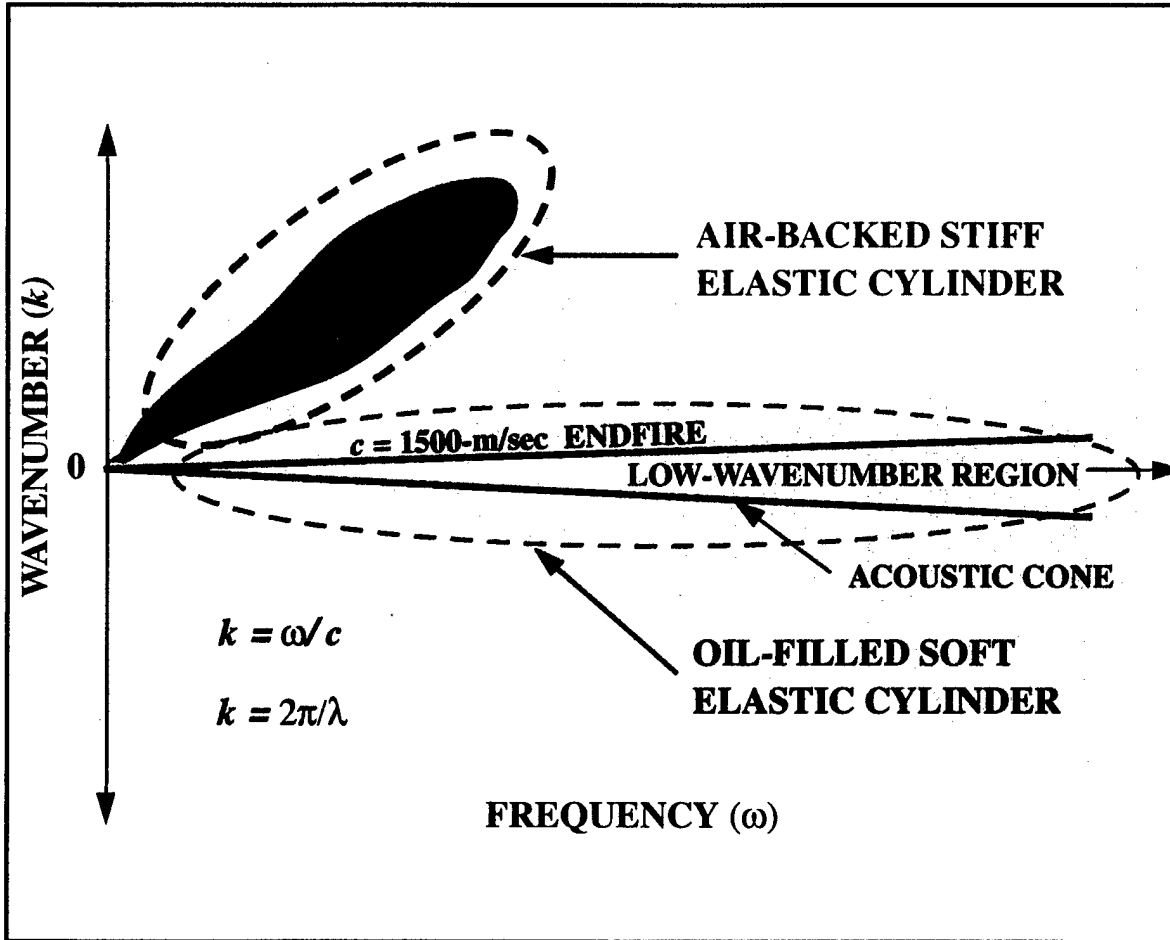


Figure 1. Partition of the Wavenumber-Frequency Plane

The OFC array provided direct measurement of the pressure fluctuations in the low-wavenumber region (marked in green), as well as a measurement across the entire plane. However, the magnitude of the pressure will be attenuated at the higher wavenumbers because of the wavenumber-filter effect of the compliant structure.

Figure 2, a color-shaded surface simulation of $P_{TBL}^2(k, \omega)$, illustrates the dynamic range of the pressure magnitude.

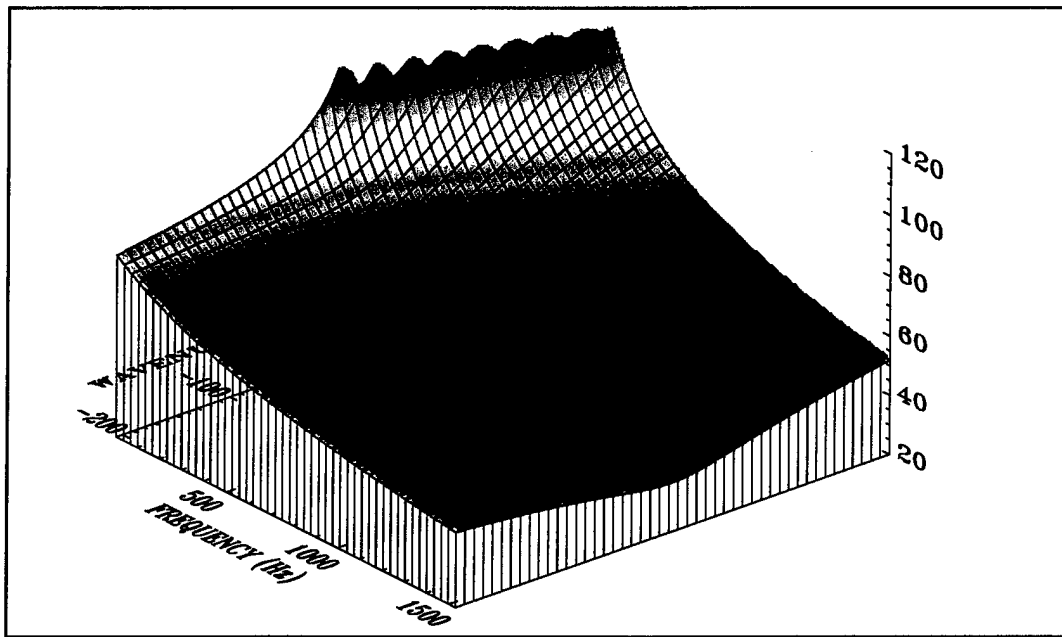


Figure 2. Three-Dimensional Representation of the TBL Wavenumber-Frequency Surface from Figure 1

Tailored Structural Responses

The mechanical structure transfer function, $T^2(k, \omega)$, is shown in figure 3 for the OFC and ABC used in this research. The surfaces in the figure are mathematical simulations, with the upper surface created from the model described in reference 2 (equation (92)). The lower surface was based on the model developed in reference 3, as well as on the theoretical development in the next section.

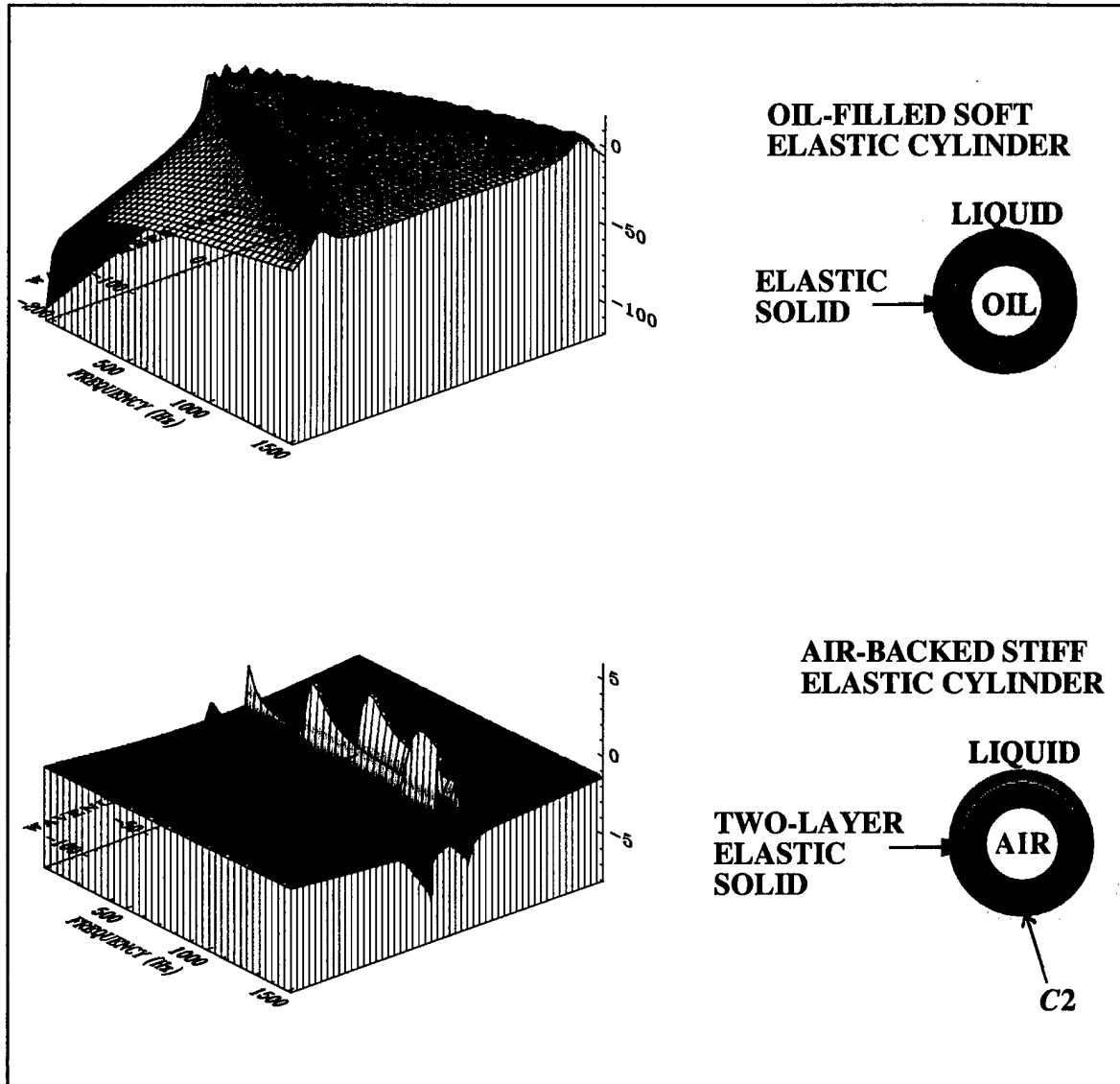


Figure 3. Tailored Structural Responses of the OFC and ABC

Sensitivity of PVDF Film/Stiff Elastic Air-Backed Cylinder. The sensors used for the ABC array are made of PVDF piezoelectric film, which generates a voltage when it is stressed along its three major axes. Table 1 lists the film constants for the sensor material used in these experiments, and table 2 describes the film geometry.

Table 1. Piezo Film Constants

Film Direction	Cylinder Axis	Piezo Constant V*m/N
1	θ	$g_{31} = 0.22$
2	x	$g_{32} = 0.02$
3	r	$g_{33} = -0.34$

Table 2. Piezo Film Geometry

	Property	Film Direction
Thickness	28.0×10^{-6} m	3
Width	0.45 inch	2
Length	1.57 inch	1
Area	0.71 inch^2	-

The piezo constants for the sensor provide the relationship for the ratio of voltage sensitivity to applied stress in a particular direction. The constants may be written as

$$g_{31} = 0.22 \frac{V}{\tau_{\theta\theta}}, \quad g_{32} = 0.02 \frac{V}{\tau_{xx}}, \quad g_{33} = -0.34 \frac{V}{\tau_{rr}}. \quad (7)$$

The mechanical transfer function characteristics of the ABC are modeled using $\tau_{\theta\theta}^{C1}/P_o$, τ_{xx}^{C1}/P_o , and τ_{rr}^{C1}/P_o from the theory derived in reference 4. For clarity, the equation for τ_{rr}^{C1}/P_o is reproduced here as

$$\begin{aligned} \frac{\tau_{rr}^{C1}(r_1)}{P_o} = & A_1^{C1} \left[(\lambda_1 + 2\mu_1) \frac{\partial^2}{\partial r^2} J_n(p_1 r_1) + \frac{\lambda_1}{r_1} \frac{\partial}{\partial r} J_n(p_1 r_1) - \lambda_1 J_n(p_1 r_1) \left(\frac{n^2}{r_1^2} + k^2 \right) \right] \\ & + A_2^{C1} \left[(\lambda_1 + 2\mu_1) \frac{\partial^2}{\partial r^2} Y_n(p_1 r_1) + \frac{\lambda_1}{r_1} \frac{\partial}{\partial r} Y_n(p_1 r_1) - \lambda_1 Y_n(p_1 r_1) \left(\frac{n^2}{r_1^2} + k^2 \right) \right] \\ & - B_1^{C1} \left[\frac{2\mu_1 n}{r_1^2} \left(J_n(q_1 r_1) - r_1 \frac{\partial}{\partial r} J_n(q_1 r_1) \right) \right] - B_2^{C1} \left[\frac{2\mu_1 n}{r_1^2} \left(Y_n(q_1 r_1) - r_1 \frac{\partial}{\partial r} Y_n(q_1 r_1) \right) \right] \\ & + C_1^{C1} 2\mu_1 i k \frac{\partial}{\partial r} J_{n+1}(q_1 r_1) + C_2^{C1} 2\mu_1 i k \frac{\partial}{\partial r} Y_{n+1}(q_1 r_1) . \end{aligned} \quad (8)$$

Expressions for $\tau_{\theta\theta}^{C1}/P_o$ and τ_{xx}^{C1}/P_o are derived in a similar fashion as

$$\begin{aligned} \frac{\tau_{\theta\theta}^{C1}(r_1)}{P_o} = & A_1^{C1} \left[\lambda_1 \frac{\partial^2}{\partial r^2} J_n(p_1 r_1) + \frac{\lambda_1 + 2\mu_1}{r_1} \frac{\partial}{\partial r} J_n(p_1 r_1) - \left(\frac{n^2}{r_1^2} (\lambda_1 + 2\mu_1) + k^2 \lambda_1 \right) J_n(p_1 r_1) \right] \\ & + A_2^{C1} \left[\lambda_1 \frac{\partial^2}{\partial r^2} Y_n(p_1 r_1) + \frac{\lambda_1 + 2\mu_1}{r_1} \frac{\partial}{\partial r} Y_n(p_1 r_1) - \left(\frac{n^2}{r_1^2} (\lambda_1 + 2\mu_1) + k^2 \lambda_1 \right) Y_n(p_1 r_1) \right] \\ & + B_1^{C1} \left[\frac{2\mu_1 n}{r_1^2} \left(J_n(q_1 r_1) - r_1 \frac{\partial}{\partial r} J_n(q_1 r_1) \right) \right] + B_2^{C1} \left[\frac{2\mu_1 n}{r_1^2} \left(Y_n(q_1 r_1) - r_1 \frac{\partial}{\partial r} Y_n(q_1 r_1) \right) \right] \\ & + C_1^{C1} \frac{2\mu_1 i k}{r_1} (n-1) \frac{\partial}{\partial r} J_{n+1}(q_1 r_1) + C_2^{C1} \frac{2\mu_1 i k}{r_1} (n-1) \frac{\partial}{\partial r} Y_{n+1}(q_1 r_1) \end{aligned} \quad (9)$$

and

$$\begin{aligned}
\frac{\tau_{xx}^{C1}(r_1)}{P_o} = & A_1^{C1} \left[\lambda_1 \left(\frac{\partial^2}{\partial r^2} (J_n(p_1 r_1)) + \frac{1}{r_1} \frac{\partial}{\partial r} J_n(p_1 r_1) \right) - J_n(p_1 r_1) \left(\lambda_1 \frac{n^2}{r_1^2} + k^2 (\lambda_1 + 2\mu_1) \right) \right] \\
& + A_2^{C1} \left[\lambda_1 \left(\frac{\partial^2}{\partial r^2} (Y_n(p_1 r_1)) + \frac{1}{r_1} \frac{\partial}{\partial r} Y_n(p_1 r_1) \right) - Y_n(p_1 r_1) \left(\lambda_1 \frac{n^2}{r_1^2} + k^2 (\lambda_1 + 2\mu_1) \right) \right] \\
& - C_1^{C1} \left[ik2\mu_1 \left(\frac{\partial}{\partial r} J_{n+1}(q_1 r_1) + \left(\frac{n+1}{r_1} \right) J_{n+1}(q_1 r_1) \right) \right] \\
& - C_2^{C1} \left[ik2\mu_1 \left(\frac{\partial}{\partial r} Y_{n+1}(q_1 r_1) + \left(\frac{n+1}{r_1} \right) Y_{n+1}(q_1 r_1) \right) \right] .
\end{aligned} \tag{10}$$

Equations (7) through (10), along with the values in tables 1 and 2, are used in equation (11) to solve for the sensitivity of the ABC array to applied wall pressure P_o . Cylinder parameters entered into the FORTRAN algorithm used to generate the output presented in this report have units of pascals; the 1×10^{-6} term in equation (11) converts the units to $\text{volts}^2/\mu\text{Pa}^2$ as follows:

$$T_A^2(k, \omega) = (1 \times 10^{-6}) t \left(g_{31} \frac{\tau_{\theta\theta}^{C1}}{P_o} + g_{31} \frac{\tau_{xx}^{C1}}{P_o} + g_{31} \frac{\tau_{rr}^{C1}}{P_o} \right) . \tag{11}$$

When equation (11) is used in equation (1) for filtering the $P_{TBL}^2(k, \omega)$ surface, equation (11) will be normalized by its value at $f = 200.0$ Hz and $k = 0.0$ rad/m. This value, $T_A^2(0.0, 200.0)$, equals -225.8 dB for the compliant cylinder in these experiments. The properties of the cylinder are the same as those listed in tables 16, 17, and 18 of reference 3. The mechanical structure transfer function for self-noise analysis in equation (1) is then

$$T^2(k, \omega) = \frac{T_A^2(k, \omega)}{T_A^2(0, 200)} = 10 \log \left[(1 \times 10^{-6}) t \left(g_{31} \frac{\tau_{\theta\theta}^{C1}}{P_o} + g_{31} \frac{\tau_{xx}^{C1}}{P_o} + g_{31} \frac{\tau_{rr}^{C1}}{P_o} \right) \right] + 225.8. \tag{12}$$

To complete the solution of equation (12), it is necessary to form the system matrix composed of

equations (150) through (319) from reference 3. Inverting this matrix at each wavenumber and frequency point permits the solution for the undetermined coefficients A_1^{C1} , A_2^{C1} , B_1^{C1} , B_2^{C1} , C_1^{C1} , and C_2^{C1} . These coefficients are inserted into equations (8), (9), and (10) for the stresses. Generation of the surfaces shown in figures 4 and 5 is now possible for any of the three excitations (P_o , P_x , or P_θ).

Sensitivity to Wall Pressure and Longitudinal Wall Shear Stress. The normalized ABC array sensitivity to wall pressure is computed as displayed in figure 4. Evaluation of equation (11) at $k = 0$, for all frequency, provides a theoretical estimation of the absolute sensitivity of the ABC array. This value can be compared directly to the experimental broadside calibration. An in-depth discussion of this comparison will be presented in an upcoming section on calibration.

The ABC array response to a longitudinal wall shear stress excitation P_x , which is computed in a similar fashion from the theory developed in reference 3, is displayed in figure 5. The response to such excitation is normalized by the same value of -225.8 dB ($T_A^2(0, 200)$) that was applied to the wall pressure. The only calibration applied to the experimental data is that of the wall pressure response P_o . Treating the data in this way assumes that the primary pressure component of interest is the wall pressure component; the shear stress response is then an uncalibrated signal. What has not been done during this analysis, yet should be a topic for future research, is to calibrate the ABC array for a shear stress excitation so as to obtain accurate absolute values of the fluctuating shear component of the TBL. In this analysis, regions of wall shear stress domination will be identified; however, the magnitudes of the levels will not be exact.

It is interesting to compare the expected levels from the wall pressure excitation and the longitudinal shear stress excitation. Two beamformed surface calculations (equation (1)) are performed using figures 4 and 5 for $T^2(k, \omega)$ and suitable excitation models for the wall pressure and wall shear stress components. These surfaces are then compared along the convective ridge wave speed for the simulation, which is 9.3 m/sec (figure 6). From this comparison, it is seen that the longitudinal response exceeds the radial response below approximately 45 Hz. In terms of the experimental design, there will be a cutoff frequency above which the convective ridge is

derived from wall pressure excitation and below which the convective ridge is derived from longitudinal shear stress excitation. This cutoff frequency will decrease with decreasing freestream flow velocity and will increase with increasing freestream flow velocity.

Figure 7 is a frequency cut at 50 Hz depicting the equivalence of the radial and longitudinal responses. The fact that there is a radial response in excess of the longitudinal response is fundamental and enables the ABC dynamic mechanical structure to be used for making direct measurements of the wall pressure component of the TBL pressure spectra.

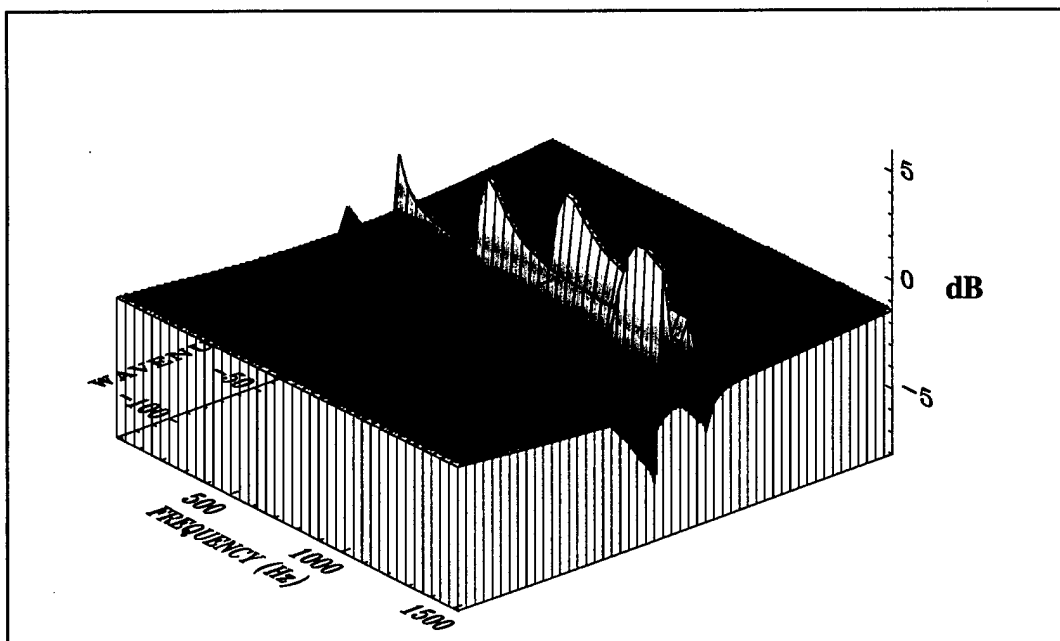


**Figure 4. ABC/PVDF Sensitivity to a Wall Pressure Excitation
Normalized by -225.8 dB (Magnitude = dB)**

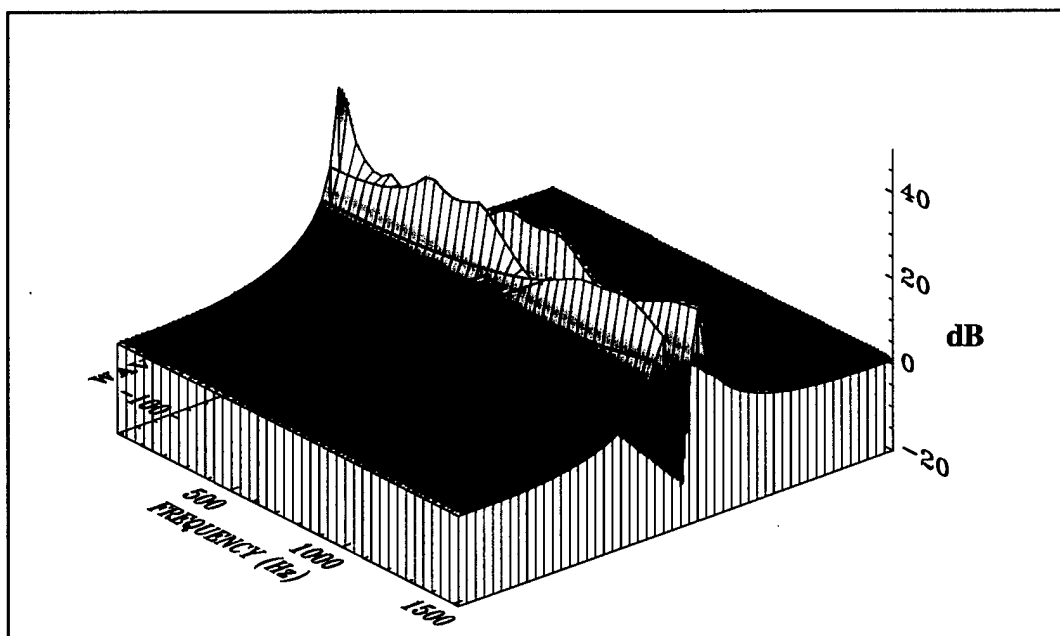


**Figure 5. ABC/PVDF Sensitivity to a Longitudinal Wall Shear Stress Excitation
Normalized by -225.8 dB (Magnitude = dB)**

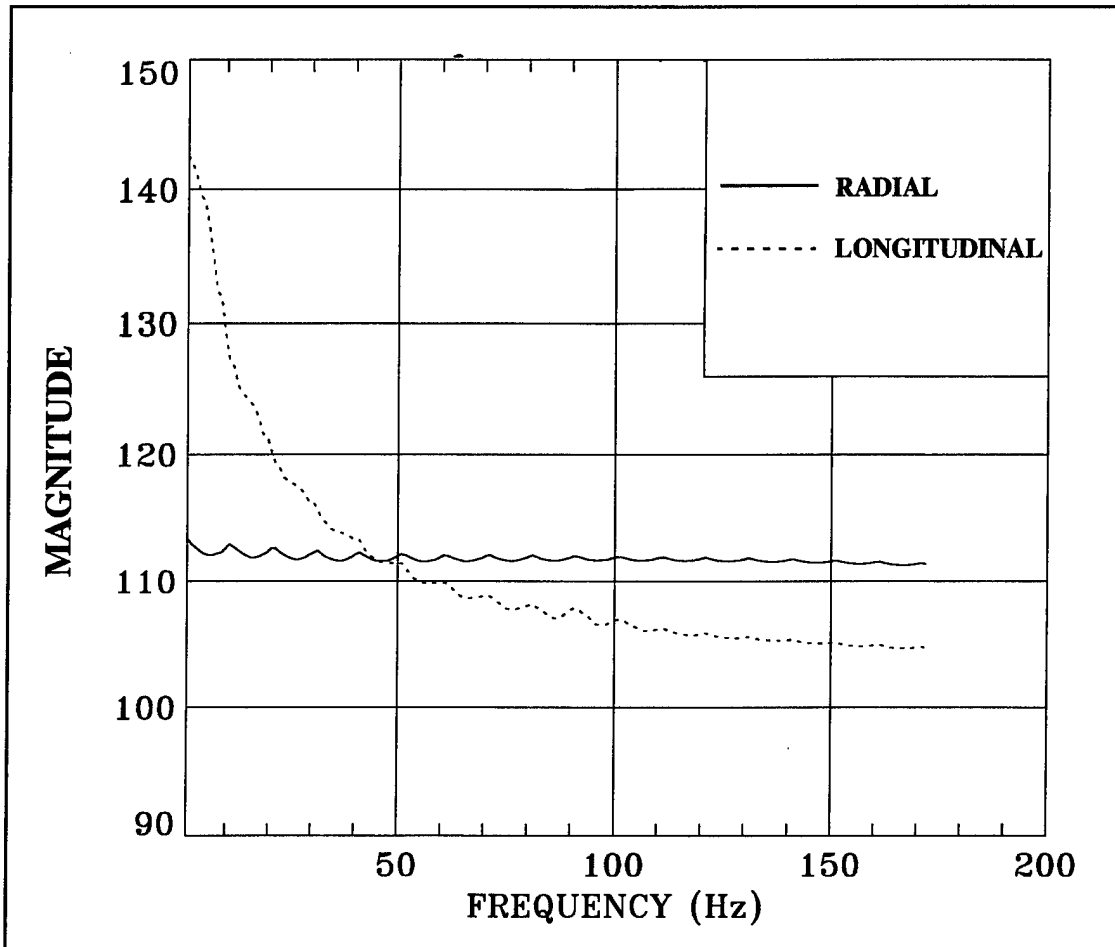


Figure 6. Comparison of ABC/PVDF Beamformed Response Surfaces for Radial and Longitudinal Excitations at 9.3 m/sec
(Magnitude = $10 \log(P_o)^2$ re $\mu Pa^2/Hz/rad/m$)

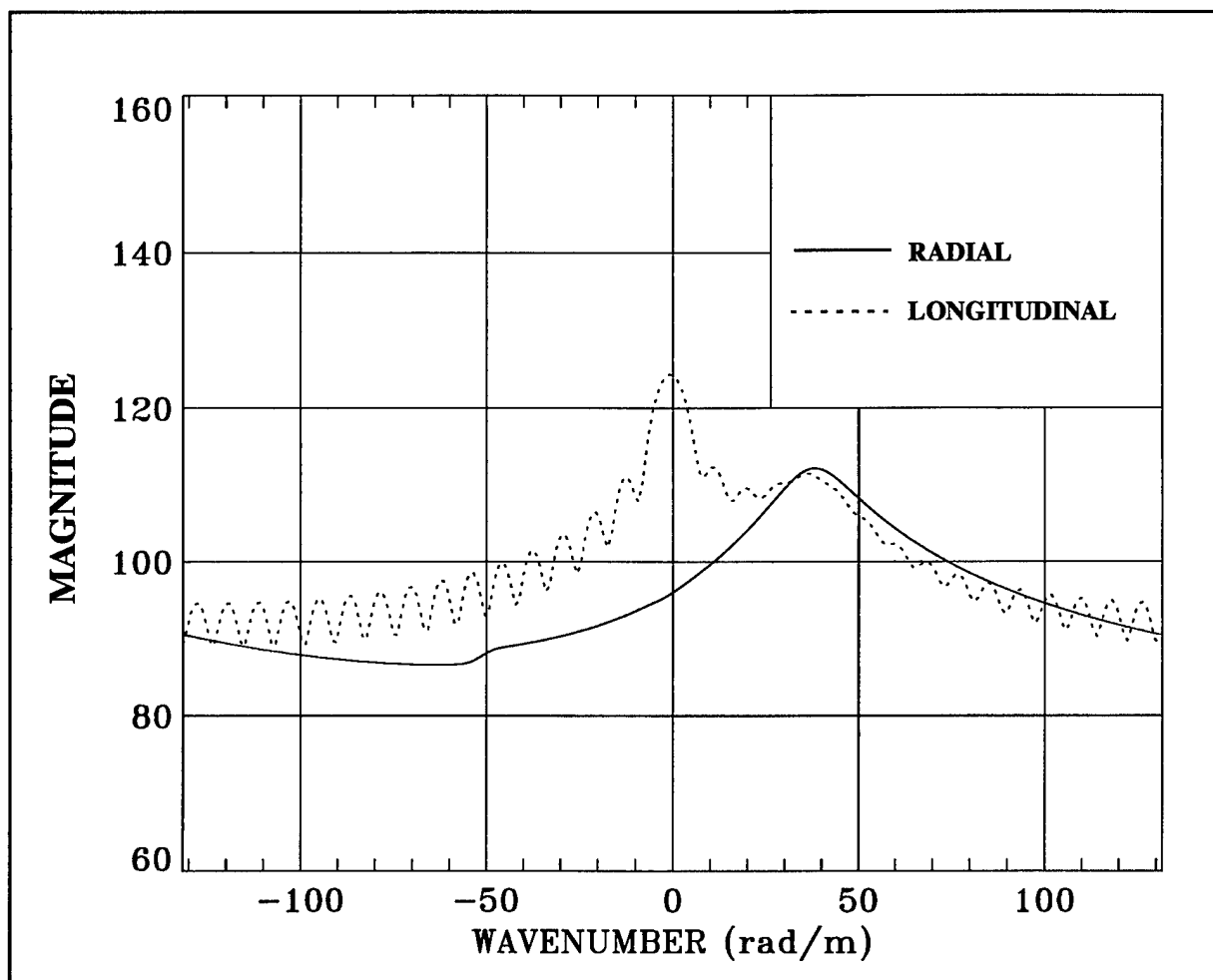


Figure 7. Comparison of ABC/PVDF Beamformed Response Surfaces at a Frequency Cut of 50 Hz (Magnitude = $10 \log(P_o)^2$ re $\mu Pa^2/Hz/rad/m$)

EXPERIMENTAL TEST CONFIGURATION

The TBL fluctuating wall pressure wavenumber-frequency plane (figures 1 and 2) is experimentally measured with the multichannel arrays and single-channel sensor (cylinders) shown in figure 8. The cylinders were towed from a surface craft at speeds ranging from 2 to 20 nautical miles per hour.

An important design parameter of the experiments was the creation of identical boundary layers over all the cylinders. This was done by keeping the diameters of the cylinders exactly the same and locating the array centers at identical setback distances from the telemetry module. The telemetry module is 4.0 inches in diameter as contrasted with 0.625 inch for the multichannel

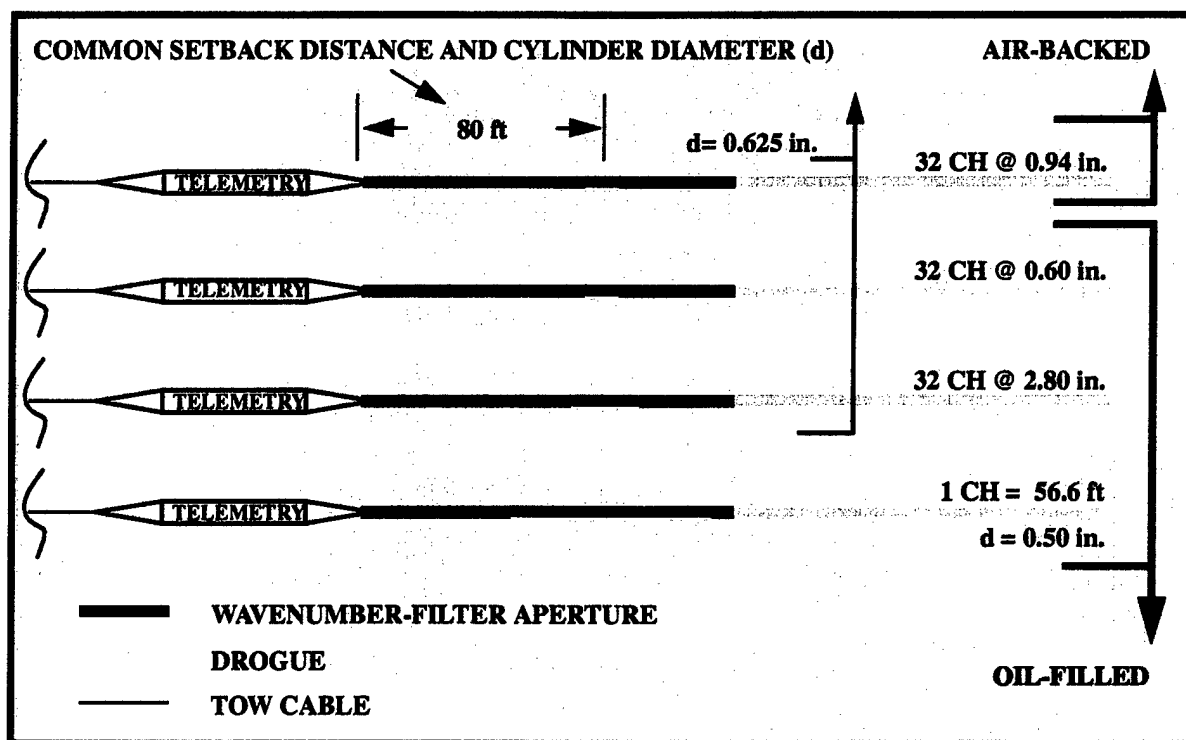


Figure 8. Experimental Test Configuration for All Wavenumber Filters

arrays; therefore, flow separation is likely to occur at this juncture, with boundary layer

reattachment and growth proceeding similarly over all the cylinders. The common setback distance to the array centers helps to ensure that the field is being measured at a point that is nearly the same from cylinder to cylinder.

One aspect of the pressure field differs between the ABC and OFC cylinders. By virtue of the innate physical contrast in radial compliance between an air-backed stiff cylinder and an oil-filled soft compliant cylinder, the pressure field generated at the surface will be substantially different between the two structures. This field, which results from the forced movement of the cylinder wall due to the presence of the TBL wall pressure, must be accounted for during the calibration of the data.

One assumption, foundational to this research, is that the TBL wall pressure spectra are unaffected by the elastic cylinder wall motion. This assumption can be made with confidence because the displacement scales of the wall motion are orders of magnitude less than the displacement scales existing in the turbulent eddies; therefore, the turbulent eddies form and impinge on the cylinder wall with negligible effect from the wall motion. This assumption allows the TBL wall pressure spectra to be completely uncoupled from the wall motion.

AIR-BACKED CYLINDER

High-Wavenumber Aperture

The ABC array is a composite wall construction containing an inner cavity of air. Construction of the composite wall begins with an extruded KEL-F brand thermoplastic tube. KEL-F is a highly fluorinated resin that requires chemical etching to facilitate bonding to its surface. This material was selected for its superior mechanical properties and dielectric strength.

After the sensor aperture is located, wiring holes are drilled through the KEL-F tube. Each PVDF piezo film sensor is then bonded to the tube with a urethane adhesive. The center-to-center spacing of the sensors is 0.94 inch, with an active area of 0.45 inch. Therefore, a gap of 0.49 inch exists between channels. A wire bundle is inserted into the tube and a shielded twisted

pair of wires is pulled through the wiring hole located beside each sensor. (This wire, manufactured by GORE, Inc., has a jacket of PTFE to achieve sufficient strength in the 28- to 34-gauge range to prevent breakage from normal handling). Wire connections to the sensor are made with conductive epoxy, and each wire hole is sealed with urethane.

A coat of nonconductive urethane is painted over the sensor aperture (electrical insulation), followed by a coat of conductive epoxy, which is connected to ground and effectively provides the aperture with an electrical shield. The entire cylinder is overmolded in urethane, resulting in an outer diameter of 0.625 inch.

The 0.94-inch channel-to-channel spacing provides an unaliased measurement range in wavenumber of ± 131 rad/m. The raw sensitivity of the composite array without amplification is -224 dB re $\text{volt}^2/\mu\text{Pa}^2$.

The KynarTM piezo film used in this array was supplied by AMP Flexible Film Sensors, Valley Forge, PA. All of the PVDF copolymer hydrophone elements used in the OFC arrays, discussed next, were provided by the same firm.

OIL-FILLED CYLINDER

The OFC construction, which follows the same approach for all apertures, uses an open-cell foam core suspended in fiber stringers. Hydrophones are mounted at the appropriate spacing and then glued into the open-cell foam core. Individual shielded twisted pairs of wire are run from the forward connector to each hydrophone channel location. Next, the apertures are covered with a layer of shield cloth that is connected to ground. This assembly is pulled into the hose, which is then filled with a nonconductive oil of suitable specific gravity to render the finished assembly neutrally buoyant.

High-Wavenumber Aperture

The hydrophone used in the high-wavenumber filter aperture was manufactured by Benthos, Inc., located in North Falmouth, MA. It has an air-backed nodal-mounted ceramic cylinder

design that was chosen for its acceleration-canceling performance. The hydrophone assembly is placed in a perforated metal cage. When mounted in the array, the hydrophone cage is in contact only with the open-cell foam; no mechanical contact is made with the ceramic surface. The fill fluid alone has contact with the acoustically sensitive ceramic hydrophone surface. These precautions ensure that the hydrophone will respond only to pressure fields existing in the fill fluid and not to the relative motion between the ceramic cylinder and the associated mechanical components of the towed array cross-section. The sensitivity of the hydrophone without amplification is $-208.5 \text{ dB re volt}^2/\mu\text{Pa}^2$ and the capacitance averages 700 picofarads. The acceleration sensitivity of the hydrophone is $-60 \text{ dB re m/sec}^2$.

As shown in figure 8, the channel spacing achieved with the high-wavenumber aperture is 0.60 inch, which provides an unaliased wavenumber measurement range of $\pm 206 \text{ rad/m}$. The advantage of this aperture is that the unaliased wavenumber range is high enough to permit the entire pressure field to be measured without any component aliasing.

Medium-Wavenumber Aperture

The medium wavenumber aperture differs from the high-wavenumber aperture in hydrophone type and channel spacing. The hydrophone element consists of a three-layer composite of aluminum plates and 500-micron-thick PVDF copolymer. The aluminum plates are wire bonded in parallel and encapsulated in epoxy for mechanical protection. Each hydrophone element is 0.2 inch wide by 0.55 inch in length. A channel is then composed of four elements wired together in series to form one hydrophone group. The channel spacing is 2.80 inches and the unaliased wavenumber measurement range is $\pm 44 \text{ rad/m}$. The final sensitivity of the four-element channel with the connecting wire required to reach the preamplifier is $-211 \text{ dB re volt}^2/\mu\text{Pa}^2$ and the capacitance is 113 picofarads.

Low-Wavenumber Aperture

This sensor is the only one of the set that is housed in a 0.5-inch-diameter cylinder rather than in a 0.625-inch-diameter cylinder. The original design goal had been a 0.5-inch diameter for all

cylinders. However, space requirements precluded the construction of the multichannel arrays in cylinders this small, which is why the 0.625-inch cylinders were used. The low-wavenumber sensor represents what was technically feasible to construct in a 0.5 inch cylinder.

The piezoelectric material used in the hydrophone is a single layer of 500-micron PVDF copolymer, measuring 0.085 inch in width by 0.55 inch in length. This material is sandwiched between two 0.008-inch-thick aluminum plates to form an element. Each element has a capacitance of 4.16 picofarads and sensitivity of $-198 \text{ dB re volt}^2/\mu\text{Pa}^2$. A total of 640 uniformly distributed elements are wired together to form a single acoustically sensitive aperture that is 56.6 feet in length.

It is apparent from the TBL surface (figure 2) that there is a rather large disparity between the magnitude of the convective ridge and the magnitude of the low-wavenumber region. The likelihood of contaminating a low-wavenumber measurement with high-wavenumber energy is thus very large. A solution to this problem that involved the inventive use of the cross-sectional area available in the 0.5-inch diameter led to the single 56.6-foot-long sensor. This 56.6-foot-long sensor has a directivity pattern consisting of a mainlobe (0.36 rad/m wide) centered on broadside ($k = 0 \text{ rad/m}$), with sidelobes trailing off until aliasing lobes (based on 0.6-inch element spacing) appear. The aliasing lobes occur at 206 rad/m , which, as was seen in the high-wavenumber aperture, is a sufficiently high wavenumber to have inconsequential effects on the primary measurement space. The single sensor is then equivalent to a fully populated array with no gaps between channels steered to broadside. An array with 56.6 feet of aperture requiring 1,160 channels on 0.6-inch centers was not constructed because it would be prohibitively expensive to build.

The value of this single-sensor design becomes obvious when the purpose of the sensor (i.e., to measure low-wavenumber energy) is kept in mind. Test conditions must be such that the magnitude of the flow noise exceeds all other pressure levels centered at $k = 0 \text{ rad/m}$ (center of the acoustic cone). The center of the acoustic cone (a broadside arrival angle) is coincident with the mainlobe of the sensor response; thus, it is imperative that the flow noise level exceed the level of any acoustic propagation that occurs simultaneously with the flow noise measurement.

CALIBRATIONS

FREQUENCY CALIBRATION

All the sensors used in the experiments were configured with a preamplifier as the first stage of amplification following the raw transducer output; figure A-1* shows the signal amplification path. The preamplifier is designed with a shaped frequency response (variable gain) ranging from 0 dB at direct current to 38.5 dB at 1000 Hz. Two other stages of amplification are applied to the signal following preamplification: a 14-dB postamplifier gain stage and a 6-dB gain through the telemetry system. These last two gain stages are constant and exhibit no variation with frequency. The frequency calibration was performed at NUWC Division Newport's acoustic calibration facility (Dodge Pond) in Niantic, CT.

Broadside Calibration ($k = 0$)

Air-Backed Cylinder. The values obtained from the frequency calibration at Dodge Pond are listed in column 2 of table A-1. The test geometry between the acoustic source and array was arranged such that the acoustic wavefront and the longitudinal axis of the cylinder were parallel (broadside arrival angle). The final calibration with all gains applied is listed in the column labeled 4.

The raw sensitivity of the ABC/piezo film sensor is listed in column 1 of table A-1 at four frequencies; the average value is -225.1 dB re $\text{volt}^2/\mu\text{Pa}^2$. This value compares very favorably with the value of -225.5 dB from the analytic simulation of this structure described previously. The broadside calibration provides verification of the sensitivity surface shown in figure 4 at $k = 0$. What remains to be verified is the magnitude of the higher wavenumber plateau that is predicted to be at a lower sensitivity than the $k = 0$ broadside sensitivity. This nonflat aspect of the response surface is the reason for performing a wavenumber calibration and ultimately for adjusting the data with a theoretical/experimental response surface.

Additional broadside calibrations were performed in the anechoic chamber at NUWC

* Figure A-1, tables A-1 through A-5, and table B-1, all called out in this section, reside in the appendixes at the end of this report, where the calibration data are more fully described.

Division Newport. These calibration values are tabulated in column 1 of table A-2. For comparison, the broadside calibration from the Dodge Pond facility is listed in column 2 of the same table. The broadside calibration in air produced a result that is 5 dB more sensitive than would be produced in water. Although there is no concrete explanation for this discrepancy, plausible reasons for the variance in sensitivity observed between the two tests might include (1) the lack of static pressure on the structure and (2) the drifting of the properties with time (3 years between tests).

Column 4 (table A-1), which shows the final frequency calibration that is entered into the software used to analyze the data from the tests, is contained in the FORTRAN code as calibration file *kelfc3a.cal*.

Oil-Filled Cylinders. The OFC calibrations are recorded in tables A-3 through A-5 for a broadside test configuration. Column 4, in each table, is used to create the final calibration file for each array. Because OFCs containing ceramic hydrophones have uniform sensitivity with respect to arrival angle, there will be no discussion of broadside versus endfire sensitivity for these sensors. This uniform sensitivity is apparent from viewing the response surface shown in figure 3 (upper wire frame image). A tabulation of the FORTRAN files used for calibration is given in table 3.

Table 3. Sensor Calibration Files

Sensor Type	FORTTRAN File
ABC - Air-Backed Cylinder Array	<i>kelfc3a.cal</i>
SCH - Single-Channel Hydrophone	<i>sch.cal</i>
MK2 - Medium-Wavenumber Array	<i>mk2.cal</i>
HK2 - High-Wavenumber Array	<i>hk2.cal</i>

WAVENUMBER CALIBRATION

Inspection of figure 4 is sufficient to show the need for concern about the uniformity of the ABC sensitivity as a function of wavenumber. In this figure, the shape of the response is attenuated by the algorithm used to display the surface. In reality, the response is in the form of a raised triangle, whose vertex is at the origin (the base), parallel to the wavenumber axis. The response is resonant at each side of the cone. When a physical surface such as this is processed by an algorithm that displays a surface based on approximately 32 by 32 points, the sharp resonance is undersampled, resulting in the jagged appearance along the long sides of the triangular response, as seen in the figure. These problems are mitigated to some degree in figure 9, which is an image that depicts the triangular response more clearly. The variation in amplitude can be discerned by the difference in color between the low-wavenumber $k = 0$ region and the higher wavenumber response outside of the cone.

Figure 10 displays a cut through figure 9 at 450 Hz. In this figure, the $k = 0$ value of -225.5 dB is clearly evident, as well as the decrease in sensitivity at higher wavenumbers. From this theoretical simulation, a 3-dB decrease in sensitivity is observed between the $k = 0$ sensitivity and the higher wavenumber plateau region. Calibrations performed in water, at various arrival angles, will span the range of phase velocities between ± 1500 m/sec. This region lies entirely within the constant sensitivity range of the raised triangle response. The only practical way of experimentally measuring the sensitivity in the high-wavenumber region then is to calibrate the sensor in a fluid of slower compressional wave speed (such as air) in an anechoic chamber (such as the one located at NUWC Division Newport).

Anechoic Chamber (Air Endfire)

Table B-1 (appendix B) tabulates calibrations performed at broadside and nearly air acoustic endfire. The decrease in sensitivity at endfire is approximately 5.5 dB, which compares favorably, although not exactly, with the theoretical prediction. A null in the theoretical response at ± 3.5 rad/m was explored during the calibration in the anechoic chamber, where it was found to exist at an angle of 32 degrees measured from broadside. The null appears at 27 degrees in the simulation of figures 9 and 10. The decrease in sensitivity from broadside to the

null measured during the calibration ranged from 7.5 to 15.0 dB; the corresponding theoretical decrease in sensitivity from broadside to the null is 9 dB.

The comparison between the wavenumber calibration and the theoretically predicted response tracks qualitatively, though not precisely quantitatively, leading to the conclusion that it is better to apply a wavenumber calibration to the experimental data than to ignore it. Secondly, it is best to use the theoretical prediction rather than the experimental calibration because of the shift in broadside sensitivity observed between the Dodge Pond calibration and the anechoic chamber calibration. Due to the several reasons given earlier for this discrepancy, it is not prudent to base the magnitude of the wavenumber calibration on the results of the anechoic chamber calibration. However, the qualitative results of the anechoic chamber calibration and the precise agreement between measured and predicted broadside sensitivity (-225 dB) justify the application of the theoretical wavenumber calibration to the experimentally acquired data.

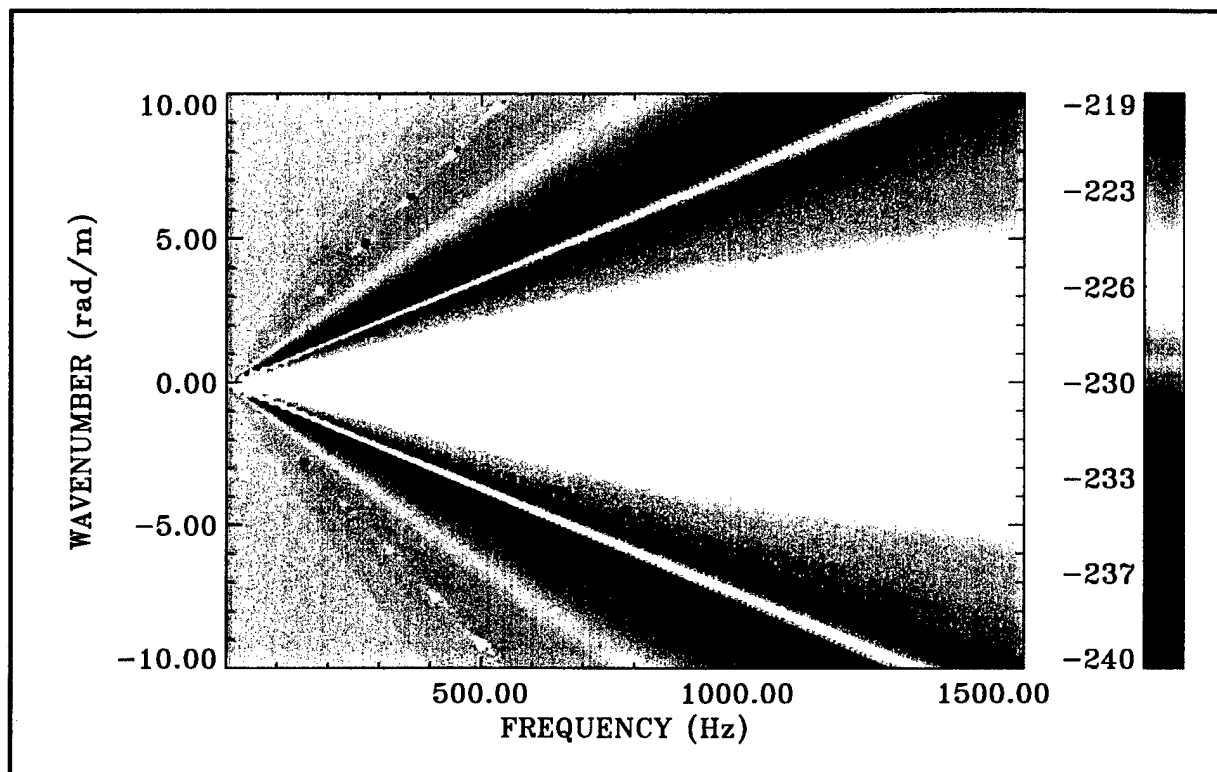
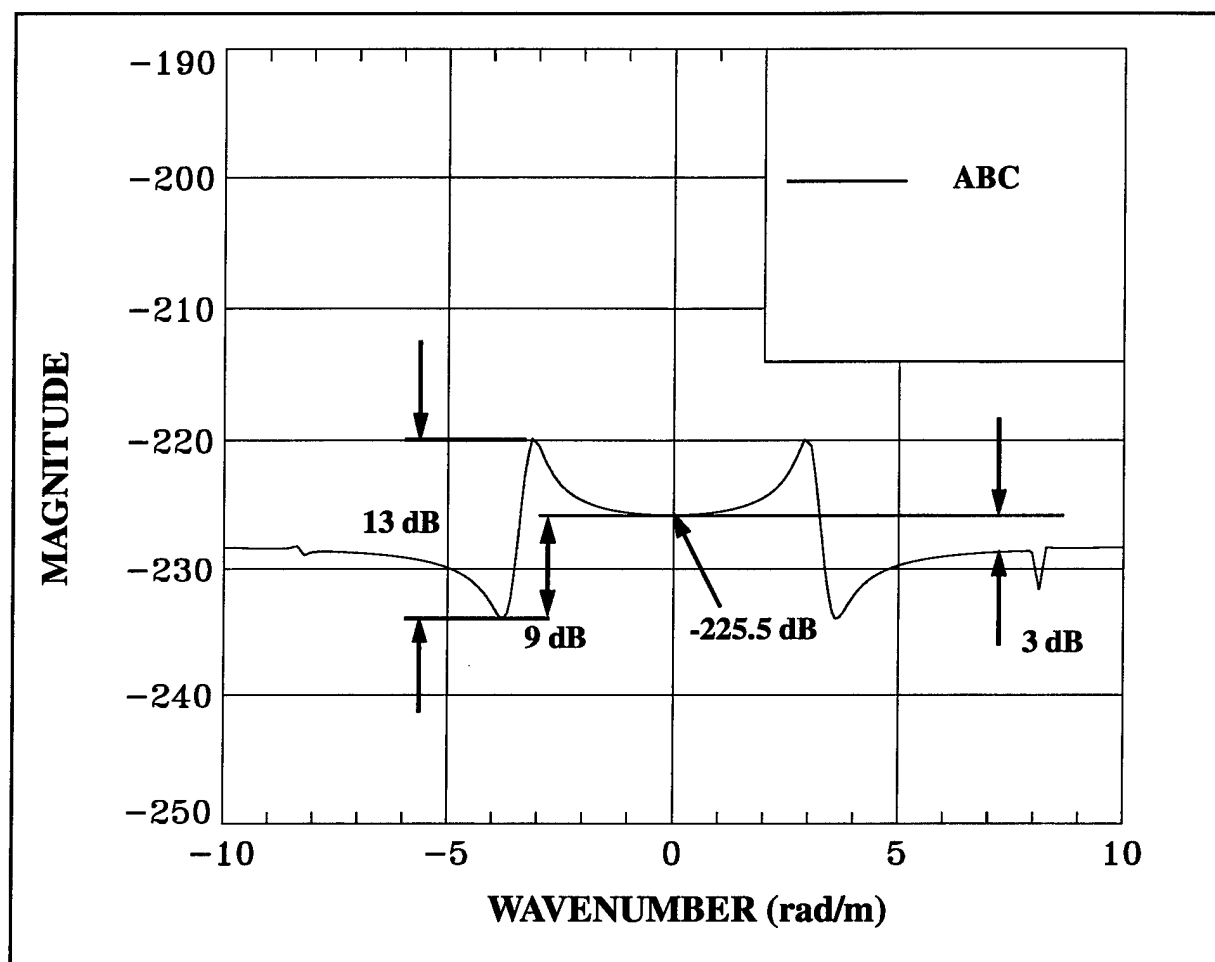


Figure 9. ABC/PVDF Absolute Sensitivity to Wall Pressure Excitation
(Magnitude = dB re volt²/μPa²)



**Figure 10. Cut in Frequency at 450 Hz for Figure 9 Showing ABC/PVDF
Absolute Sensitivity to Wall Pressure Excitation
(Magnitude = dB re volt²/μPa²)**

THEORETICAL FIELD CALIBRATION (k, ω) PLANE

Assumptions and Limitations

The combination of TBL wall pressure and dynamic structure interaction represents an interesting crossover between two fields of science, in which the forcing pressure field in the water is generated in two distinctly different ways.

Typically, in the field of structural acoustics, an acoustic source generates a propagating wave in the fluid medium that contacts the structure, causing both a reflected wave and a motion of the surface, which becomes the source of a self-generated wave. The total pressure at the surface of the structure, P_t^1 , can be expressed as

$$P_t^1 = P_i + P_{s\infty} + P_s^1, \quad (13)$$

where P_i is the incident pressure generated by a farfield plane wave, $P_{s\infty}$ is the reflected pressure from an infinitely rigid structure, and P_s^1 is the pressure field generated by the forced motion of the elastic structure. The underscored 1 indicates the ABC.

In the field of fluid dynamics, the wall pressure generated beneath the TBL differs from the case most commonly considered in acoustics since the pressure field is generated locally, with no individual P_i and $P_{s\infty}$ components. The substitution that is made into equation (13) is

$$P_i + P_{s\infty} \Rightarrow P_o(k, \omega)|_{r=b}, \quad (14)$$

resulting in

$$P_t^1 = P_o(k, \omega)|_{r=b} + P_s^1. \quad (15)$$

The total pressure existing at the surface of the sensor, $r = b$, is P_t^1 . This pressure is filtered by the dynamic mechanical response of the ABC ($T_{ABC}(k, \omega, \bar{b})$) and the spatial Fourier transform of the sensor's finite aperture ($H_{ABC}(k)$). A block diagram of the two attenuations is

shown in figure 11 below. Both attenuations need to be accurately estimated and removed, as well as the gains shown in appendix A (figure A-1), to properly estimate the value of the TBL wall pressure, $P_o(k, \omega)|_{r=b}$, that exists at $r = b$ in figure 11.

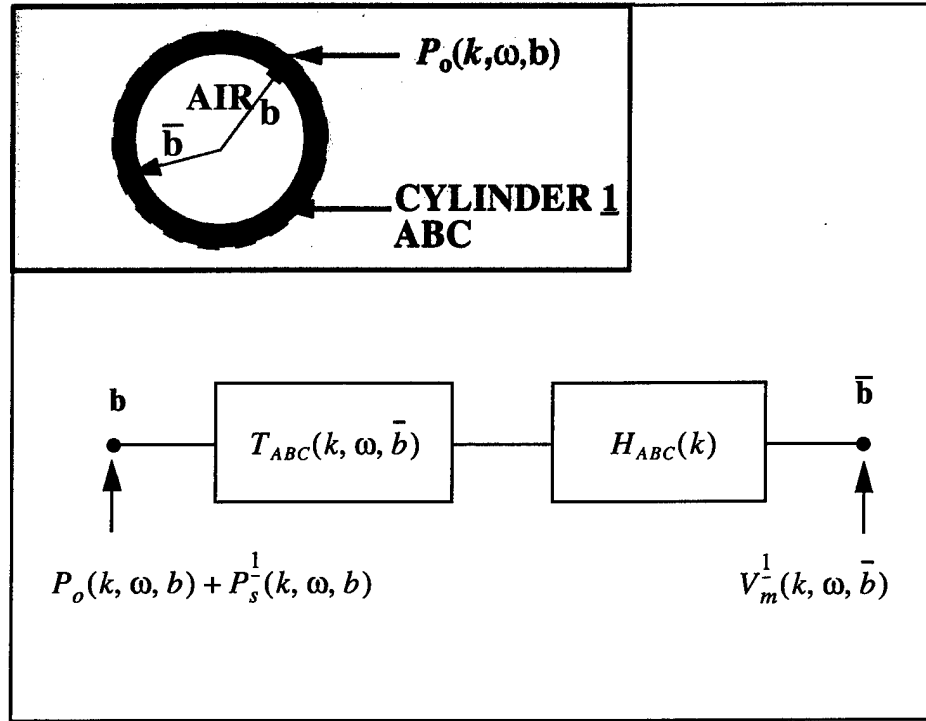


Figure 11. Signal Path Within the ABC Structure

In summary of the development thus far, the total pressure at radius $r = b$ is attenuated by the dynamic response of the ABC ($T_{ABC}(k, \omega, \bar{b})$) and the sensor's aperture function ($H_{ABC}(k)$); the final signal is then output from the sensor at $r = b$ (figure 11) as

$$(P_o(k, \omega, b) + P_s^1(k, \omega, b))(T_{ABC}(k, \omega, \bar{b})H_{ABC}(k)) = \frac{V_m^1(k, \omega, \bar{b})}{S^1}, \quad (16)$$

where $V_m^1(k, \omega, \bar{b})$ is the measured voltage spectra and S^1 is the frequency calibration for the array.

The surface-generated pressure, $P_s^1(k, \omega, b)$, can be written in terms of the wall pressure $P_o(k, \omega, b)$ and a theoretical simulation that will allow the wall pressure to be extracted directly from the measurement. As shown in the next section, $P_s^1(k, \omega, b)$ for the ABC is negligible over the intended measurement area in the wavenumber-frequency plane and may be safely ignored; however, $P_s^2(k, \omega, b)$ for the OFC is significant and must be retained for accurate estimations of the magnitude of the pressure spectra.

Pressure Field Components

Surface-Generated Pressure. The surface-generated pressure is expressed in terms of the wall pressure, $P_o(k, \omega, b)$, by evaluating the dynamic elasticity solution for the ABC that was previously discussed (reference 3). This surface-generated pressure, expressed as a transfer function with respect to forcing pressure, is

$$\frac{P_s^1}{P_o}(k, \omega, b) . \quad (17)$$

Figures 12 and 13 show the results of this calculation for the OFC and the ABC, respectively. Cuts in frequency are made through both of these surfaces at 100 Hz and are displayed in figure 14 for comparison. As seen in figure 14, the ABC surface-generated pressure is inconsequential, generally no greater than -20 dB, while the OFC surface-generated pressure field makes a significant contribution to the total pressure. This figure also shows that $P_s^2(k, \omega, b)$ is equivalent in magnitude to the forcing pressure $P_o^2(k, \omega, b)$ at 100 rad/m, increasing to +6 dB at the maximum unaliased wavenumber of the array, which is ± 206 rad/m.

Corrected Pressure. Equation (17) is combined with equation (16) to yield

$$\left[P_o(k, \omega, b) \left(1 + \frac{P_s^1}{P_o}(k, \omega, b) \right) \right] (T_{ABC}(k, \omega, \bar{b}) H_{ABC}(k)) = \frac{V_m^1(k, \omega, \bar{b})}{S^1} . \quad (18)$$

The solution of equation (18) for $P_o(k, \omega, b)$ results in

$$P_o(k, \omega, b) = \frac{V_m^{-1}(k, \omega, \bar{b})}{S^{-1}} \left[\frac{1}{\left(1 + \frac{P_s^{-1}}{P_o}(k, \omega, b) \right) (T_{ABC}(k, \omega, \bar{b}) H_{ABC}(k))} \right] . \quad (19)$$

Equations (4), (12), and the full solution to the dynamic elasticity problem presented by the ABC are required to fully solve for $P_o(k, \omega, b)$, as seen below in equation (20).

The full correction term for the ABC array is computed and displayed in figure 15. This correction term is the collection of terms contained in large brackets in equation (19) and is reproduced as equation (20):

$$\left[\frac{1}{\left(1 + \frac{P_s^{-1}}{P_o}(k, \omega, b) \right) (T_{ABC}(k, \omega, \bar{b}) H_{ABC}(k))} \right] . \quad (20)$$

The correction surface will be applied to the experimental raw data for all freestream velocities. Cuts through the correction surface of figure 15 are displayed in figure 16 for three freestream velocities.

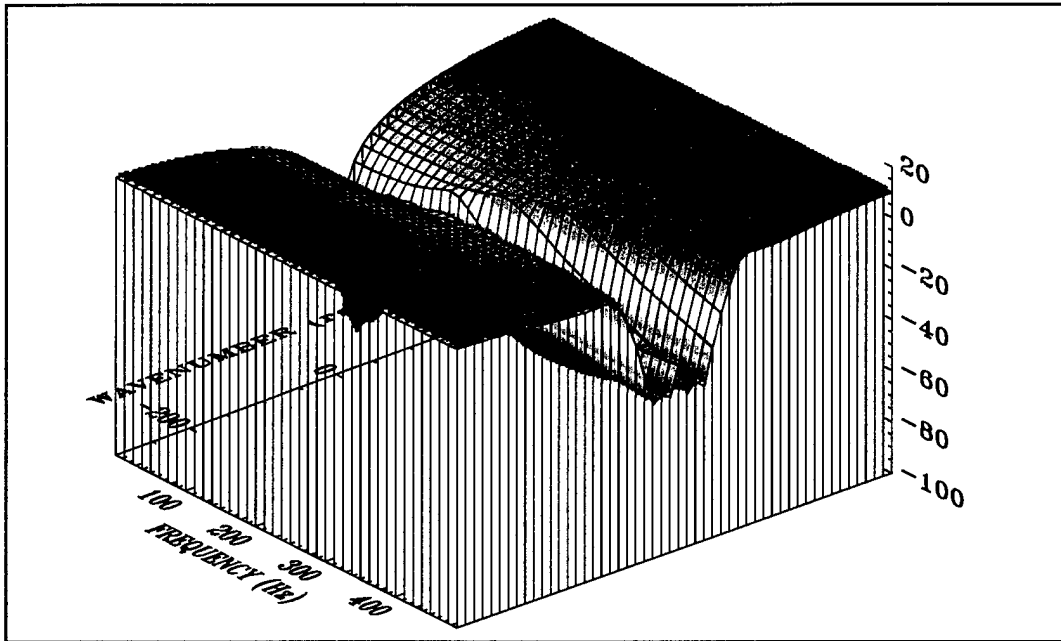


Figure 12. OFC Surface-Generated Pressure Field at $r = 0.327$ in.
 (Magnitude = $10 \log(P_s(r)/P_o)^2$)

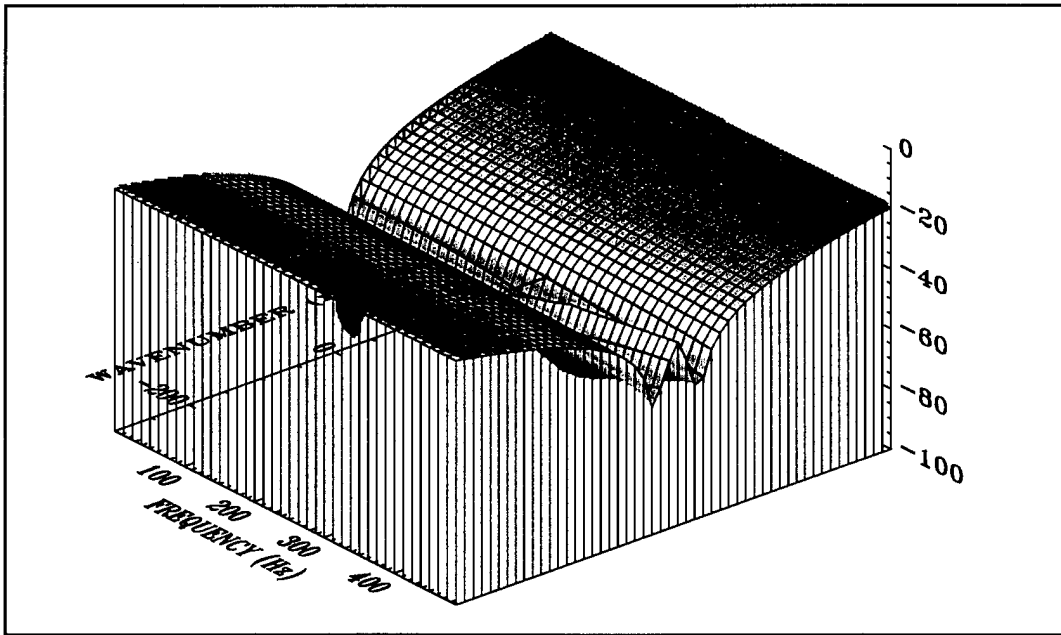


Figure 13. ABC Surface-Generated Pressure Field at $r = 0.327$ in.
 (Magnitude = $10 \log(P_s(r)/P_o)^2$)

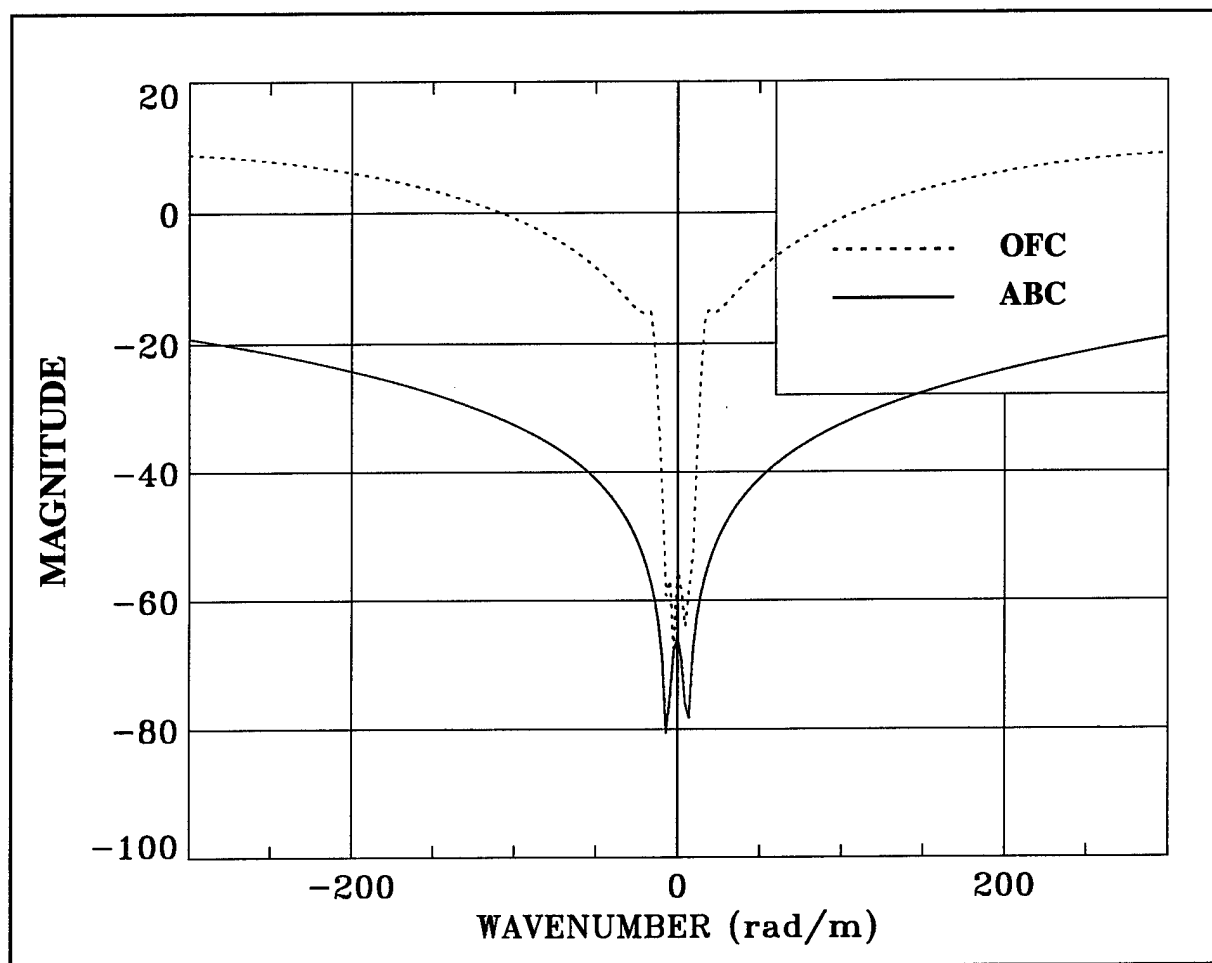


Figure 14. Cut in Frequency for Figures 12 and 13 Showing Surface-Generated Pressure Field Comparison at $r = 0.327$ in. and $f = 100$ Hz
(Magnitude = $10 \log(P_s(r)/P_o)^2$)

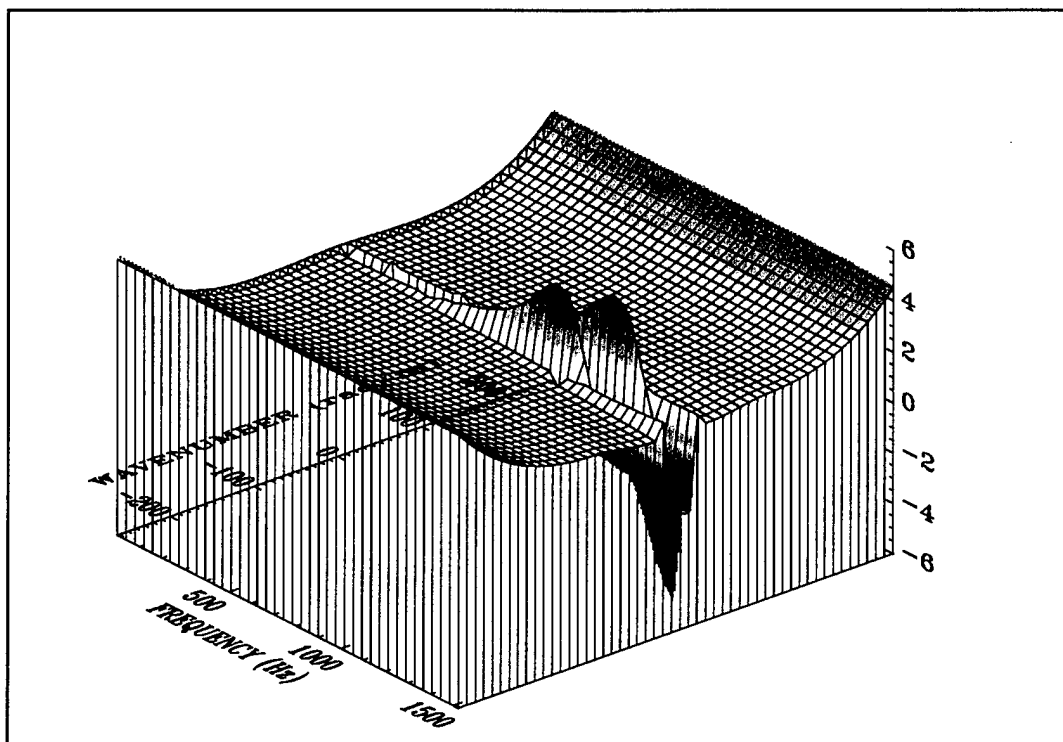


Figure 15. Theoretical Field Correction Surface for the ABC Normalization
Constant of -14.2 dB at $f = 200$ Hz and $k = 0$ rad/m
(Magnitude = dB re Equation (20))

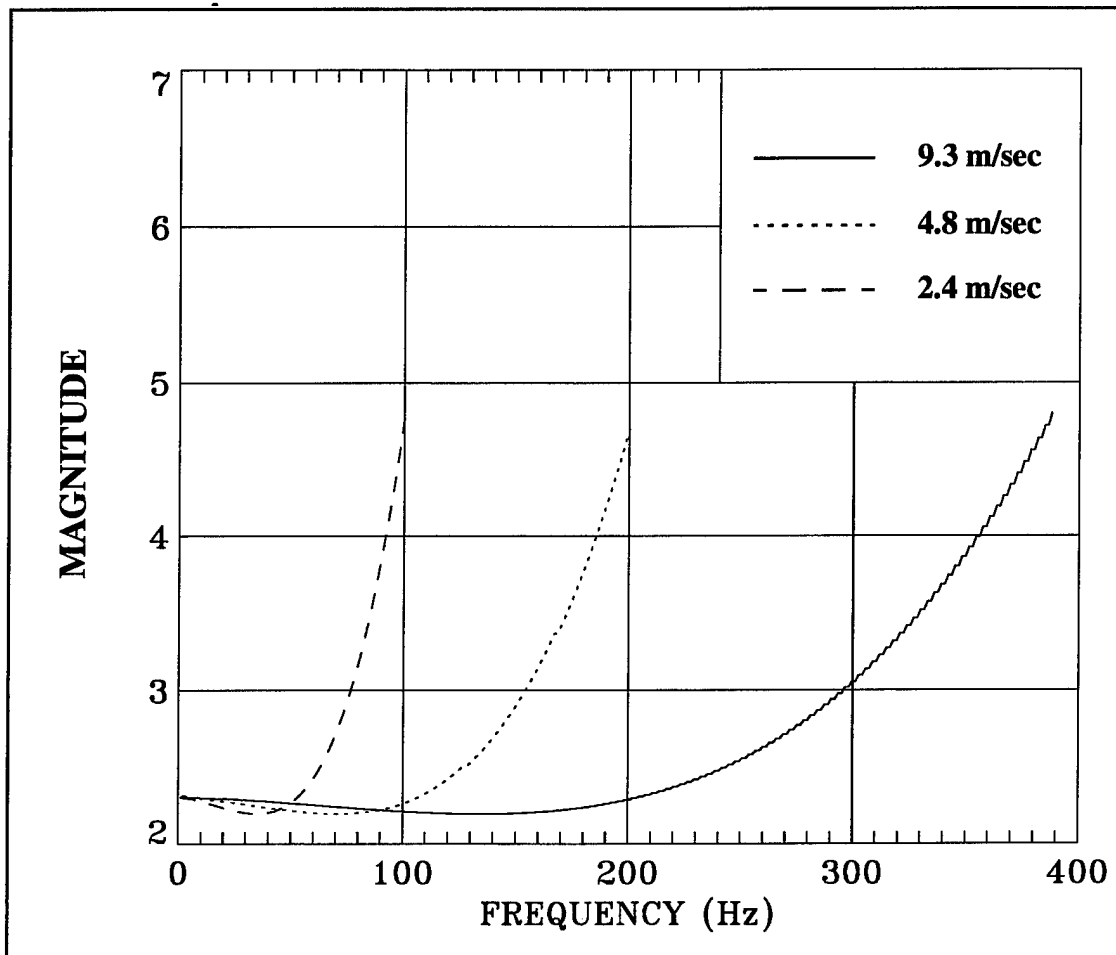


Figure 16. Cuts Through Figure 15 Showing Corrections to the Convective Ridge for Three Different Flow Speeds (Magnitude = dB)

Inner Pressure. The pressure measured by the OFC array will be used in a following section to produce a calibration of the hose wall transfer function, $T_{OFC}(k, \omega, a)$. It will be necessary to remove any contribution of $P_s^2(k, \omega, b)$ from the pressure field measured by the array to obtain an accurate calibration because the surface-generated pressure in the OFC is far more significant than in the ABC (see figure 14); the underscored 2 indicates the OFC. Once the surface-generated pressure field component is removed, $P_i(k, \omega, a)$ is composed solely of $P_o(k, \omega, b)$, which has been filtered by the OFC radial pressure transfer function, $T_{OFC}(k, \omega, a)$.

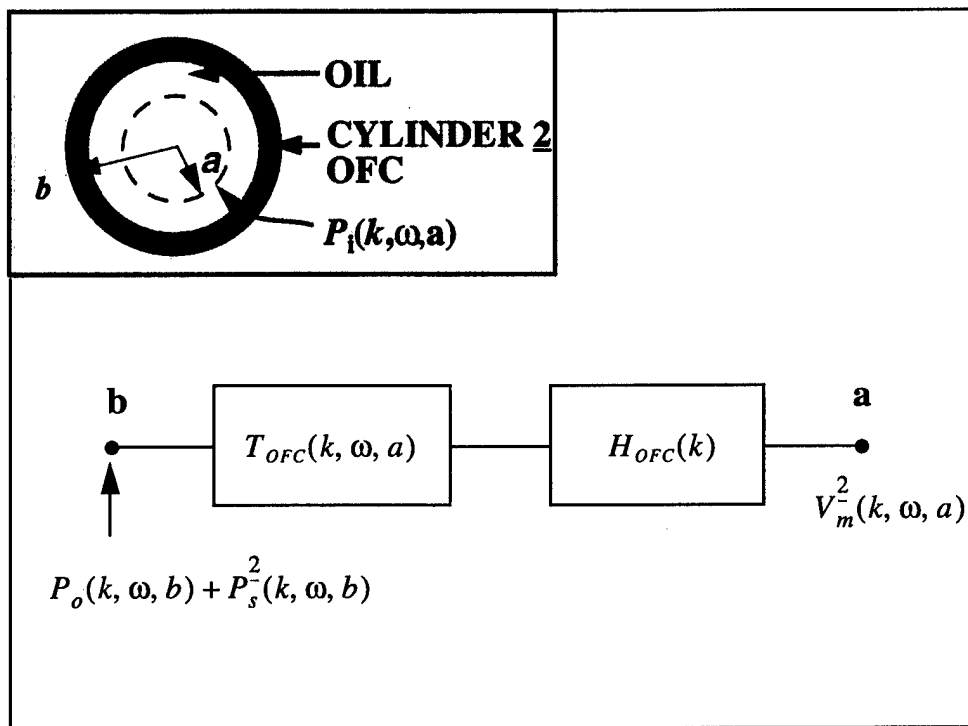


Figure 17. Signal Path Across the OFC

In a fashion analogous to that used for the ABC, an expression for the inner pressure $P_i(k, \omega, a)$ is illustrated in figure 17. The derivation starts with the total pressure acting on the outer surface of the cylinder:

$$P_i^2(k, \omega, b) = P_o(k, \omega, b) + P_s^2(k, \omega, b) . \quad (21)$$

The total pressure is then filtered by both the hose transfer function and the sensor aperture function, resulting in the measured pressure

$$\frac{V_m^2(k, \omega, a)}{S^2} . \quad (22)$$

The hose transfer function is the ratio between the internal pressure at radius a and the external pressure at radius b as follows:

$$T_{OFC}(k, \omega, a) = \frac{P_i(k, \omega, a)}{P_o(k, \omega, b)} . \quad (23)$$

The surface-generated pressure is expressed in terms of the forcing pressure field $P_o(k, \omega, b)$ and the theoretical simulation $P_s^2(k, \omega, b)/P_o(k, \omega, b)$ as

$$P_s^2(k, \omega, b) = P_o(k, \omega, b) \left(\frac{P_s^2}{P_o}(k, \omega, b) \right) , \quad (24)$$

which mathematically produces

$$P_t^2(k, \omega, b) T_{OFC}(k, \omega) H_{OFC}(k) = \frac{V_m^2(k, \omega, a)}{S^2} . \quad (25)$$

Equations (21), (23), and (24) are combined with equation (25) to yield the following expression for the inner pressure field that arises solely from the TBL wall pressure:

$$P_i(k, \omega, a) = \frac{V_m^2(k, \omega, a)}{S^2} \left\{ \frac{1}{\left[H_{OFC}(k) \left(1 + \frac{P_s^2(k, \omega, b)}{P_o(k, \omega, b)} \right) \right]} \right\} . \quad (26)$$

EXPERIMENTAL RAW DATA

All the experimental raw data are displayed as uncalibrated so that the dynamic range of the data is minimized and the best color contrast is achieved for a given color map. This approach will allow the reader to extract as much information (visually) as possible from the images.

AIR-BACKED CYLINDER

The ABC array data are displayed in figures 18 through 20 for freestream velocities of 5, 10, and 20 knots, respectively. The primary and prominent feature measured during the experiments is the convective ridge. Since the negative wavenumber half-plane does not have energy in the unaliased space of comparable amplitude to the first alias of the convective ridge, the alias of the convective ridge contains useful information that is not contaminated. To view the convective ridge more effectively, the negative wavenumber half-plane has been moved up above the terminus of the positive wavenumber half-plane; this shift has only been performed for the ABC experimental raw data.

OIL-FILLED CYLINDER

Data from the OFC high- k wavenumber filter are displayed in figures 21 through 23. A bi-directional breathing wave is evident at all flow speeds, with its energy extending well up to 1300 Hz at the 20-knot flow speed.

The convective ridge is evident at 10 and 20 knots but is not readily identifiable at the 5-knot flow speed. This is puzzling since not only is the convective ridge clearly visible in the medium- k wavenumber-filter 5-knot data (figure 24), but the sensitivity of the medium- k wavenumber filter is actually 3 dB less than that of the high- k wavenumber filter.

Acoustic energy is visible, centered on $k = 0$, for the high- k wavenumber filter, although its short aperture (1.6 ft) does not afford sufficient directionality to differentiate propagation directions. However, the 7.46-foot acoustic aperture of the medium- k wavenumber filter provides enough directivity for the acoustic cone to become evident in the medium- k data. In

figures 24, 25, 26, 27, and 28 (which contain data for 5-, 10-, 15-, 20-, and 25-knot flow speeds, respectively, for the medium- k wavenumber filter), the convective ridge aliases, wrapping around two times until it is attenuated by the hose transfer function.

The medium- k data will typically display a convective ridge with two distinct peaks, or ridges. However, a cut in frequency at 9.16 Hz, as was selected for figure 29, displays a minimal amount of double-ridge phenomena, even though these phenomena are still visible. Figures 30 and 31 zoom in on the 20-knot data, displaying the double-ridge phenomena more prominently.

The enigma of the medium- k data may be explained by the type of hydrophone used for the medium- k filter, which is the three-layer element made from 500-micron PVDF copolymer and alternating aluminum plates. This structure has a rectangular cross-section and does not have an axisymmetric response due to its composite planar asymmetric shape. The TBL is composed of spanwise or circumferential wavenumber content that could possibly be causing the asymmetric hydrophone to respond to wavenumbers in the boundary layer other than to the mode-0 axisymmetric component. Whether or not these components would travel at slightly different convective speeds or result in interference that would produce a local cancellation and dimple, causing the ridge to be construed as a double ridge, is an open question. And because the convective ridge energy is short in wavelength by nature, it will all the more probably produce an asymmetric hydrophone output.

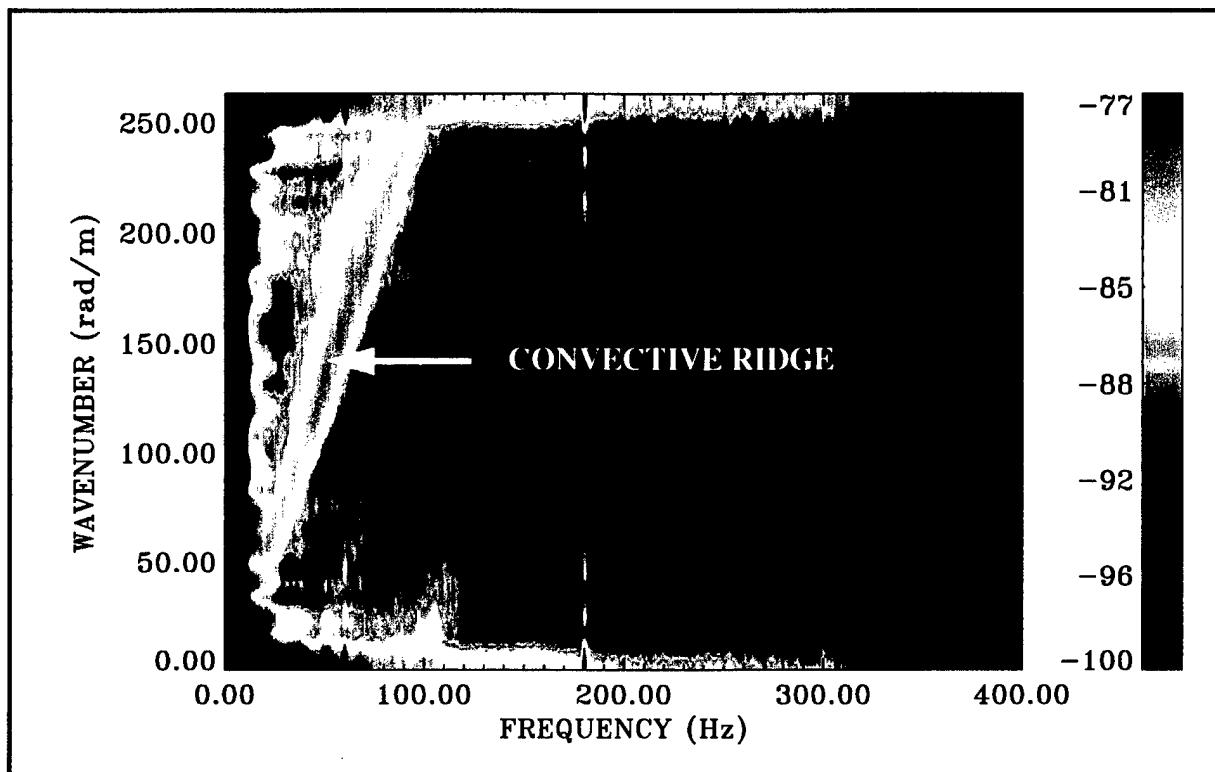


Figure 18. ABC Experimental Raw Data $P_o(k, \omega)$ at a 5-knot Flow Speed

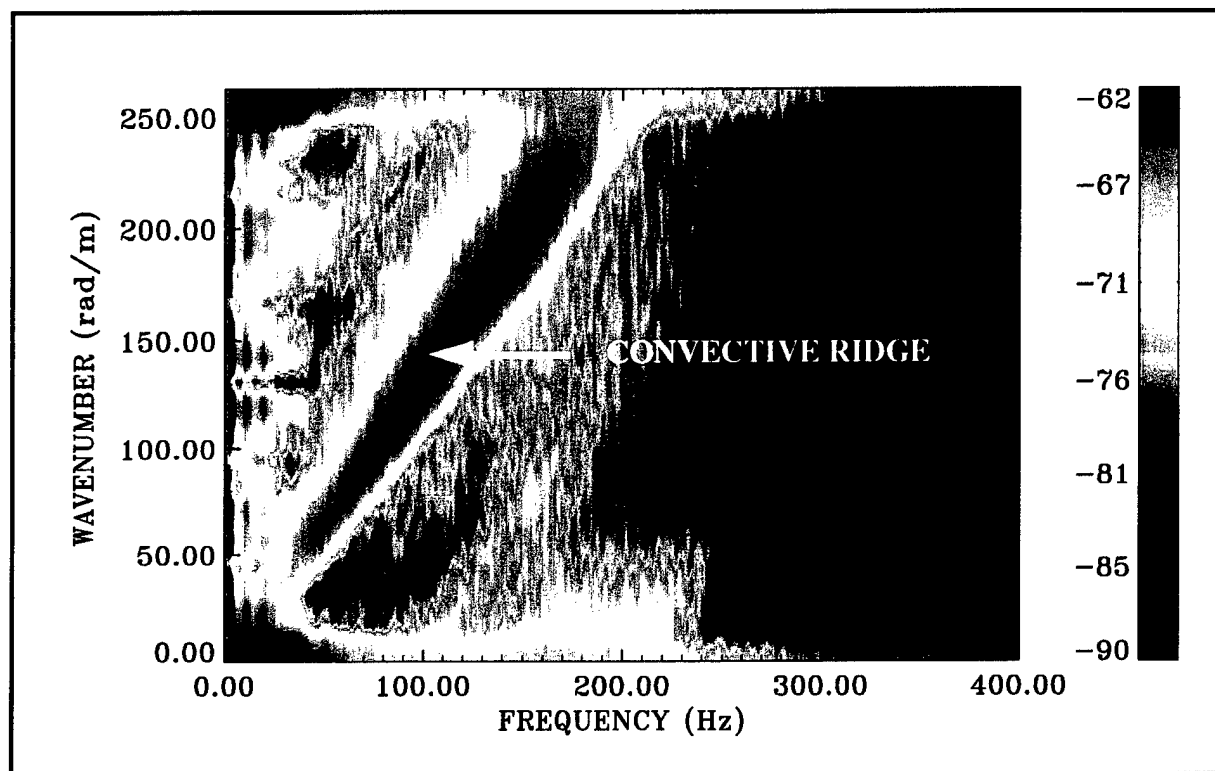


Figure 19. ABC Experimental Raw Data $P_o(k, \omega)$ at a 10-knot Flow Speed

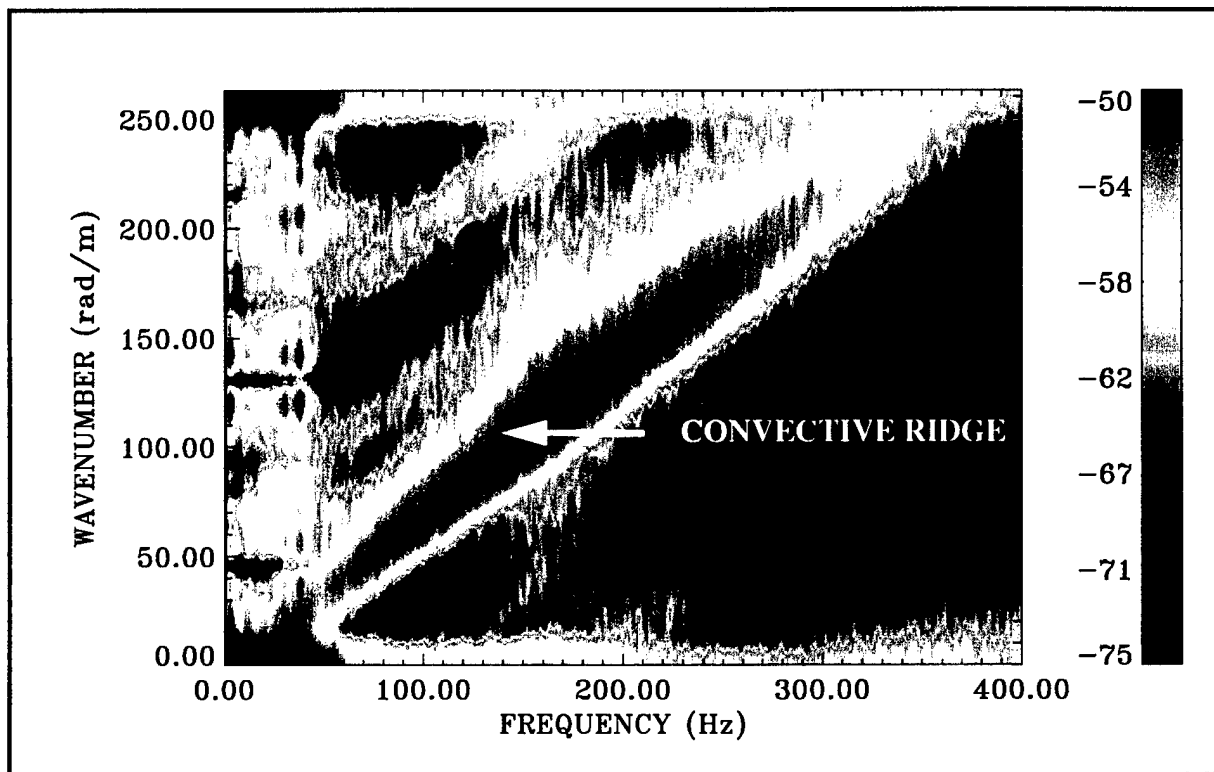
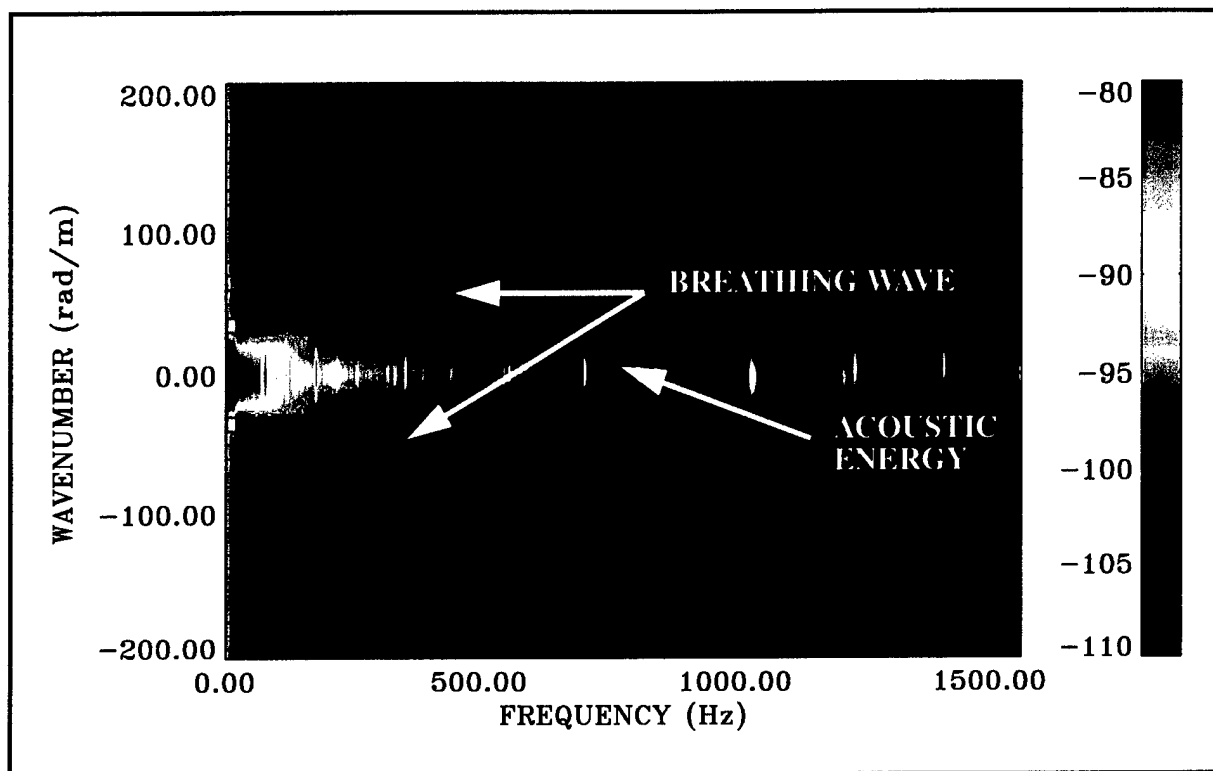
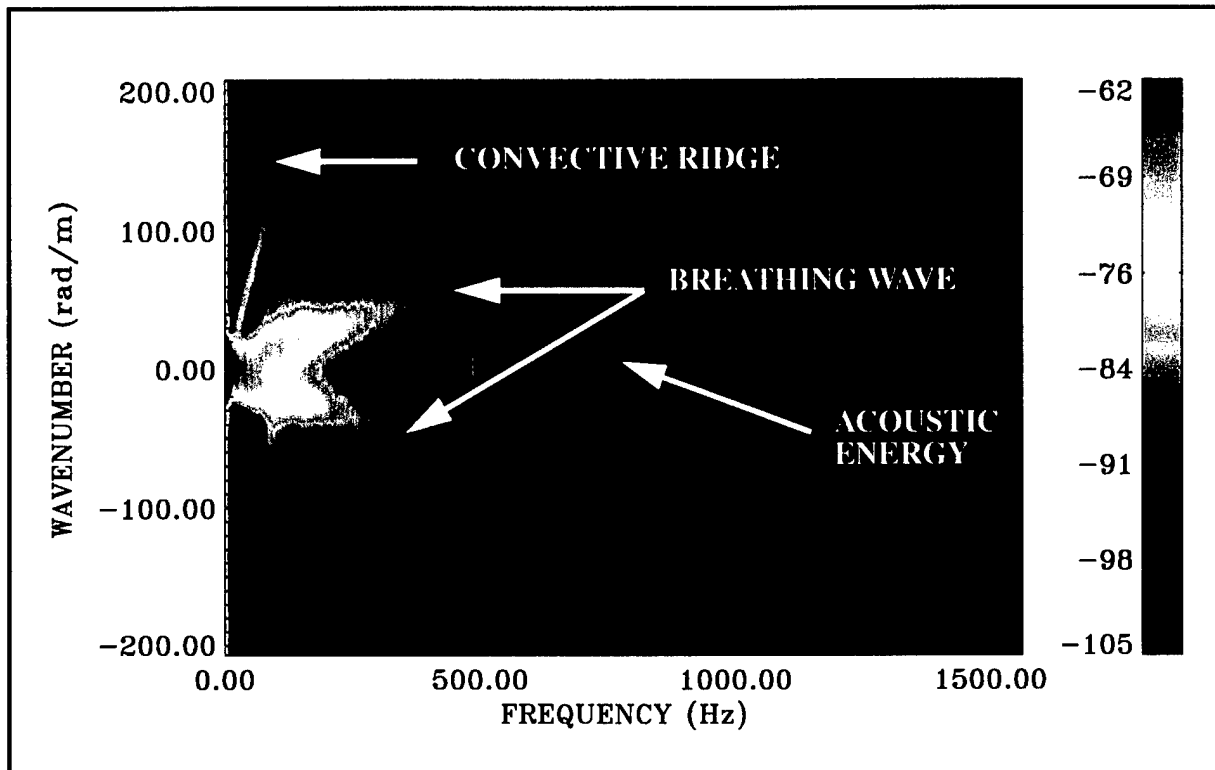


Figure 20. ABC Experimental Raw Data $P_o(k,\omega)$ at a 20-knot Flow Speed



*Figure 21. OFC Experimental Raw Data $P_i(k, \omega)$
from the High- k Wavenumber Filter
at a 5-knot Flow Speed*



*Figure 22. OFC Experimental Raw Data $P_i(k, \omega)$
from the High-k Wavenumber Filter
at a 10-knot Flow Speed*

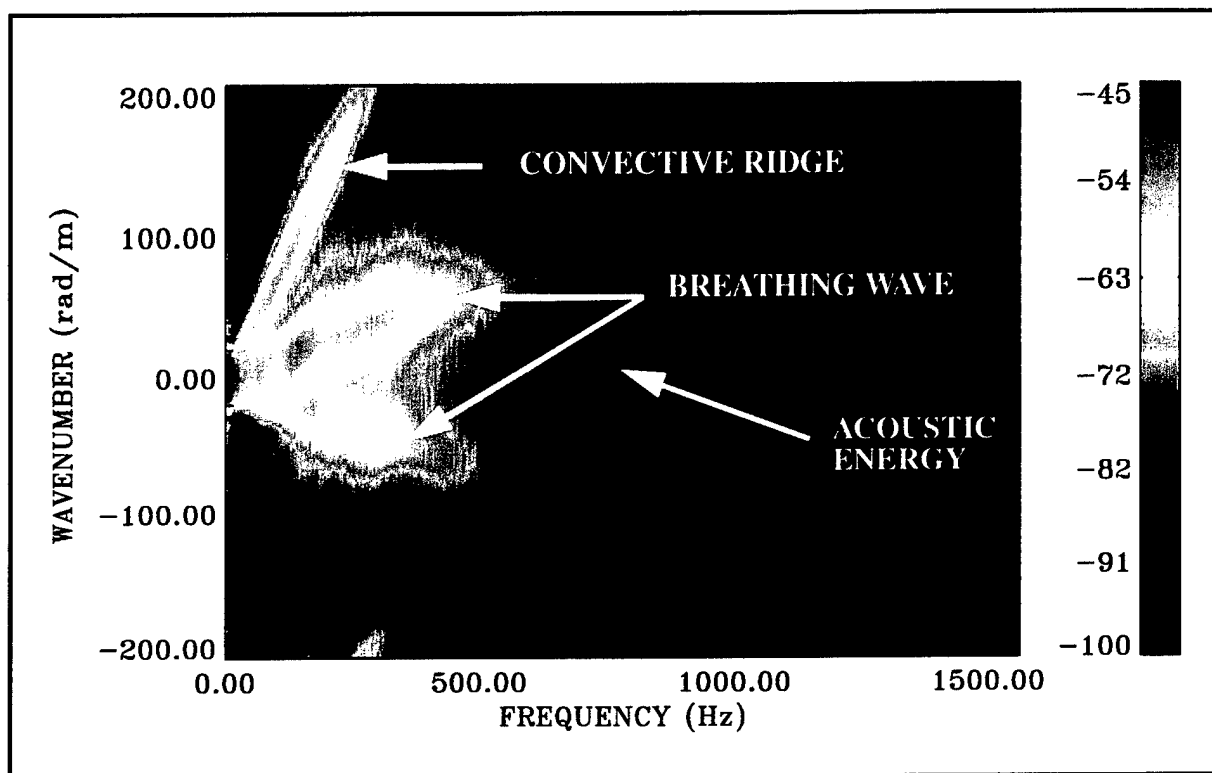


**Figure 23. OFC Experimental Raw Data $P_i(k, \omega)$
from the High- k Wavenumber Filter
at a 20-knot Flow Speed**

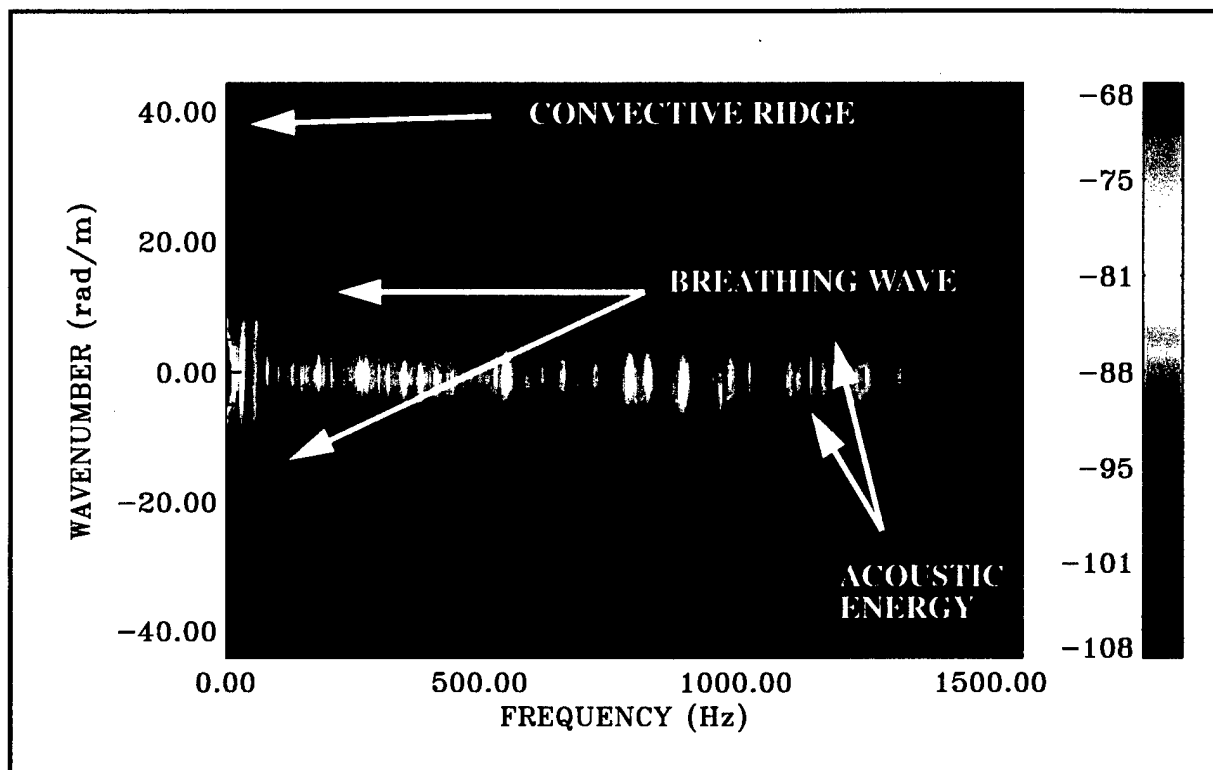


**Figure 24. OFC Experimental Raw Data $P_i(k, \omega)$
from the Medium-k Wavenumber Filter
at a 5-knot Flow Speed**

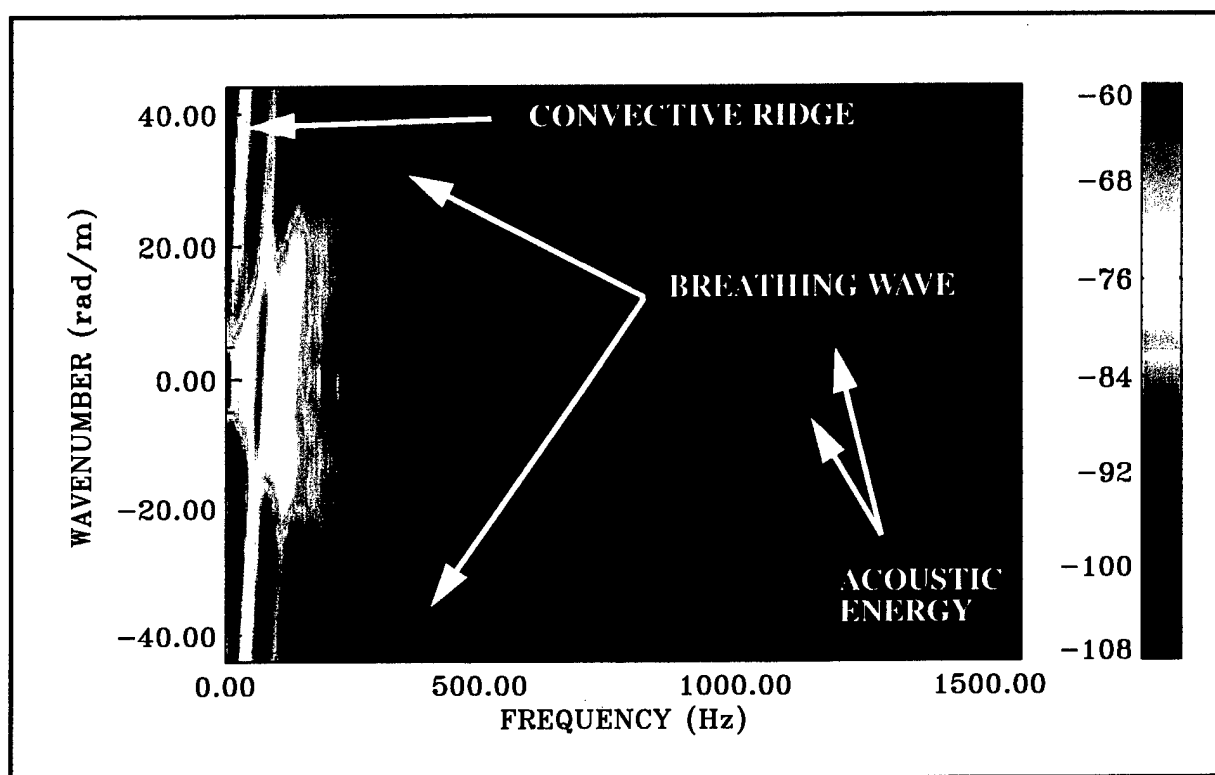


*Figure 25. OFC Experimental Raw Data $P_f(k, \omega)$
from the Medium-k Wavenumber Filter
at a 10-knot Flow Speed*

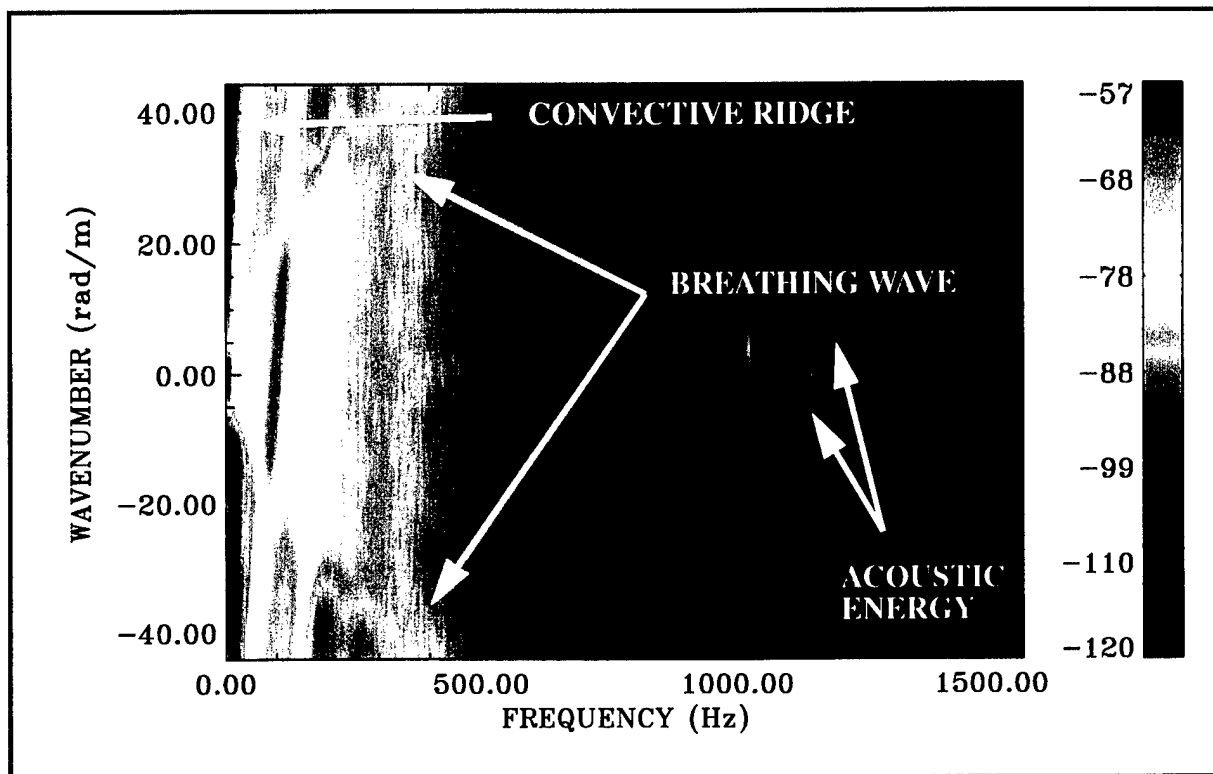


*Figure 26. OFC Experimental Raw Data $P_f(k, \omega)$
from the Medium-k Wavenumber Filter
at a 15-knot Flow Speed*

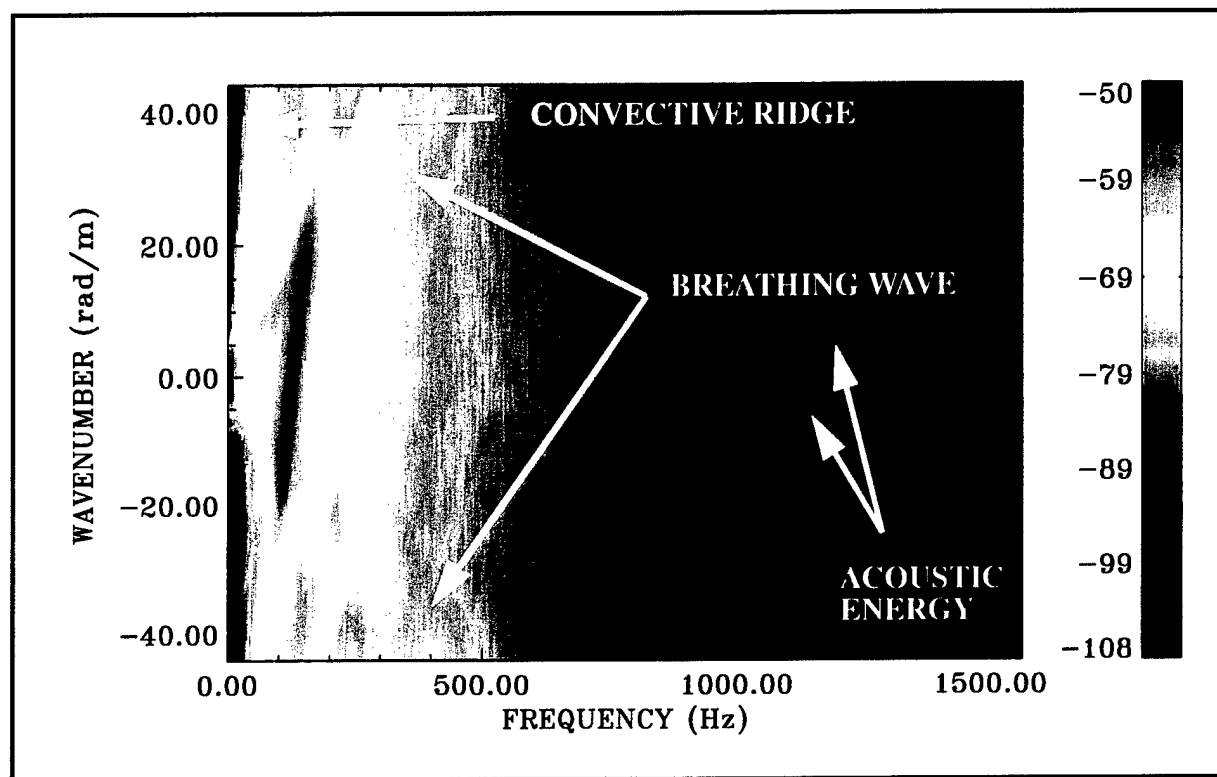


*Figure 27. OFC Experimental Raw Data $P_i(k, \omega)$
from the Medium-k Wavenumber Filter
at a 20-knot Flow Speed*

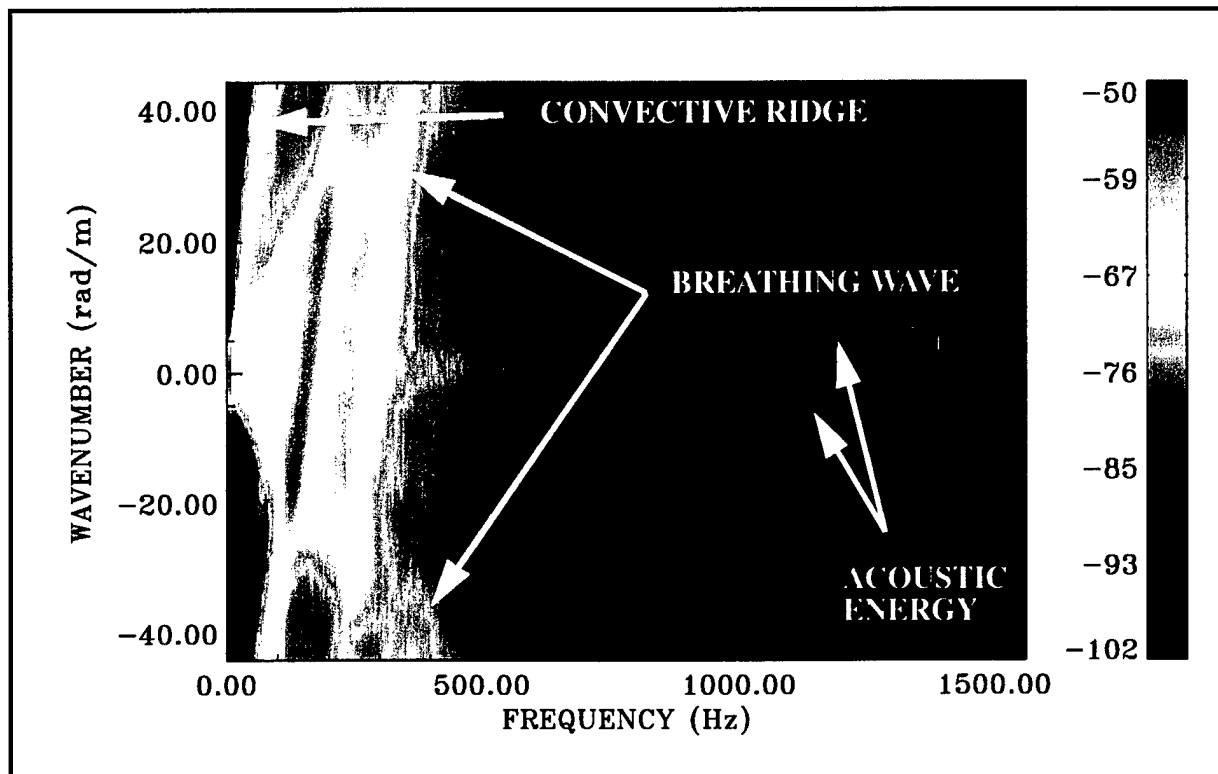


**Figure 28. OFC Experimental Raw Data $P_i(k, \omega)$
from the Medium- k Wavenumber Filter
at a 25-knot Flow Speed**

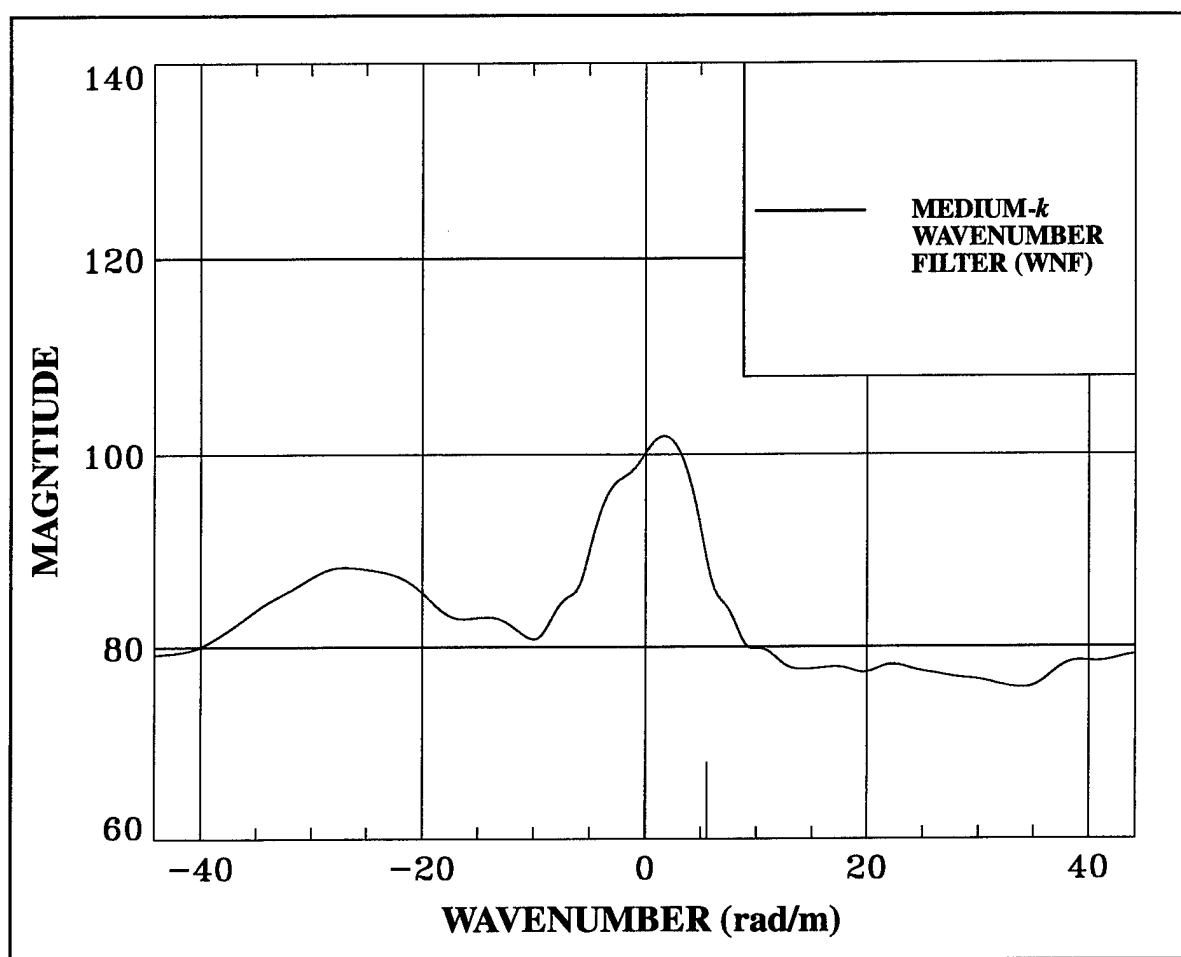


Figure 29. OFC Medium-k Wavenumber-Filter Frequency Cut from Figure 24 at 9.16 Hz and a 5-knot Flow Speed for Uncorrected Surface-Generated Pressure Effects
(Magnitude = $10 \log(P_i^2)$ re $\mu Pa^2/Hz/rad/m$)

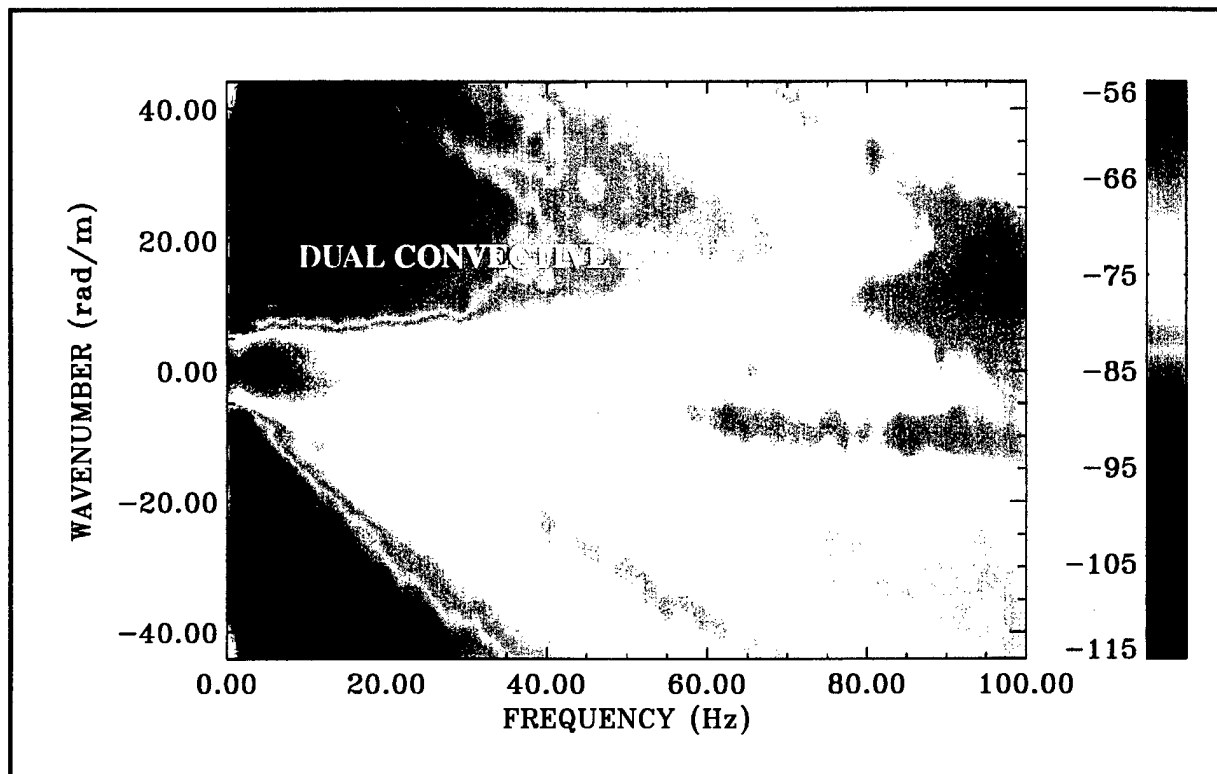


Figure 30. OFC Experimental Raw Data $P_i(k, \omega)$ from the Medium- k Wavenumber Filter at a 20-knot Flow Speed Showing the Dual Convective Ridge (Color Image)

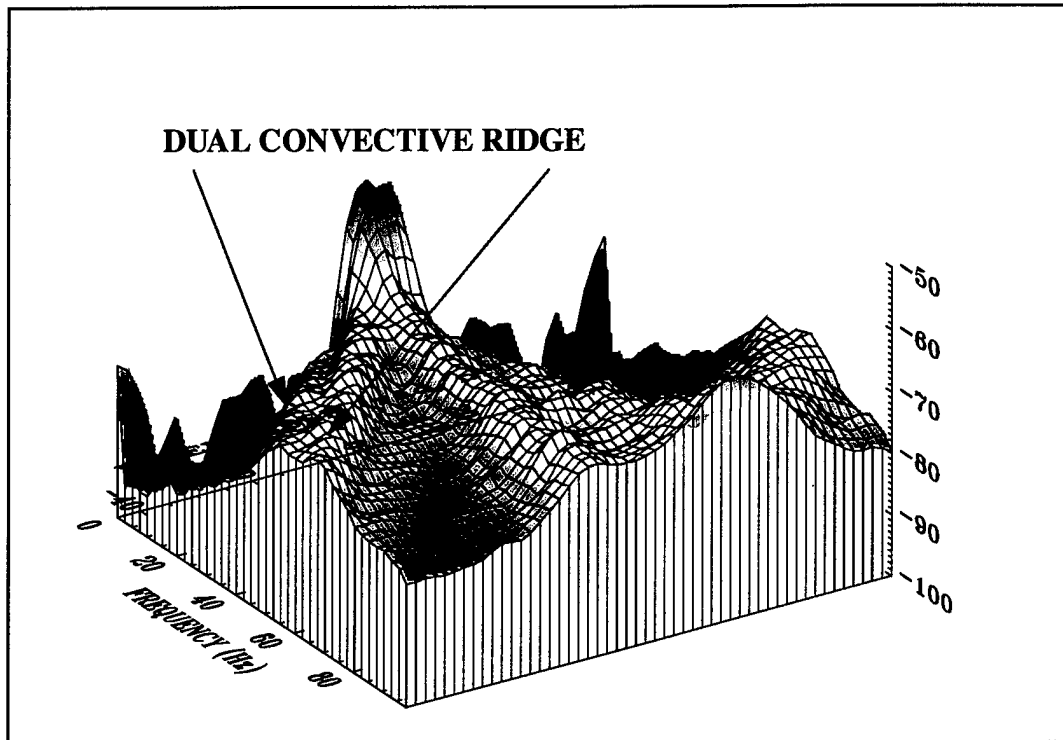


Figure 31. OFC Experimental Raw Data $P_i(k, \omega)$ from the Medium- k Wavenumber Filter at a 20-knot Flow Speed Showing the Dual Convective Ridge (Wire Frame)

CALIBRATED DATA FROM DIRECT TURBULENT BOUNDARY LAYER PRESSURE FIELD MEASUREMENTS

LOW-WAVENUMBER OIL-FILLED CYLINDER DATA

Even though puzzling behavior was observed from the medium- k wavenumber filter when it was used for high-wavenumber convective ridge measurements, this filter remains a very useful tool for low-wavenumber pressure measurements. Low-wavenumber data from all the OFC sensors are compared in figure 32. These data have been normalized to spectral levels with respect to wavenumber and frequency using the beamwidth correction given in table 4; pressure units are then $\mu\text{Pa}^2/\text{Hz}/\text{rad}/\text{m}$. The same normalization is maintained throughout this report.

Table 4. Sensor Aperture Corrections for Spectral Level Normalization

Sensor	Aperture Length (m)	Wavenumber Measurement Range (rad/m)	Aperture Shading Type	Aperture Width in Wavenumber k (rad/m)	Beamwidth Correction (dB)
ABC	0.764	± 131	Taylor (3 @ 26 dB)	9.18	9.63
HK2	0.488	± 206	Hanning	19.4	11.10
MK2	2.276	± 44	Hanning	4.14	6.17
SCH	17.254	± 0.18	Uniform	0.364	-4.38

Comparison of Wavenumber Filters—Spectral Levels

The striking feature of the curves in figure 32 is that they all collapse and overlay one another, even though the data were collected from arrays with different aperture widths in wavenumber (table 4). The fact that they all collapsed, when normalized to spectral level, is proof that the arrays did in fact measure uncorrelated flow noise.

Data from the medium- k filter are plotted up to 55 Hz; above this frequency, the array aliases convective energy and contaminates the low-wavenumber level. Unaliased high- k filter data are plotted from 5 to 1562 Hz. The single-channel 56.6-foot hydrophone measures flow noise up to 400 Hz and then becomes contaminated with acoustic energy.

In summary, from 5 to 400 Hz, all the OFC sensors have measured uncorrelated flow noise that scales with aperture width. These data are of very high quality and are suitable for use in TBL wall pressure model derivation or verification. The only region that is suspect is the 5- to 15-Hz range. There is a possibility that these 5-15 Hz levels are influenced to some degree by vibration, which is discussed in the next section.

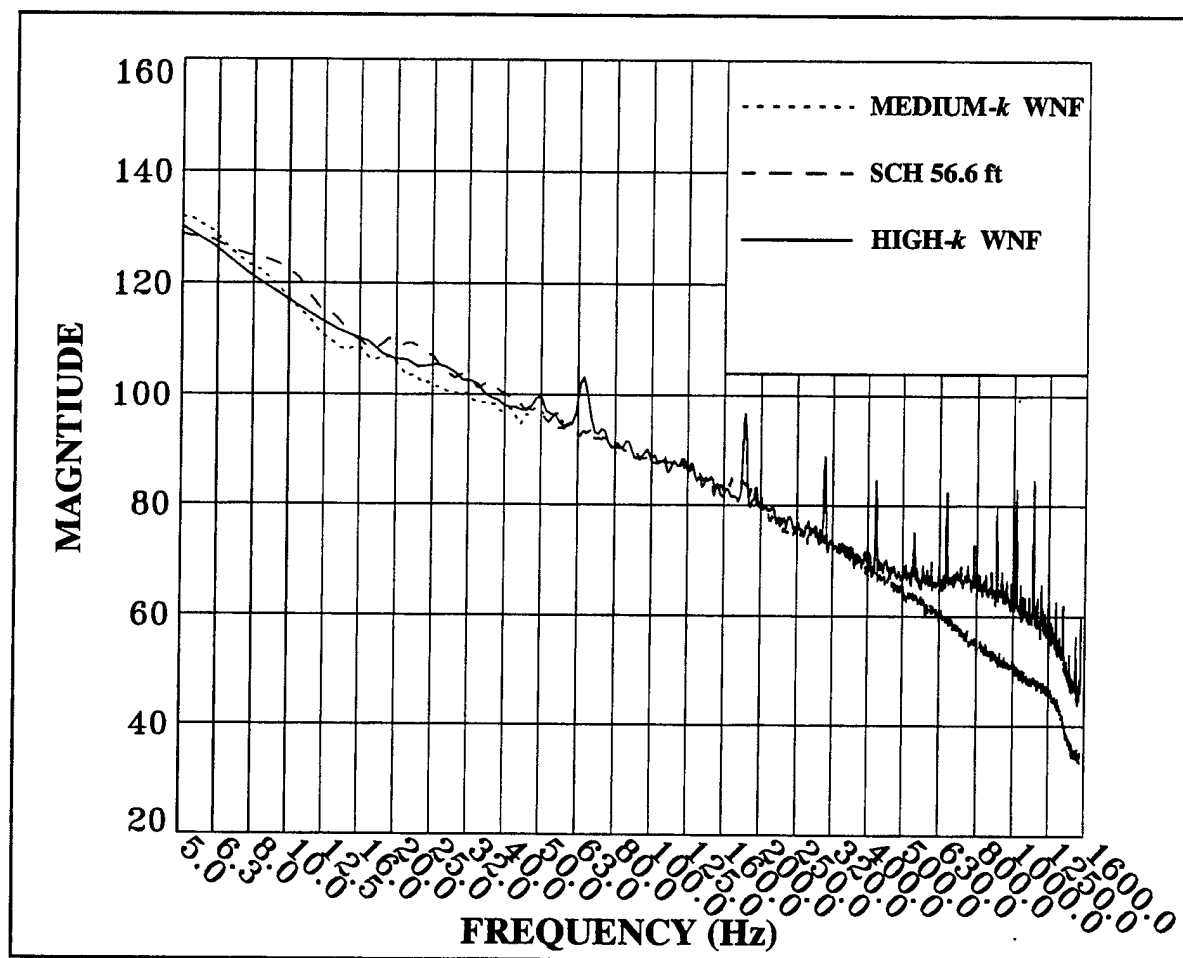


**Figure 32. Comparison of OFC Low-Wavenumber Pressure Levels
from Wavenumber Filters at a 20-knot Flow Speed
(Magnitude = $10 \log(P_i^2)$ re $\mu\text{Pa}^2/\text{Hz}/\text{rad}/\text{m}$)**

COMPARISON OF CONVECTIVE RIDGE AND LOW-WAVENUMBER LEVELS

In figure 33, the convective ridge level from the ABC array has been included with the OFC data shown in figure 32. Referring back to figure 2, notice how the convective ridge emanates from the origin of the surface ($k = 0, \omega = 0$), which is coincident with the low wavenumber at that point. It is therefore reasonable to expect the ABC data to merge with the OFC data at low frequency. For reasons that will be established later, the ABC wall pressure data are only available down to 45 Hz at the 20-knot flow speed. Extrapolating these ABC data (constant-level dashed line) lower in frequency shows that the OFC data will exceed the ABC data below 12.5 Hz, which indicates that the OFC pressure data could be influenced by vibration and may not be truly dominated by flow noise in this low-frequency region. The ABC data suggest that the OFC pressure data below 16 Hz should be subordinated to an extrapolation of ABC pressure data. A combination of ABC levels and OFC levels should be used to extrapolate the low-wavenumber merge, as indicated by the bold dashed line on figure 33.

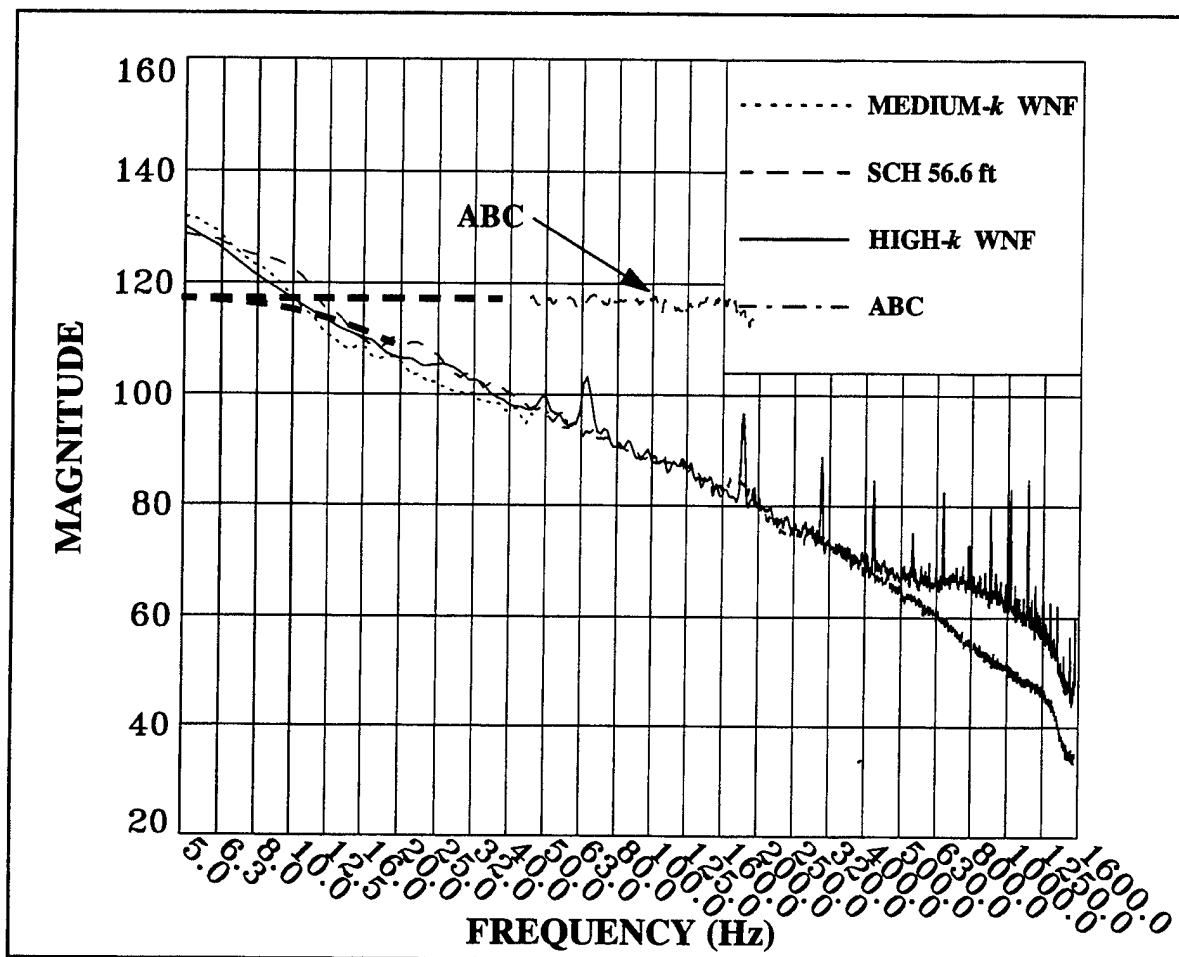


Figure 33. Comparison of OFC Low-Wavenumber Pressure Levels and ABC Convective Ridge Levels from Wavenumber Filters at a 20-knot Flow Speed (OFC Magnitude = $10 \log(P_i^2)$ re $\mu\text{Pa}^2/\text{Hz}/\text{rad}/\text{m}$ and ABC Magnitude = $10 \log(P_o^2)$ re $\mu\text{Pa}^2/\text{Hz}/\text{rad}/\text{m}$)

CONVECTIVE RIDGE LEVELS

The experimental raw data, shown in figures 18 through 20 for the ABC array, are calibrated as previously discussed with equation (20). The calibration is performed by adding the correction, evaluated in figure 15, to figures 18 through 20 for each flow speed. An example of a fully calibrated 20-knot flow speed is shown in figure 34. The calibration is performed, and the amplitude of the convective ridge is displayed in figure 35.

Each of the curves in figure 35 is composed of a wall-shear-stress-dominated region (low frequency) and a wall-pressure-dominated region (high frequency). Based on the theoretical response of the ABC shown in figures 4 and 5, the wall-shear-stress-dominated region was removed. The portion that remains is mainly dominated by the wall pressure and is shown in figure 36.

The 5- and 10-knot flow speed curves in figure 35 could possibly be influenced by the wall shear stress. The first clue to the wall shear stress influence is the sloped shape in frequency. This possibility will be further explored in a later section.

Cuts in frequency that have been made for the fully calibrated ABC data are displayed in figures 37 through 40 for the 5-, 10-, 15-, and 20-knot flow speeds, respectively. The asymmetry of the convective ridge is clearly seen in these figures. However, the width of the array response does not allow the true slope of the low-wavenumber side of the ridge to be determined accurately. Note that at 15 and 20 knots (figures 39 and 40) the shape of the low-wavenumber bump and the low-wavenumber side of the convective ridge follow the same curve, which is simply the impulse response of the array aperture; in this case, the low-wavenumber side of the convective ridge has not been accurately resolved. This is less true at the 5- and 10-knot flow speeds (figures 37 and 38), where the convective ridge has been accurately resolved. More information might be obtained from the medium- k wavenumber filter, which has a much narrower response in wavenumber, as can be seen in figure 29; however, there is limited resolution of the convective ridge, which makes it difficult to determine the slope on the low-wavenumber side.

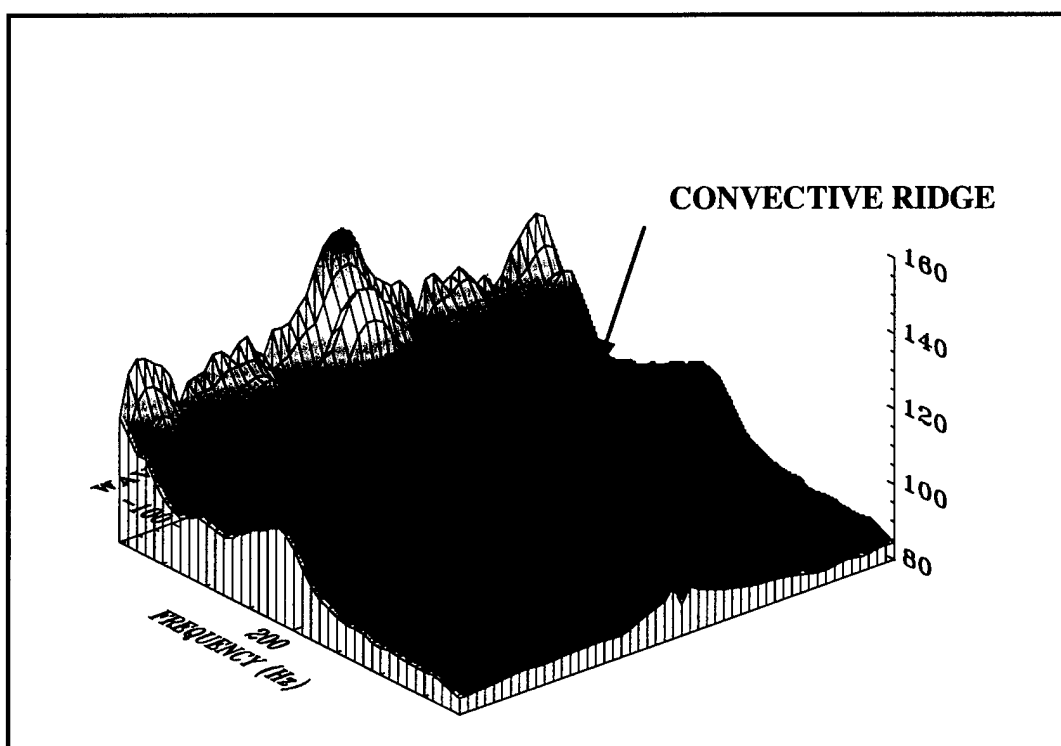


Figure 34. ABC Calibrated Pressure Level at a Flow Speed of 20 knots
(Magnitude = $10 \log(P_o^2)$ re $\mu\text{Pa}^2/\text{Hz}/\text{rad}/\text{m}$)

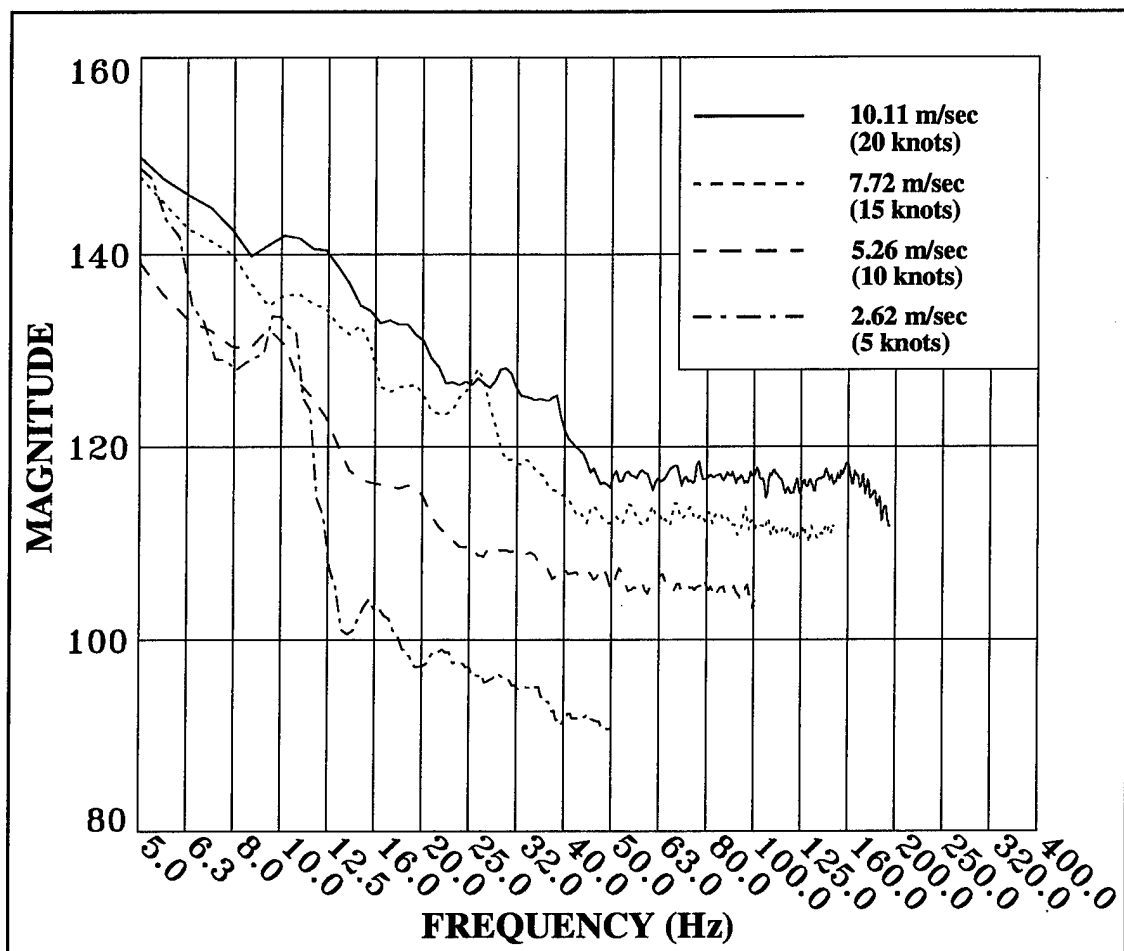


Figure 35. Comparison of Fully Calibrated Convective Ridge Pressure Levels at Various Flow Speeds (Magnitude = $10 \log(P_o^2)$ re $\mu\text{Pa}^2/\text{Hz}/\text{rad}/\text{m}$)

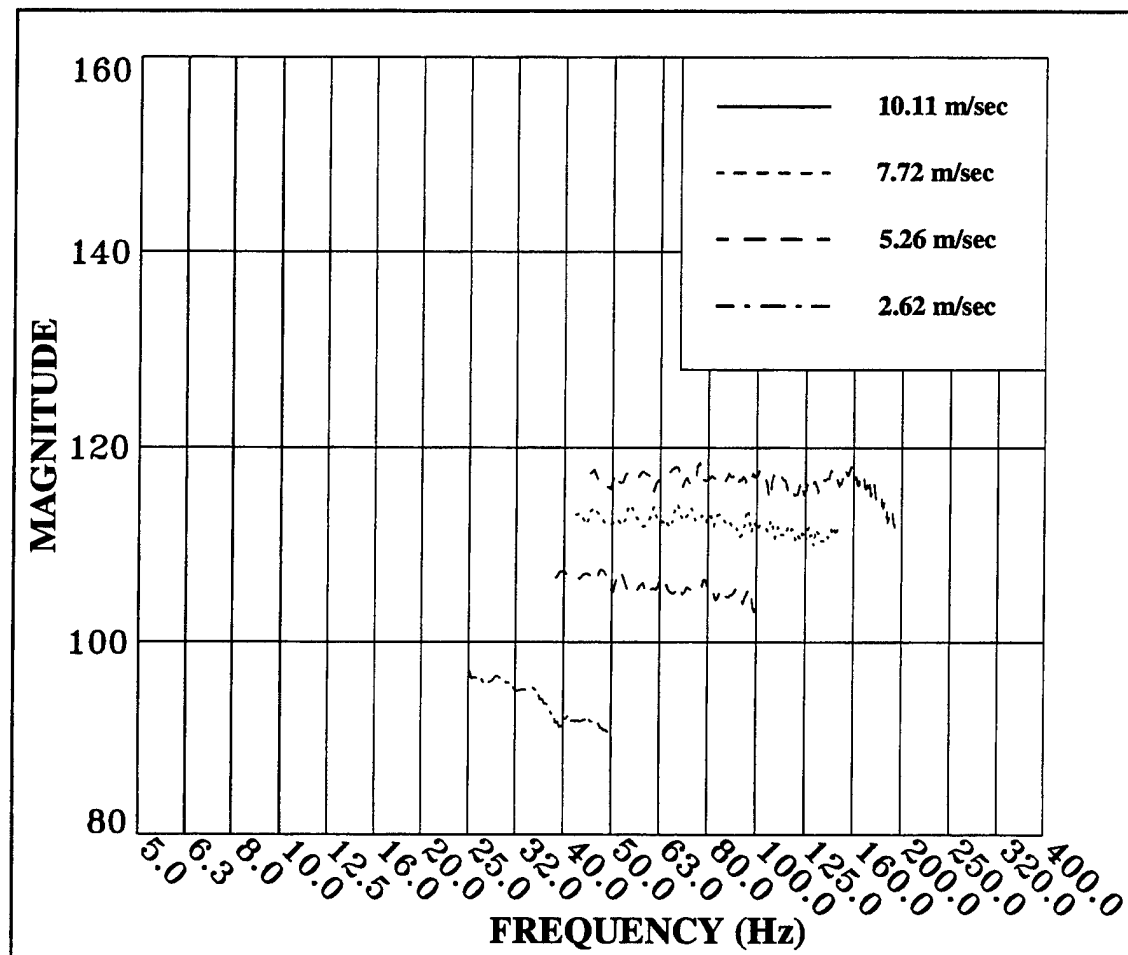


Figure 36. Comparison of Fully Calibrated Convective Ridge Pressure Levels for the Wall Pressure Component Only
(Magnitude = $10 \log(P_o^2)$ re $\mu Pa^2/Hz/rad/m$)

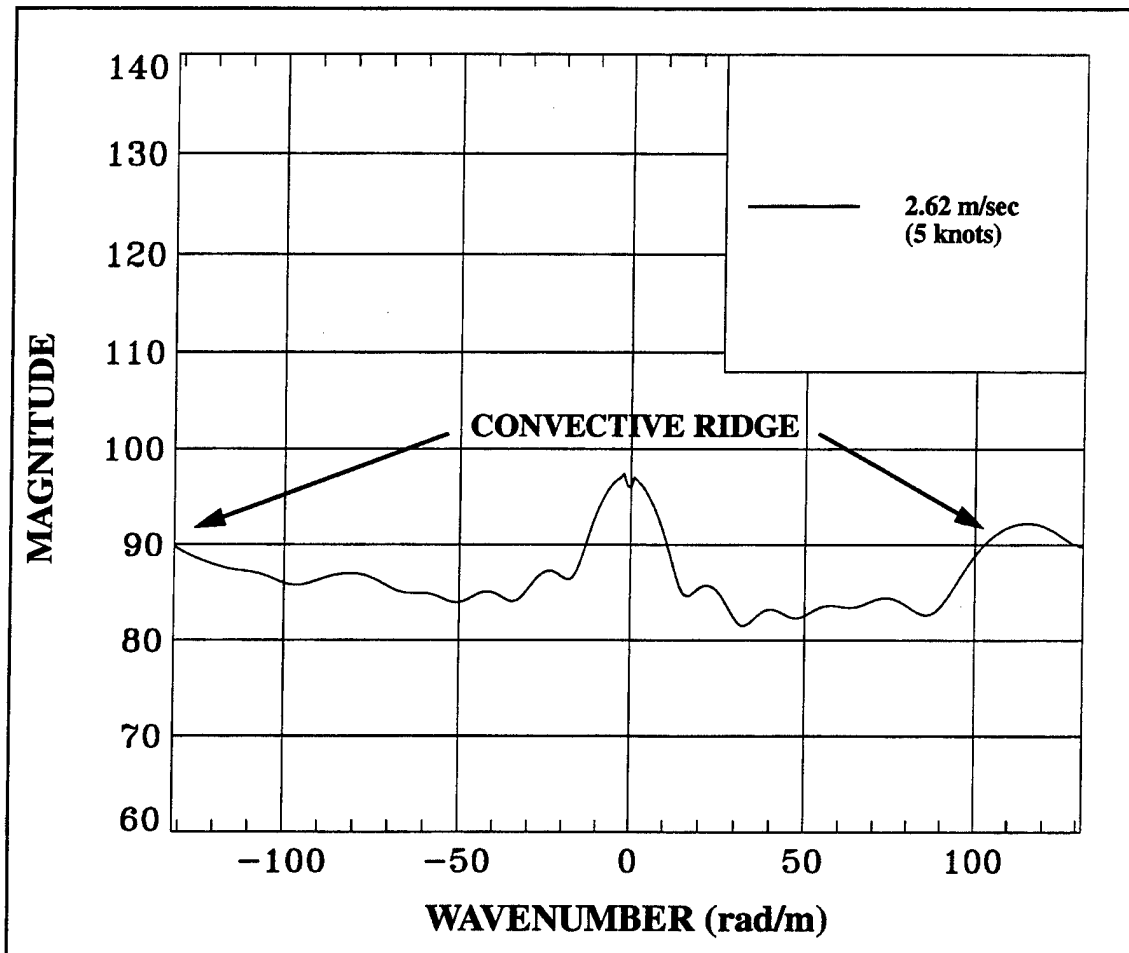


Figure 37. Cut in Frequency at 44 Hz for Fully Calibrated Wall Pressure Component at a 5-knot Flow Speed (Magnitude = $10 \log(P_o^2)$ re $\mu Pa^2/Hz/rad/m$)

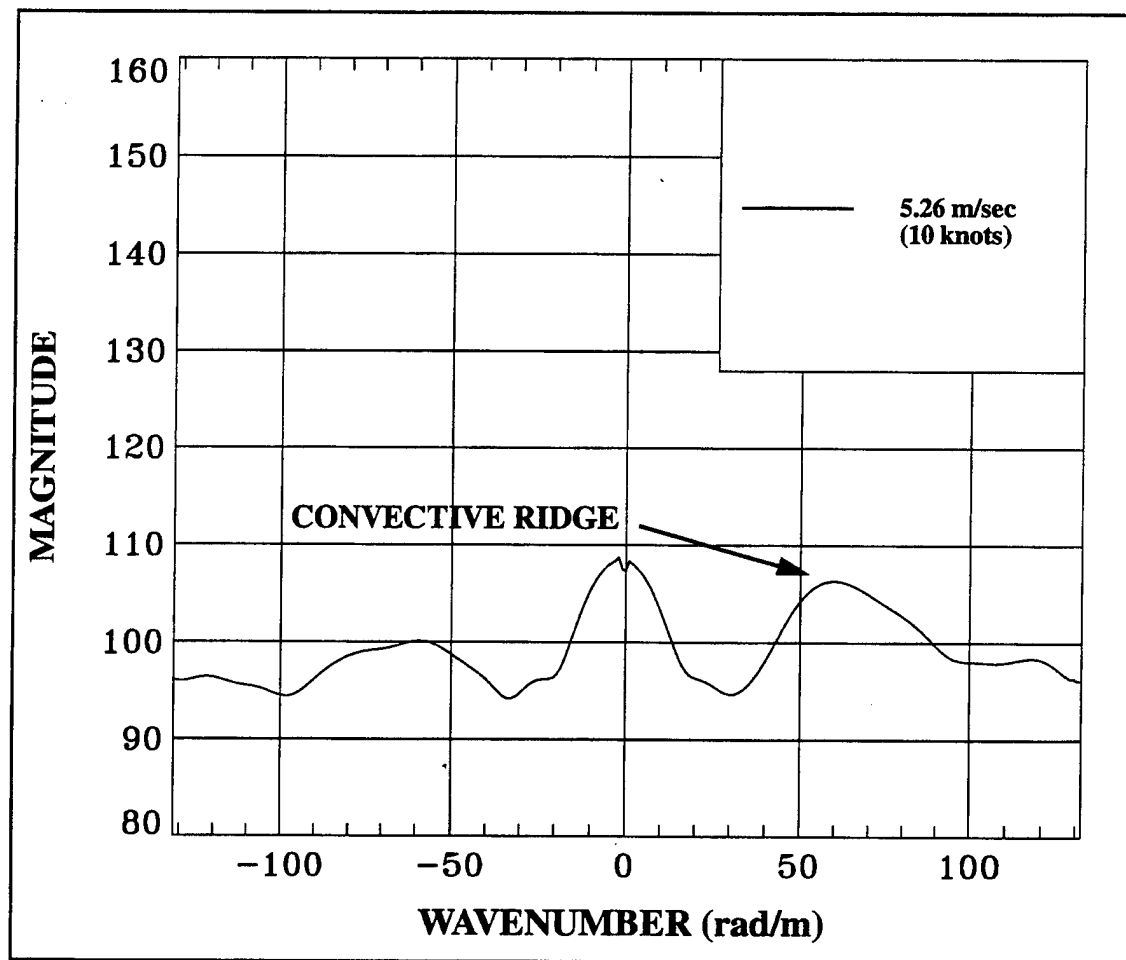


Figure 38. Cut in Frequency at 45 Hz for Fully Calibrated Wall Pressure Component at a 10-knot Flow Speed (Magnitude = $10 \log(P_o^2)$ re $\mu Pa^2/Hz/rad/m$)

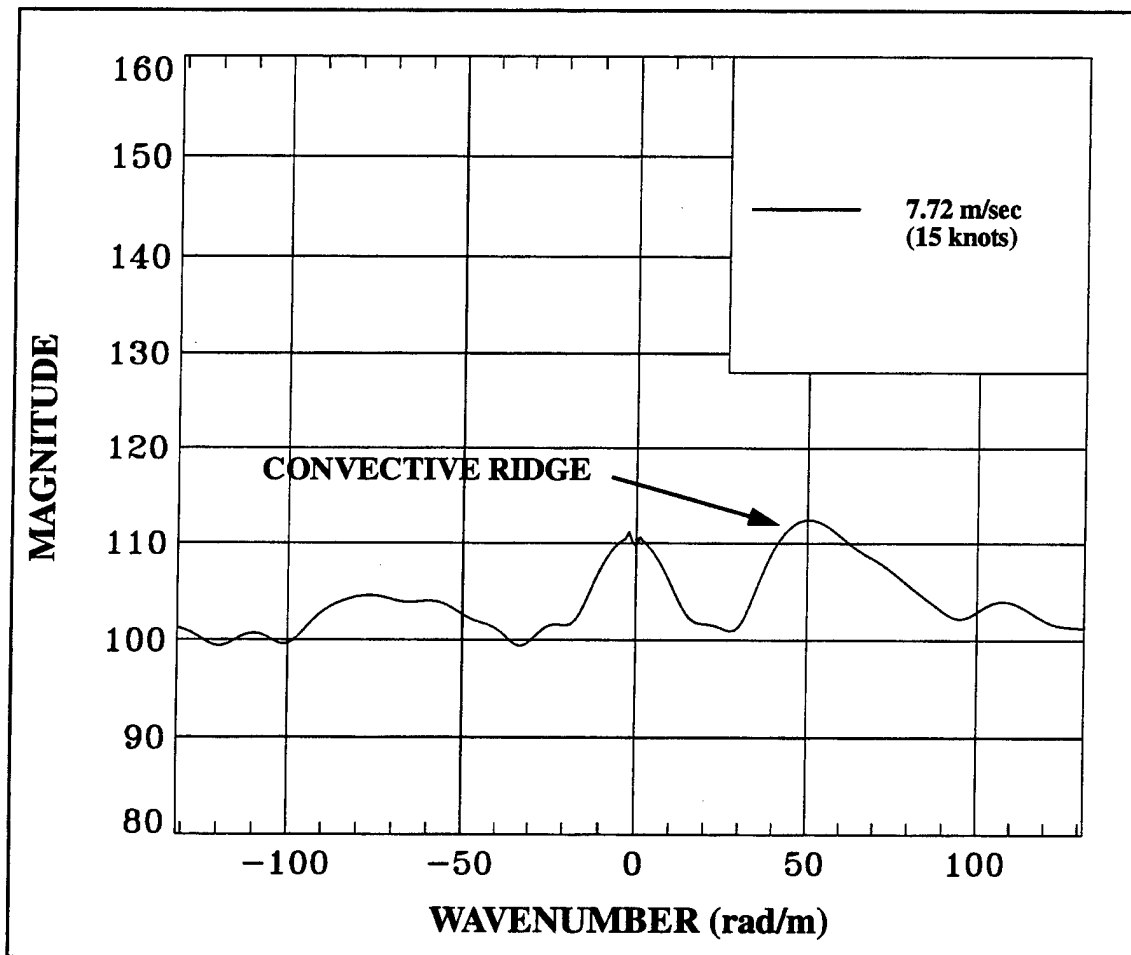


Figure 39. Cut in Frequency at 59 Hz for Fully Calibrated Wall Pressure Component at a 15-knot Flow Speed (Magnitude = $10 \log(P_o^2)$ re $\mu Pa^2/Hz/rad/m$)

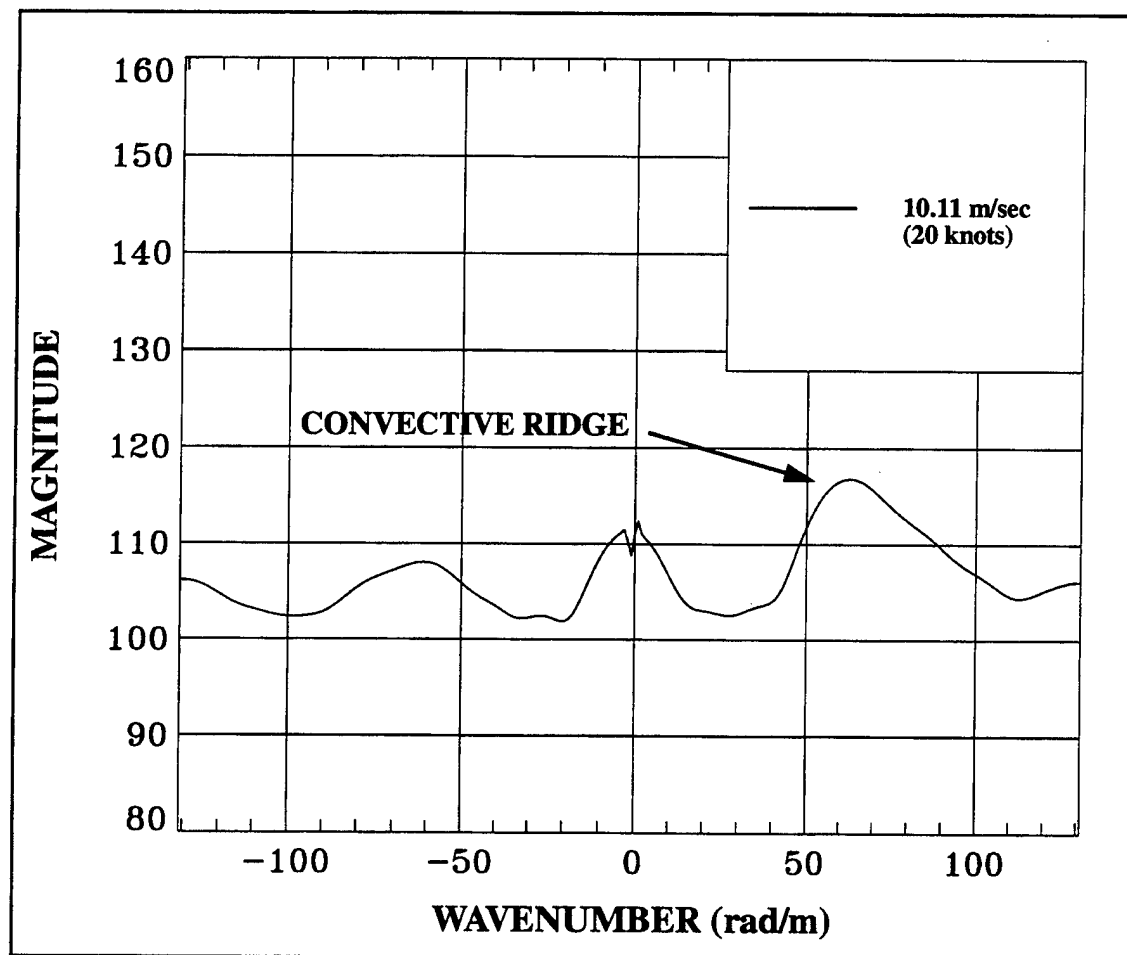


Figure 40. Cut in Frequency at 94 Hz for Fully Calibrated Wall Pressure Component at a 20-knot Flow Speed (Magnitude = $10 \log(P_o^2)$ re $\mu Pa^2/Hz/rad/m$)

HOSE WALL TRANSFER FUNCTION CALIBRATION

Until the direct TBL wall pressure measurements were made, the OFC hose wall transfer function for wall pressure remained a theoretical calculation, heavily dependent on structural modeling and void of direct calibration. The calibration undertaken here is the first one that has been accomplished for a real cylinder; it is documented with an invention disclosure that is patent pending under Navy Case No. 78106.⁴ The calibration seeks to verify the rolloff of the dynamic mechanical structural response shown in the upper surface of figure 3.

The hose transfer function has been defined in equation (23) and will be repeated here for clarity as equation (27):

$$T_{OFC}(k, \omega, a) = \frac{P_i(k, \omega, a)}{P_o(k, \omega, b)} . \quad (27)$$

Substituting equation (26) for $P_i(k, \omega, a)$ and equation (19) for $P_o(k, \omega, b)$ into equation (27) gives the following result for the hose wall transfer function:

$$T_{OFC}(k, \omega, a) = \frac{\frac{V_m^2(k, \omega, a)}{S^2} \left[\frac{1}{H_{OFC}(k) \left(1 + \frac{P_s^2(k, \omega, b)}{P_o(k, \omega, b)} \right)} \right]}{\frac{V_m^1(k, \omega, \bar{b})}{S^1} \left[\frac{1}{\left(1 + \frac{P_s^1(k, \omega, b)}{P_o} \right) (T_{ABC}(k, \omega, \bar{b}) H_{ABC}^2(k))} \right]} . \quad (28)$$

It is important to note that $P_i(k, \omega, a)$ and $P_o(k, \omega, b)$ are not the pressures directly measured by the sensors in the ABC and OFC arrays. These arrays respond to the total pressure

and thus require the removal of the surface-generated pressure effect and the sensor aperture function effect to obtain an accurate calibration of the hose wall transfer function.

The calibration is performed by dividing the pressures, as shown in equation (28). In figure 41, this is done at the convective ridge location for the 100-Hz case. The calibration is then performed along the convective ridge slope in the wavenumber-frequency plane to produce the curve (labeled EXPERIMENT) shown in figure 42.

Two models for the OFC transfer function are also plotted in figure 42 for comparison: one is an isotropic dynamic elasticity model from reference 3 and the other is a generally orthotropic shell model with longitudinal reinforcement from reference 2. At high wavenumbers, better agreement is obtained with the shell model.

It is important to retain physics that describe the longitudinal reinforcement of the cylinder wall because this reinforcement influences the breathing wave shape and hence the rolloff at high wavenumbers, which is the principal concern of the hose wall transfer function calibration.

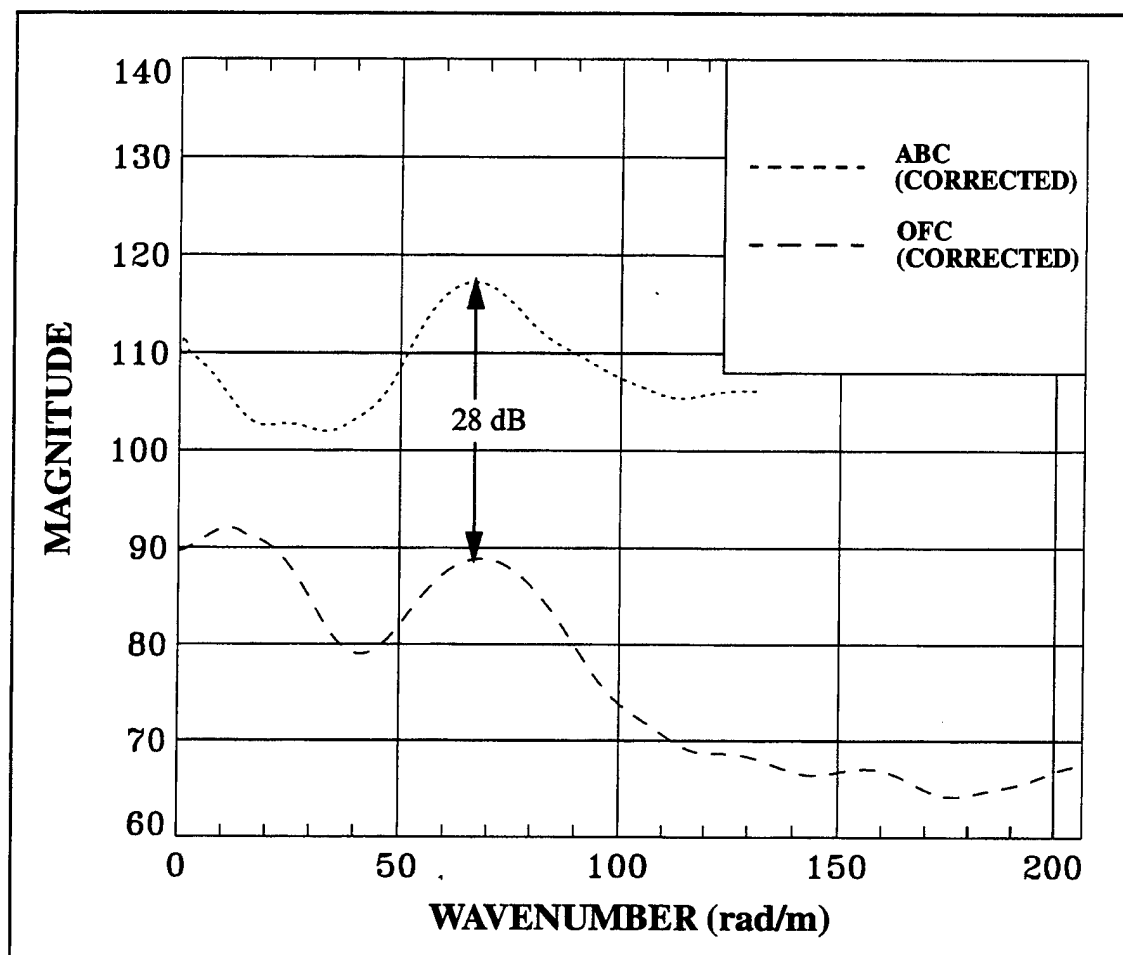


Figure 41. Outer (ABC) and Inner (OFC) Corrected Pressure Levels Used for the Hose Transfer Function Calibration, with Cuts Through the Surfaces at 100 Hz (Magnitude = $10 \log(P^2)$ re $\mu\text{Pa}^2/\text{Hz}/\text{rad}/\text{m}$, Where $P = P_o$ and P_i for the Outer and Inner Pressure Fields, Respectively)

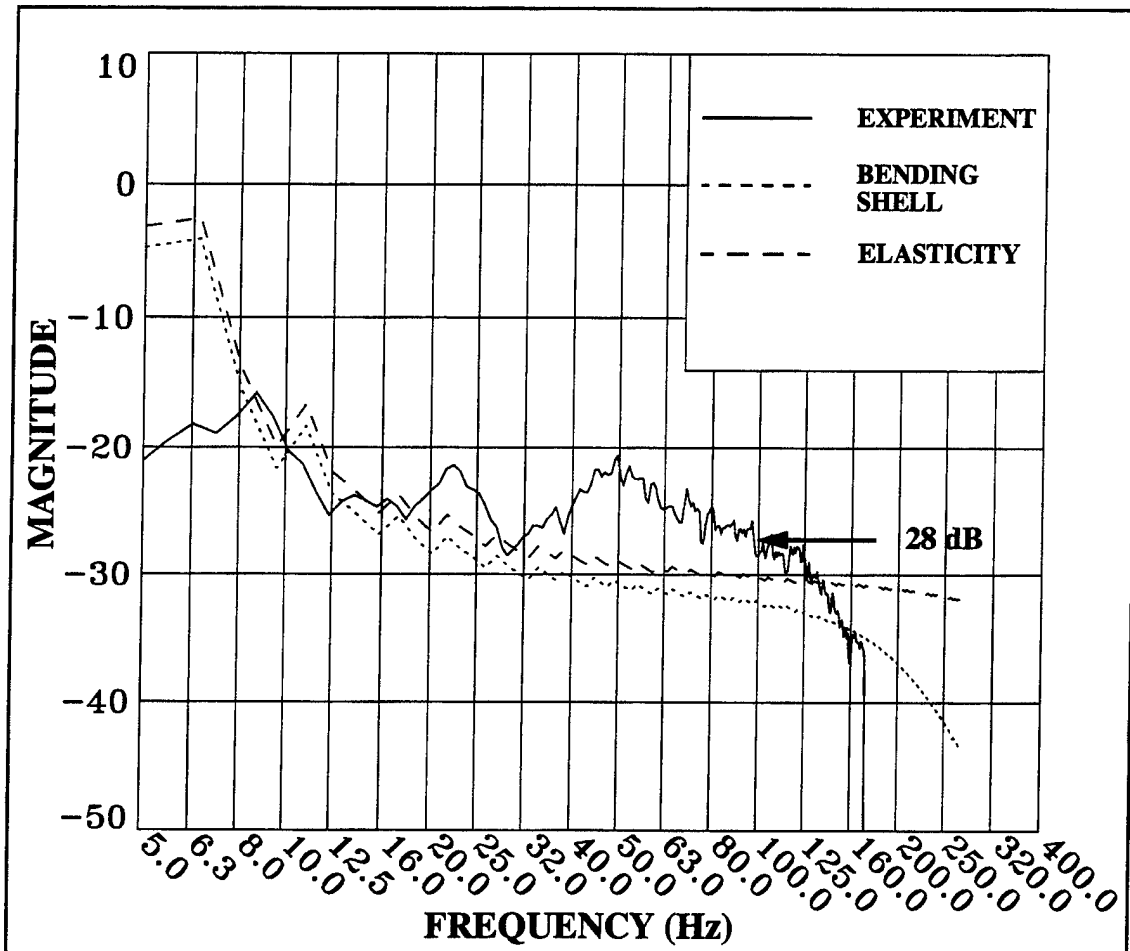


Figure 42. Comparison of Experimental and Theoretical Hose Transfer Function Calibrations at 8.2 m/sec Using the Bending Shell and Elasticity Models
 (Magnitude = $10 \log(P_i/P_o)^2$)

SELF-NOISE MODEL PREDICTIONS USING EXISTING TURBULENCE SOURCE MODEL

COMPARISON OF EXPERIMENTAL DATA AND MODEL PREDICTIONS (AIR-BACKED CYLINDER)

In previous sections, the design of the ABC sensor has been discussed, its response to wall pressure and longitudinal shear stress excitation has been analyzed, and the region that should be dominated by the fluctuating shear component of the TBL and the region that should be governed by the wall pressure component have been estimated. In this section, the measured data are compared with the theoretical predictions to evaluate the TBL source models currently used for noise predictions. Additionally, the accuracy of the predicted performance of the ABC is verified with the data that were actually obtained in the experiment.

The predictions and experiment are compared for flow speeds of 20, 10, and 5 knots. At each flow speed, both wall pressure and longitudinal shear stress simulations are performed.

20 Knots

Wall Pressure Excitation. Equation (1) is used to produce a full beamformed surface simulation for the output of the ABC array. Evaluation of this equation over the unaliased range of the array at ± 131.4 rad/m and 1000 Hz results in the upper image of figure 43. The corresponding experimental data are shown in the lower image of the same figure.

When the amplitude of the convective ridge from each of the images of figure 43 is compared in figure 44, agreement to within 6 dB is achieved above 50 Hz. This is the region where the response of the sensor is dominated by wall pressure excitation. Below 45 Hz, where the array output is dominated by longitudinal shear excitation, the theoretical simulation underpredicts the level measured in the experiment at a 20-knot flow speed.

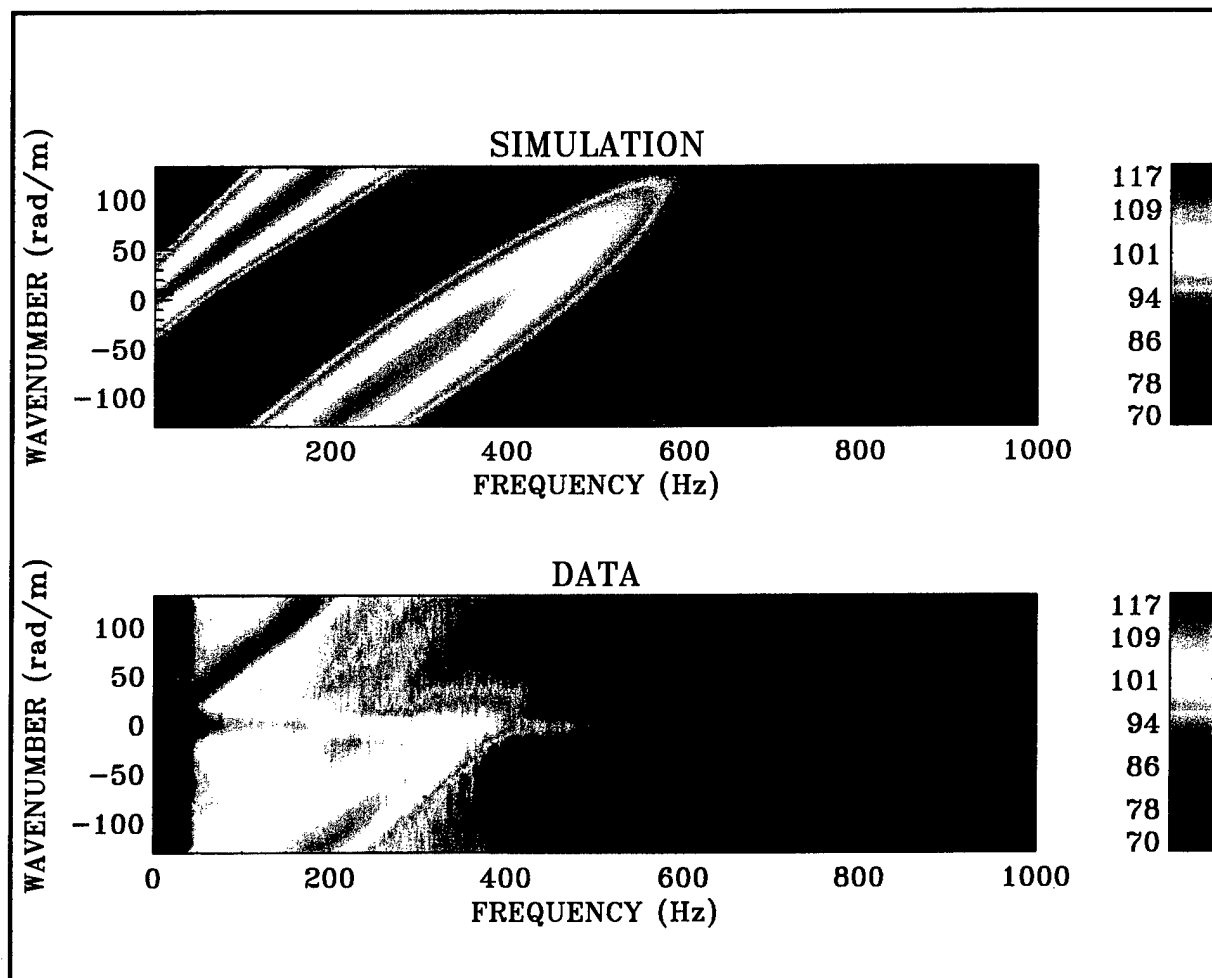


Figure 43. Comparison of Experimental Data $P_o(k,\omega)$ and Wall Pressure Simulation at a Flow Speed of 10.11 m/sec

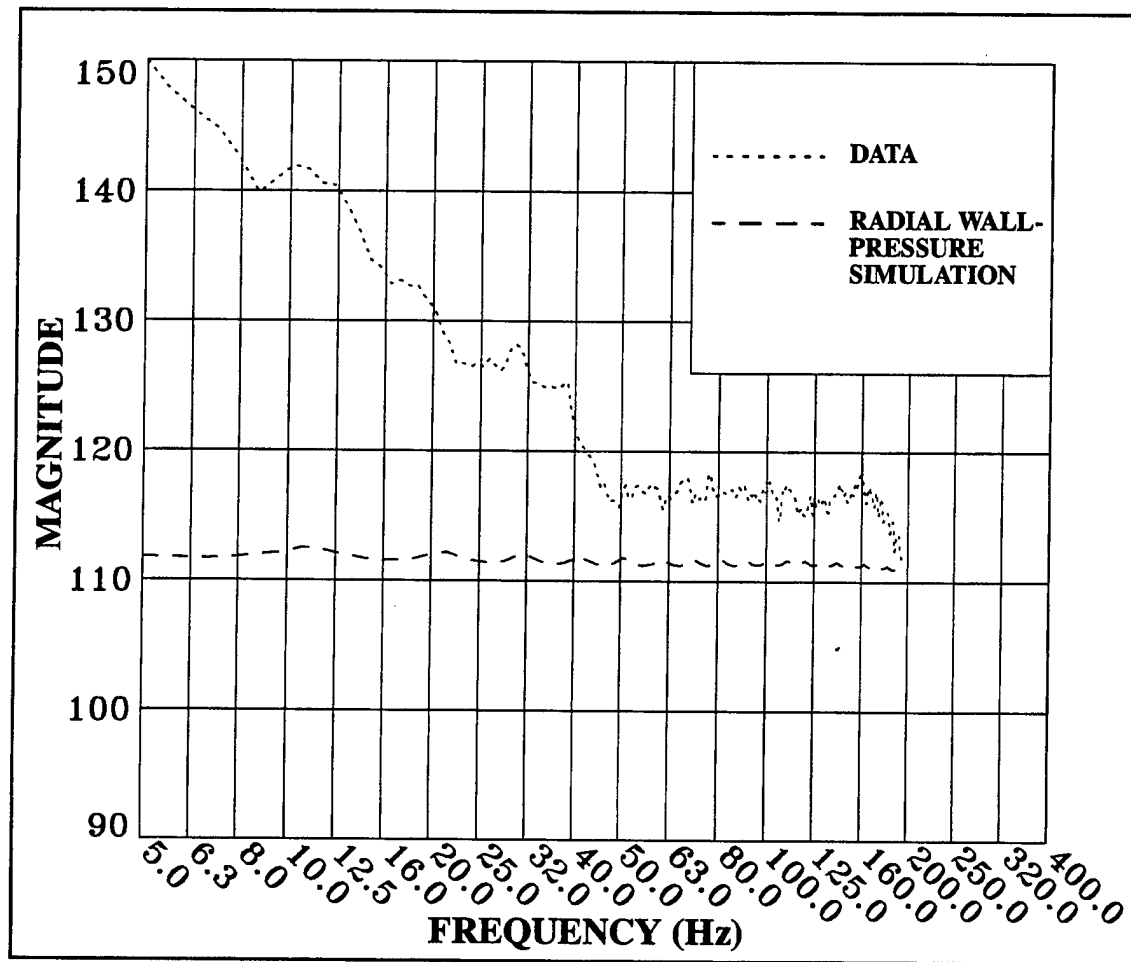


Figure 44. Convective Ridge Magnitude Comparison of Experimental Data and Wall Pressure Simulation at a Flow Speed of 10.11 m/sec
 (Magnitude = $10 \log(P_o(k, \omega)^2)$ re $\mu Pa^2/Hz/rad/m$)

Shear Stress Excitation. A simulation of the array response for a longitudinal shear stress excitation is performed with equation (1) and an appropriate model for the TBL shear forcing function. The resulting beamformed surface is displayed in figure 45 (upper image). The same experimental data file, used in figure 43, is displayed again as the lower image of figure 45.

As was done previously for the wall pressure excitation, the magnitude of the convective ridge of the images in figure 45 is compared in figure 46. In this case, the experimental data and the theoretical prediction can only be compared qualitatively to each other because a suitable shear stress calibration was not applied to the experimental data. Application of a longitudinal shear stress calibration to the experimental data to obtain calibrated levels will be left for future research. If figure 46 is examined again, from approximately 45 Hz and higher, the disparate behavior (different slopes) of the “calibrated levels” and the theoretical prediction is seen. In addition, the experimental data change character very abruptly, becoming flat with increasing frequency. This flat character supports the contention that the sensor is responding to wall pressure above 45 Hz and to some other excitation, possibly shear, below 45 Hz. Another source of the signal existing in the data below 45 Hz could be array sidelobe leakage from the high-level low-wavenumber components of the sensor output.

In figure 47, the wall pressure prediction is shown with the experimental data and shear stress predictions displayed in figure 46. The 45-Hz break point between the sloped low-frequency response and the flat response above 45 Hz is coincidental and should not be construed as a similarity between theory and experiment.

It should be emphasized that applying a single calibration to the experimental data treats the entire output of the sensor as if it were derived from a single excitation source (e.g., wall pressure). If part of the sensor output did not derive from that particular source but rather from another source (such as wall shear stress), then that part would be in the form of a noise response until the proper calibration was applied to correctly depict the amplitude. Note that this approach is not being taken with the analysis of the response of the ABC to the longitudinal component of the TBL, since the response of the ABC to the longitudinal component of the TBL remains uncalibrated throughout this report.

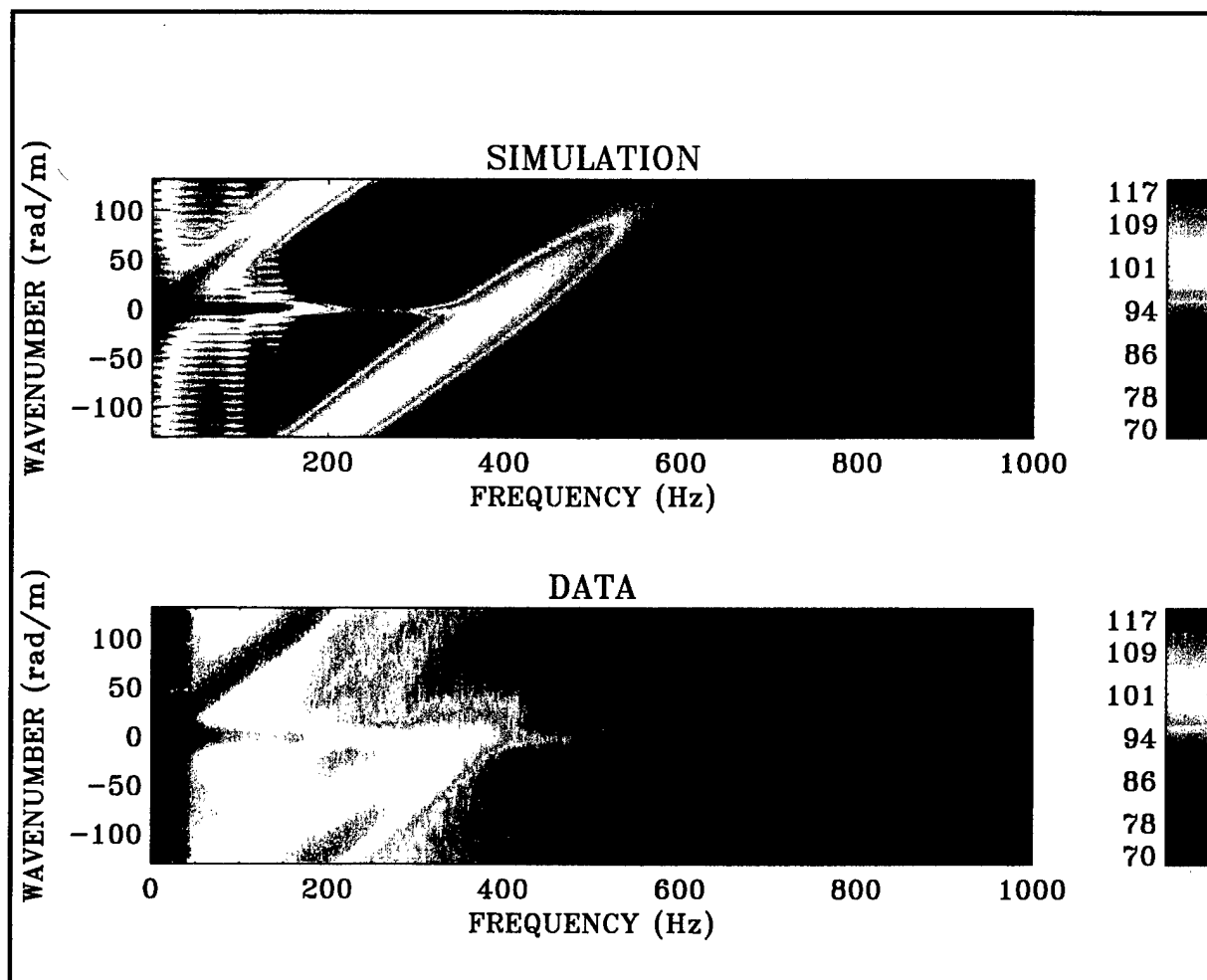


Figure 45. Comparison of Experimental Data $P_o(k, \omega)$ and Wall Shear Stress Simulation at a Flow Speed of 10.11 m/sec

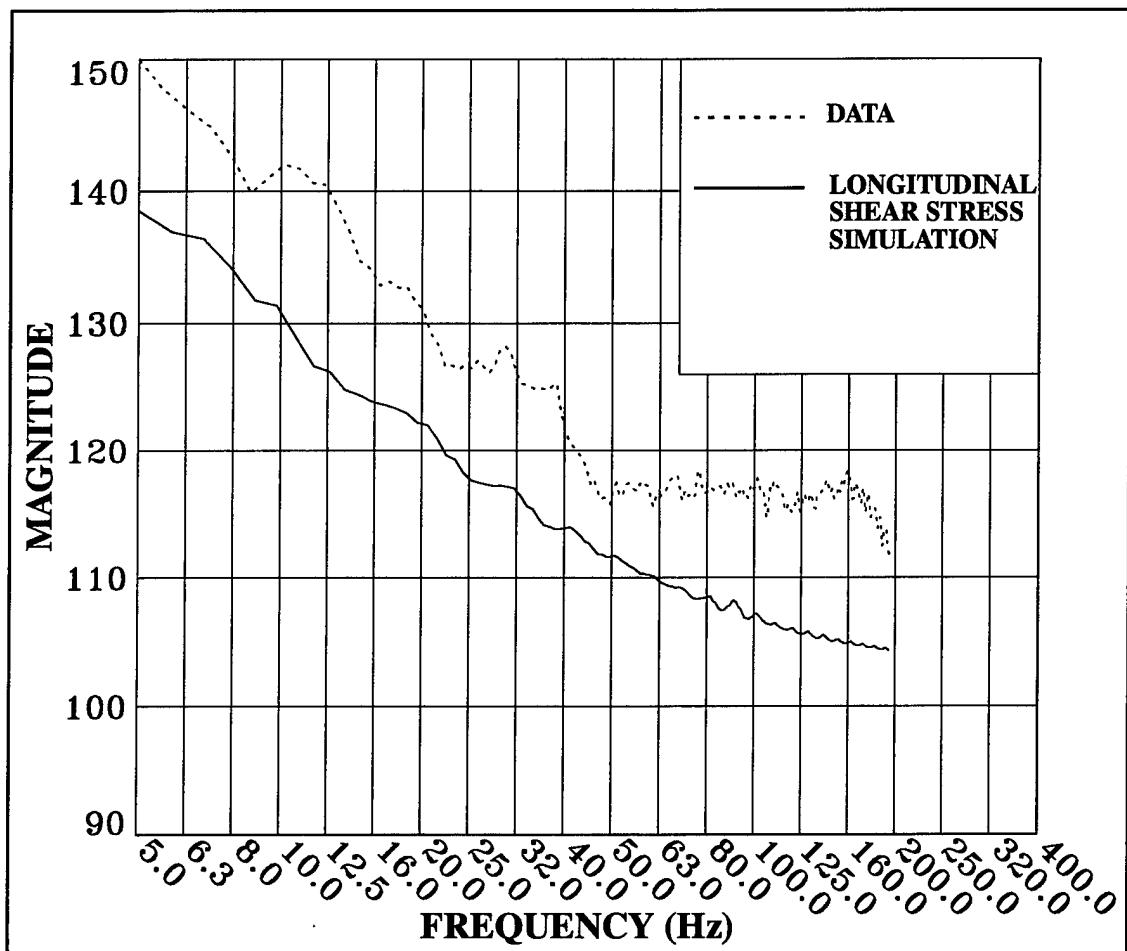


Figure 46. Convective Ridge Magnitude Comparison of Experimental Data and Wall Shear Stress Simulation at a Flow Speed of 10.11 m/sec
 (Magnitude = $10 \log(P_o(k, \omega)^2)$ re $\mu Pa^2/Hz/rad/m$)

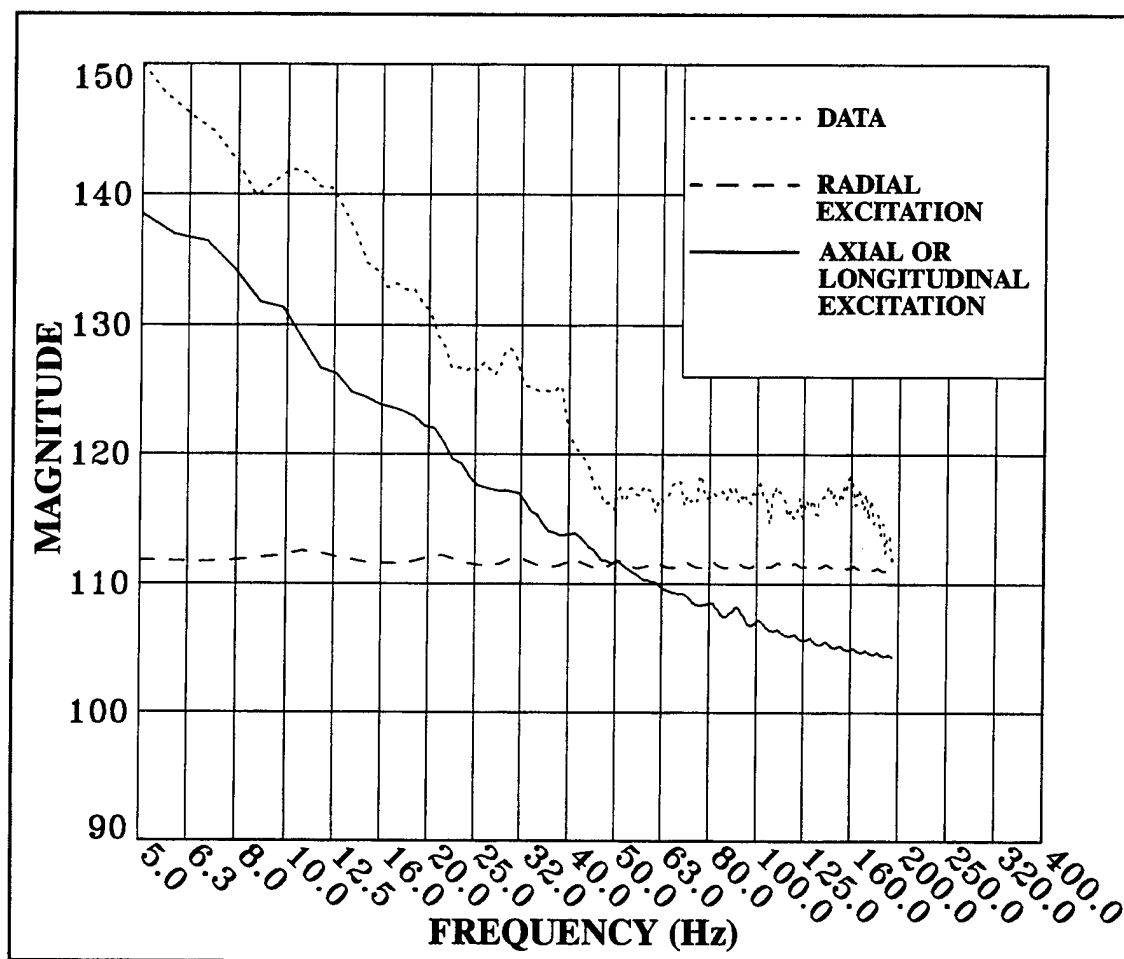


Figure 47. Convective Ridge Magnitude Comparison of Experimental Data with Wall Pressure and Wall Shear Stress Simulations at a Flow Speed of 10.11 m/sec (Magnitude = $10 \log(P_o(k, \omega)^2)$ re $\mu\text{Pa}^2/\text{Hz}/\text{rad}/\text{m}$)

10 Knots

Wall Pressure Excitation. A theoretical simulation for the ABC array response is performed for a 10-knot flow speed in the same manner as was described previously for 20 knots. The resulting image is displayed in figure 48 (upper image). Corresponding experimental data, for comparison with the simulation, is displayed as the lower image in the same figure.

The amplitude of the convective ridge from each of the images in figure 48 is compared in figure 49. Above 50 Hz, agreement is very close between the experiment and simulation for the wall pressure level, typically within 3 dB. Below 50 Hz, the comparison diverges, and the experimental data become dominated by nonwall-pressure sources, as was previously discussed.

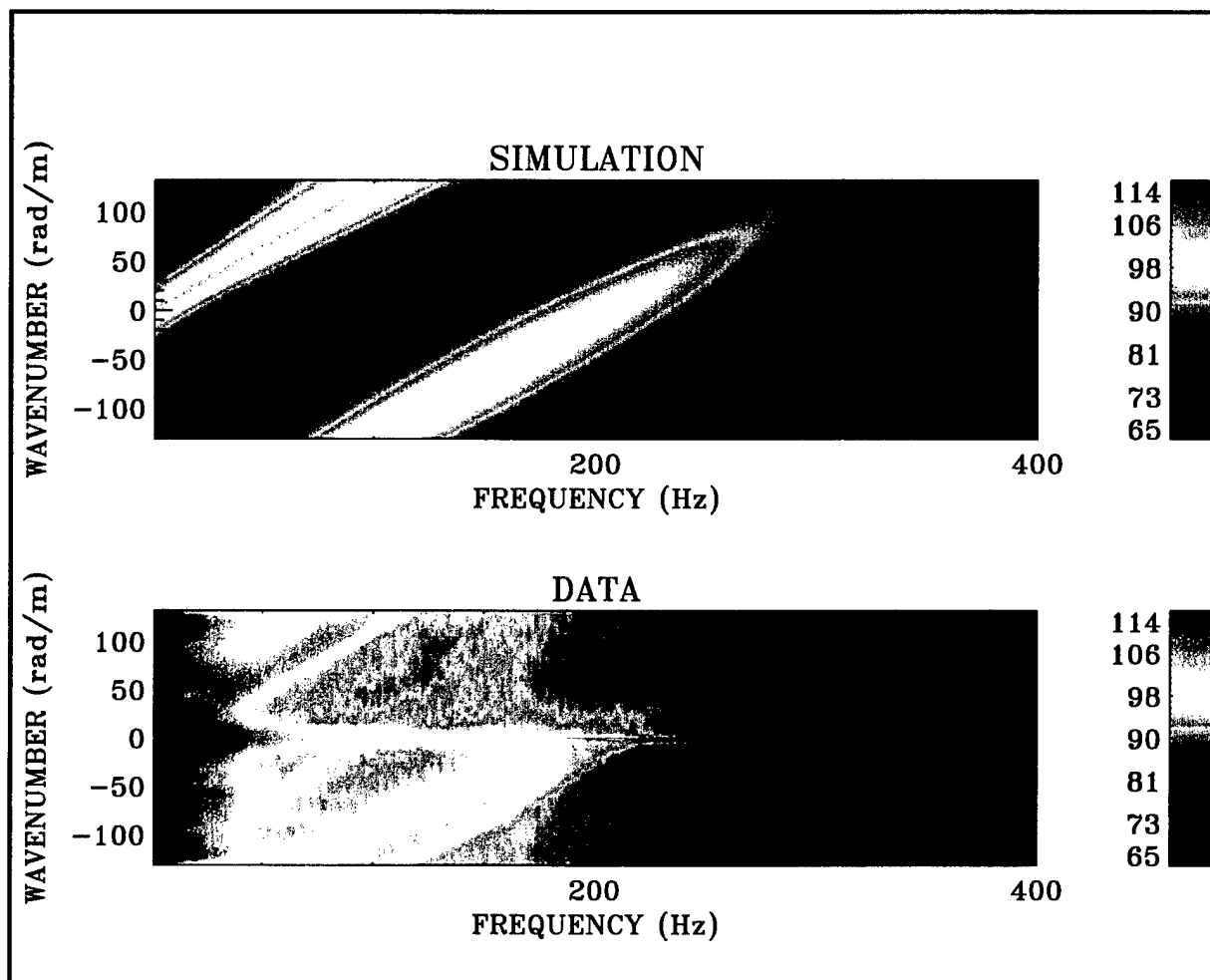


Figure 48. Comparison of Experimental Data $P_o(k, \omega)$ and Wall Pressure Simulation at a Flow Speed of 5.26 m/sec

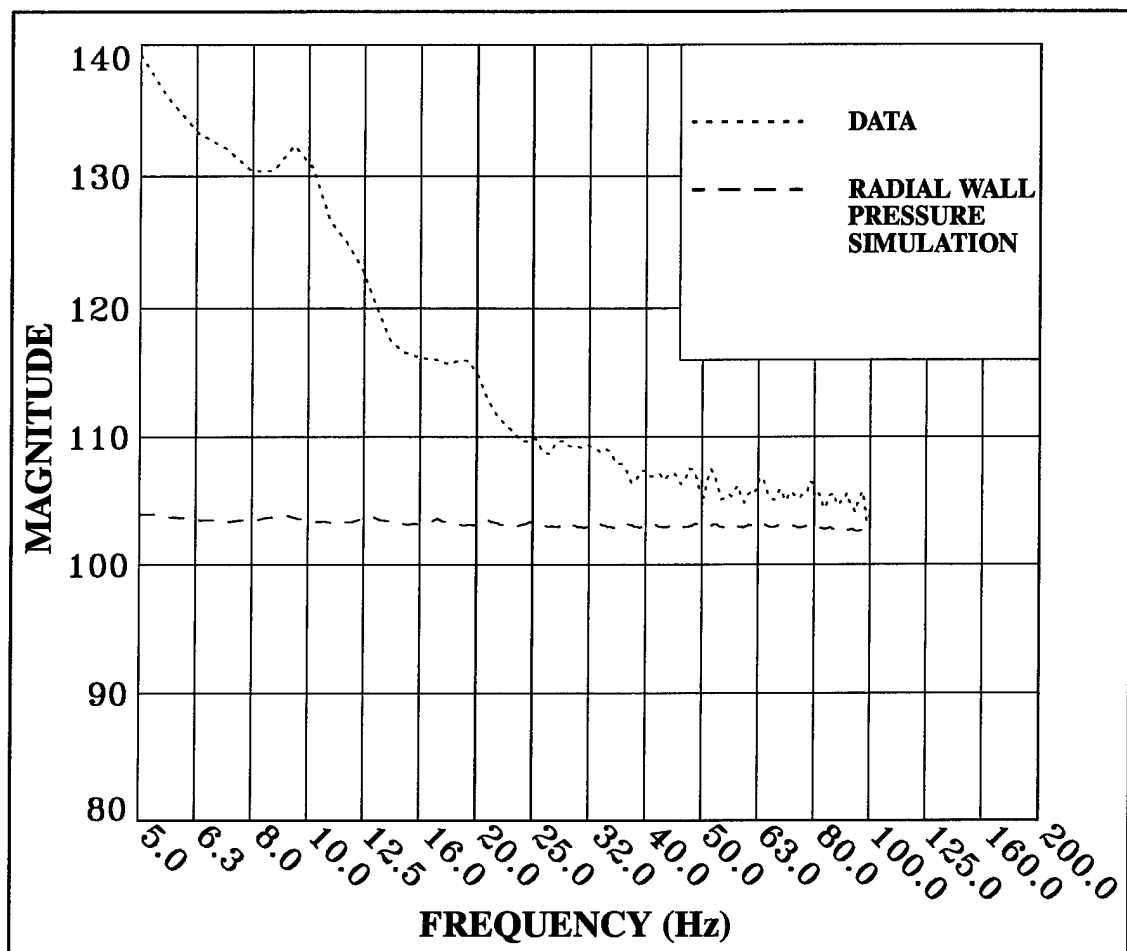


Figure 49. Convective Ridge Magnitude Comparison of Experimental Data and Wall Pressure Simulation at a Flow Speed of 5.26 m/sec
 (Magnitude = $10 \log(P_o(k, \omega)^2)$ re $\mu\text{Pa}^2/\text{Hz}/\text{rad}/\text{m}$)

Shear Stress Excitation. A theoretical simulation of the ABC array response to a longitudinal shear stress excitation is performed and displayed as the upper image in figure 50. The same experimental data file, used for comparison in figure 48, is displayed again as the lower image in figure 50.

An inspection of the images reveals the common extensional wave response at low wavenumbers, extending out to 400 Hz. The convective ridge is visible in the simulation, as well as in the experimental data. The level of the theoretical response of the convective ridge is lower than that of the experimental data, which is evident from an inspection of the images in figure 50, as well as from the amplitude comparison in figure 51. The wall pressure simulation is added to the amplitude comparison of figure 51, resulting in figure 52.

Careful inspection of figure 52 shows that the experimental data are just on the verge of departing from the slope of the wall pressure simulation above approximately 32 Hz. This situation indicates that the influence of the longitudinal shear excitation is almost as strong as the wall pressure component of the TBL at this flow speed. Care should thus be exercised when experimental data are used for wall pressure TBL model development at or below the 10-knot flow speed

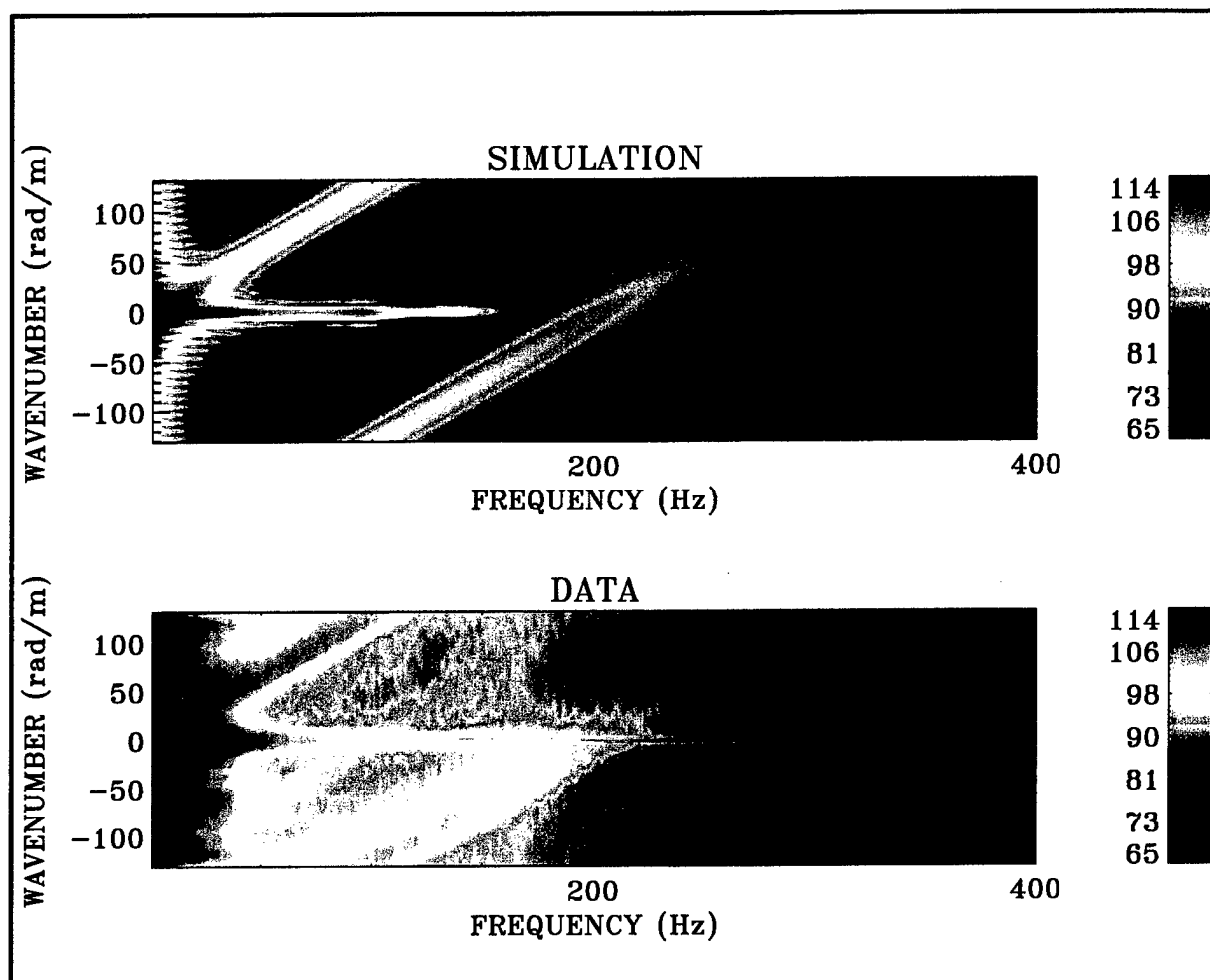


Figure 50. Comparison of Experimental Data $P_o(k,\omega)$ and Wall Shear Stress Simulation at a Flow Speed of 5.26 m/sec

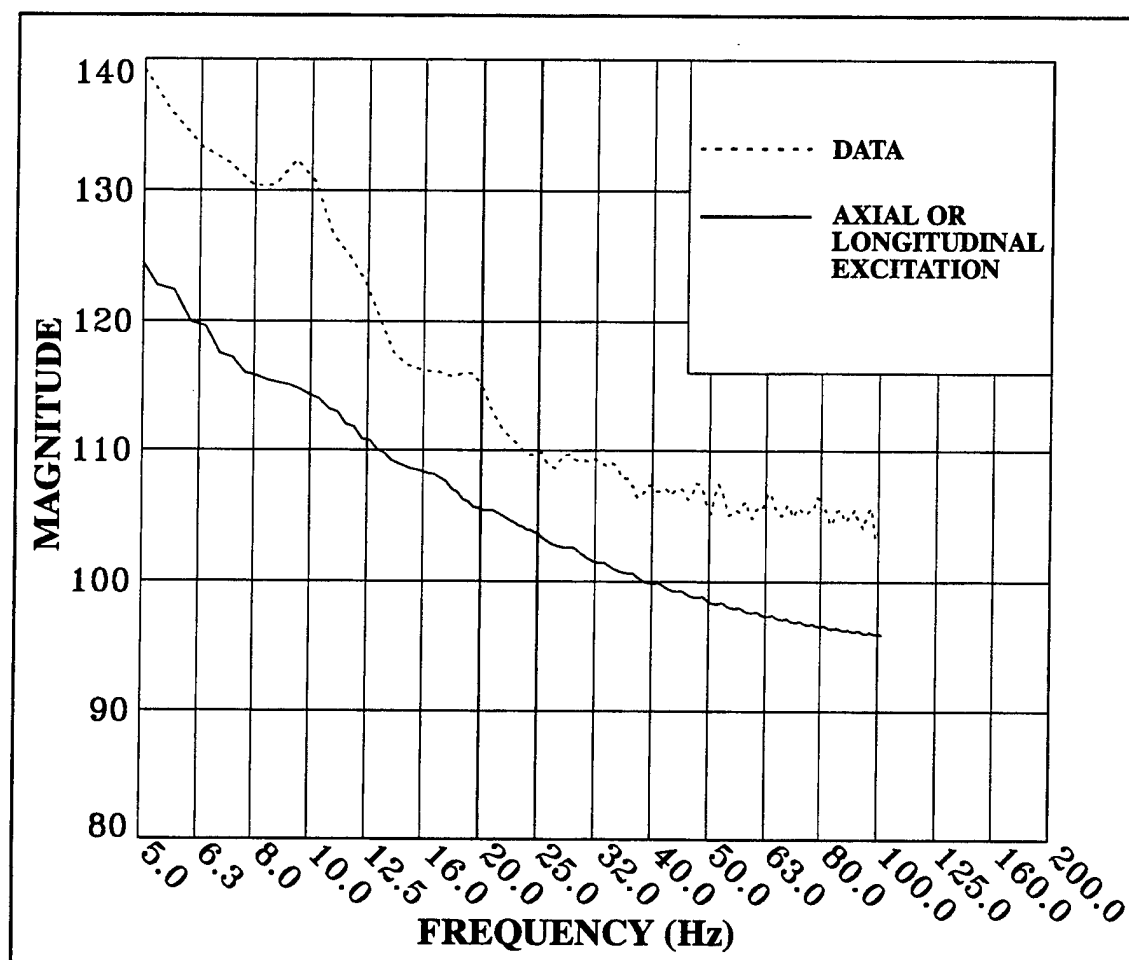


Figure 51. Convective Ridge Magnitude Comparison of Experimental Data and Wall Shear Stress Simulation at a Flow Speed of 5.26 m/sec
 (Magnitude = $10 \log(P_o(k, \omega)^2)$ re $\mu\text{Pa}^2/\text{Hz}/\text{rad}/\text{m}$)

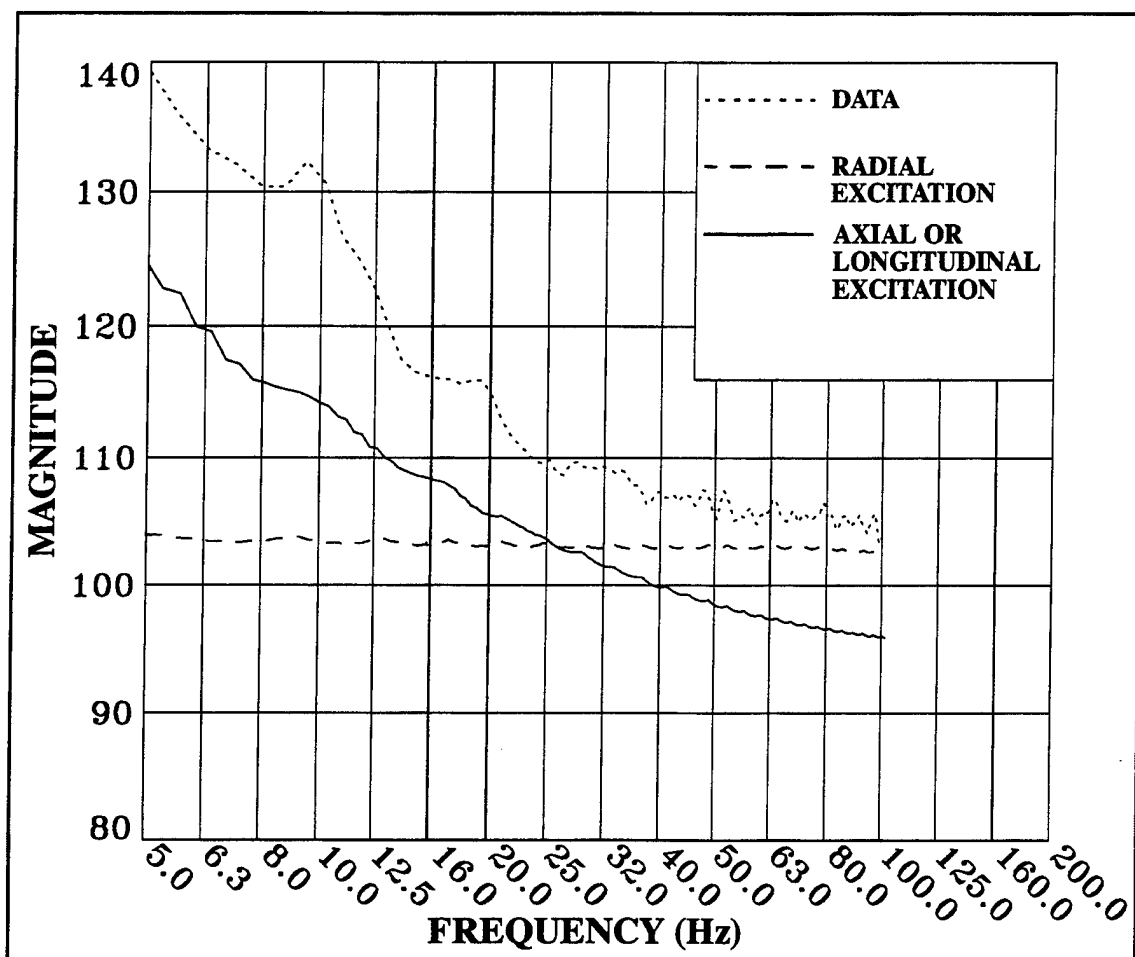


Figure 52. Convective Ridge Magnitude Comparison of Experimental Data with Wall Pressure and Wall Shear Stress Simulations at a Flow Speed of 5.26 m/sec (Magnitude = $10 \log(P_o(k, \omega)^2)$ re $\mu\text{Pa}^2/\text{Hz}/\text{rad}/\text{m}$)

5 Knots

Wall Pressure Excitation. Figure 53 contains the 5-knot experimental data, along with a theoretical simulation for this same flow speed. Comparison of convective ridge levels are plotted in figure 54. It is obvious that the character of the experimental data has departed from the simulation to a great degree. No longer does the convective ridge display the flat shape that it previously had, even down to the 10-knot flow speed.

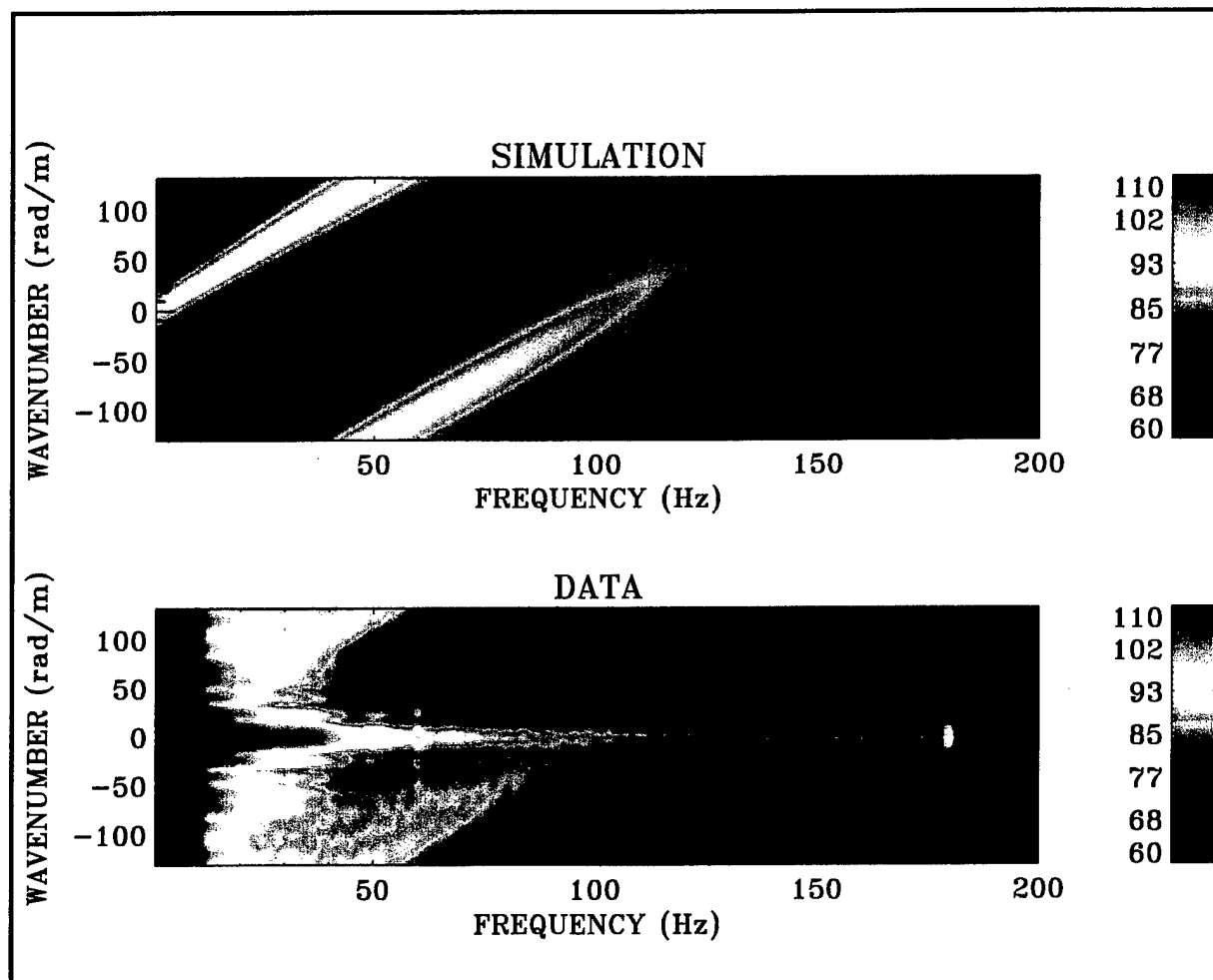


Figure 53. Comparison of Experimental Data $P_o(k, \omega)$ and Wall Pressure Simulation at a Flow Speed of 2.62 m/sec

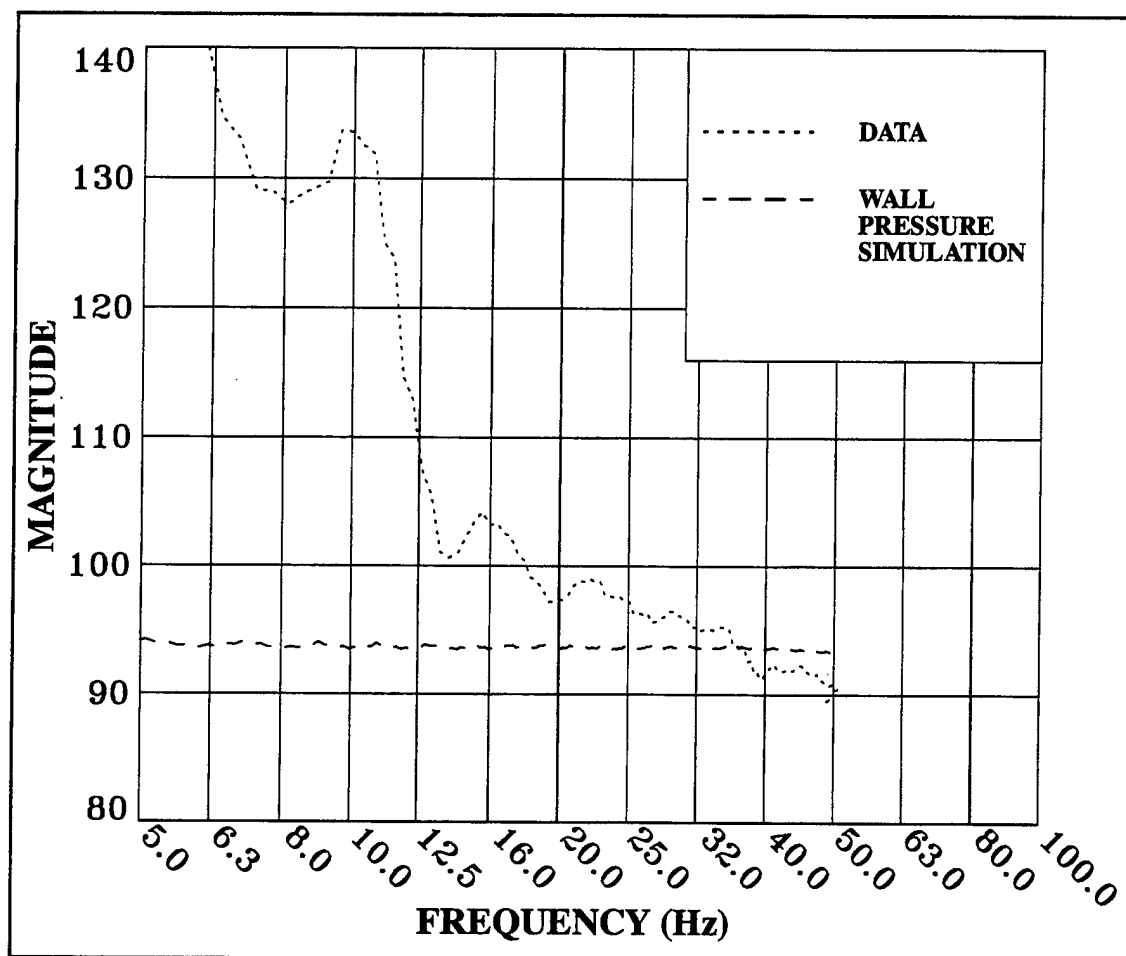


Figure 54. Convective Ridge Magnitude Comparison of Experimental Data and Wall Pressure Simulation at a Flow Speed of 2.62 m/sec
(Magnitude = $10 \log(P_o(k, \omega)^2)$ re $\mu Pa^2/Hz/rad/m$)

Shear Stress Excitation. The output of the ABC array at the 5-knot flow speed is completely dominated by excitation sources other than the wall pressure, with longitudinal shear excitation being the principal contributor. Comparison of the experimental data and the theoretical simulation for the longitudinal shear stress excitation is shown in figure 55. Figure 56 contains a comparison of convective ridge levels from the images of figure 55. In figure 57, the 5-knot wall pressure simulation is combined with the curves of figure 56. From approximately 13 Hz and higher, the experimental data track the longitudinal shear stress simulation, but do not track the wall pressure simulation at all.

The significant result of this study is that the current model for TBL wall pressure overpredicts the measured convective ridge levels at 5 knots by an undetermined amount. Additionally, the longitudinal shear stress component of the TBL exceeds the wall pressure component for the 5-knot flow speed by an undetermined amount. Caution must thus be exercised when drawing conclusions from these 5-knot experimental data.

The low-frequency sensor output is extremely high in level compared with the levels making up the convective ridge. Care must be taken not to mistake sidelobe leakage for a direct measurement of the convective ridge. Observation of figure 55 reveals that sidelobe leakage of low-wavenumber energy is contaminating the convective ridge up to approximately 20 Hz. Above 20 Hz, the convective ridge is relatively free from such leakage.

Additional information may be obtained from the experimental data by applying the full-field calibration to the shifted surface, as displayed in figures 18 through 20. This would allow accurate levels to be read from the convective ridge along the first alias. Further research in this area would double the useful frequency range that was obtained.

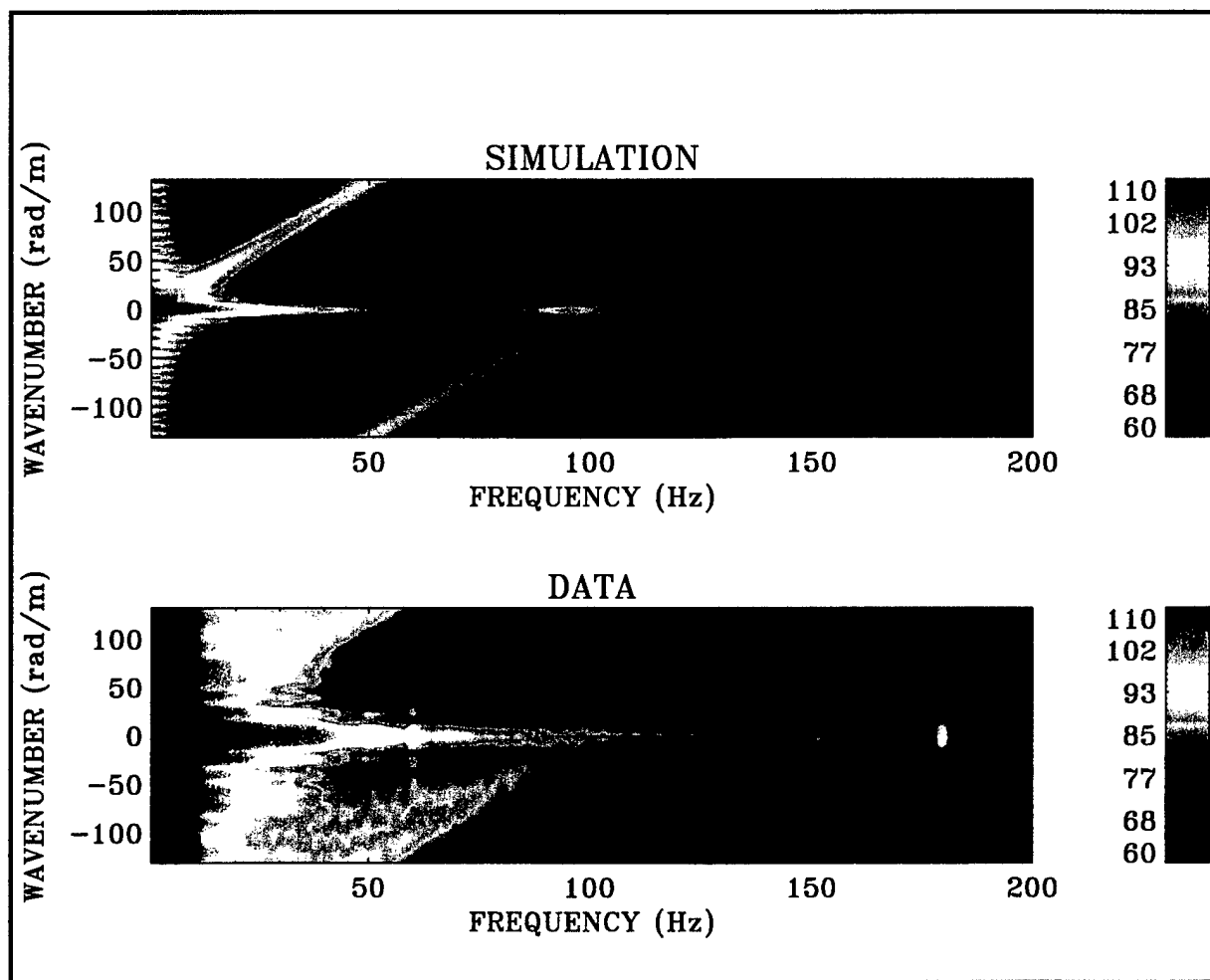


Figure 55. Comparison of Experimental Data $P_o(k, \omega)$ and Wall Shear Stress Simulation at a Flow Speed of 2.62 m/sec

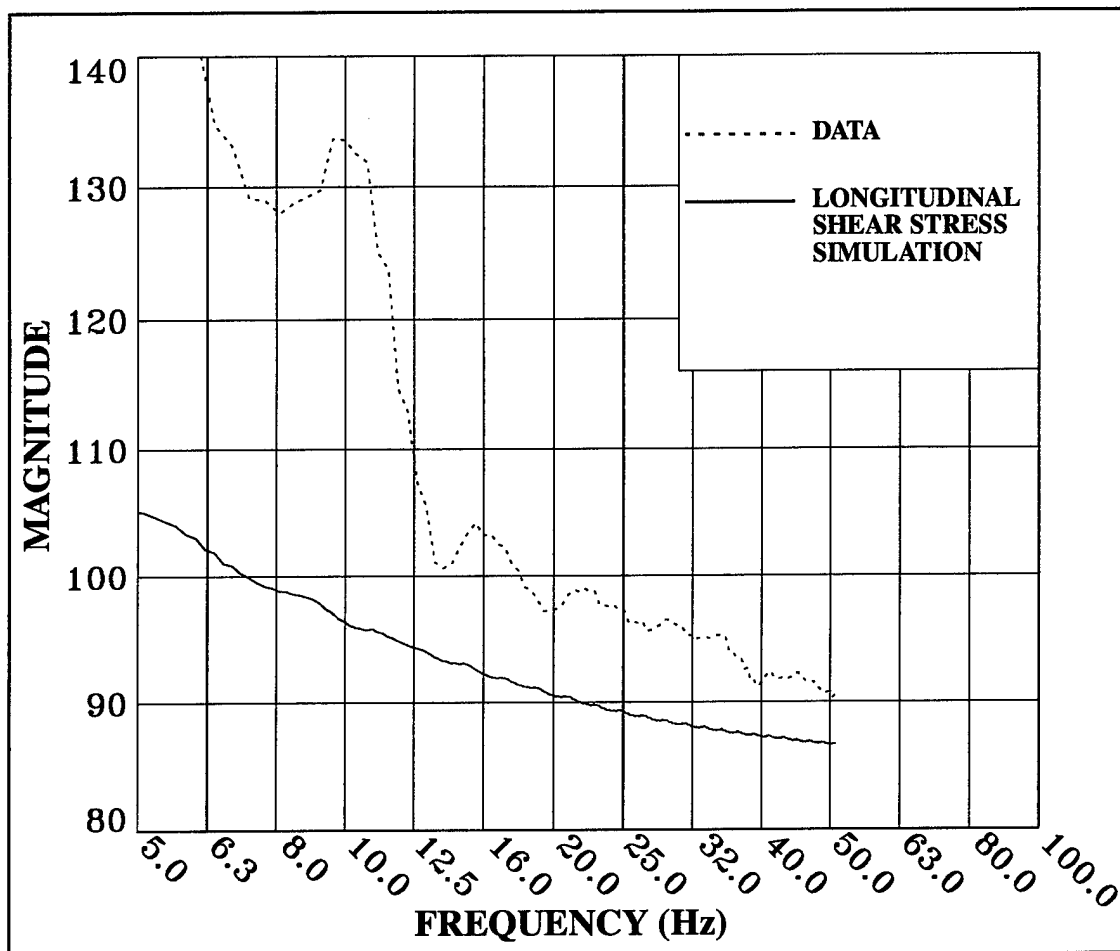


Figure 56. Convective Ridge Magnitude Comparison of Experimental Data and Wall Shear Stress Simulation at a Flow Speed of 2.62 m/sec
 (Magnitude = $10 \log(P_o(k, \omega)^2)$ re $\mu\text{Pa}^2/\text{Hz}/\text{rad}/\text{m}$)

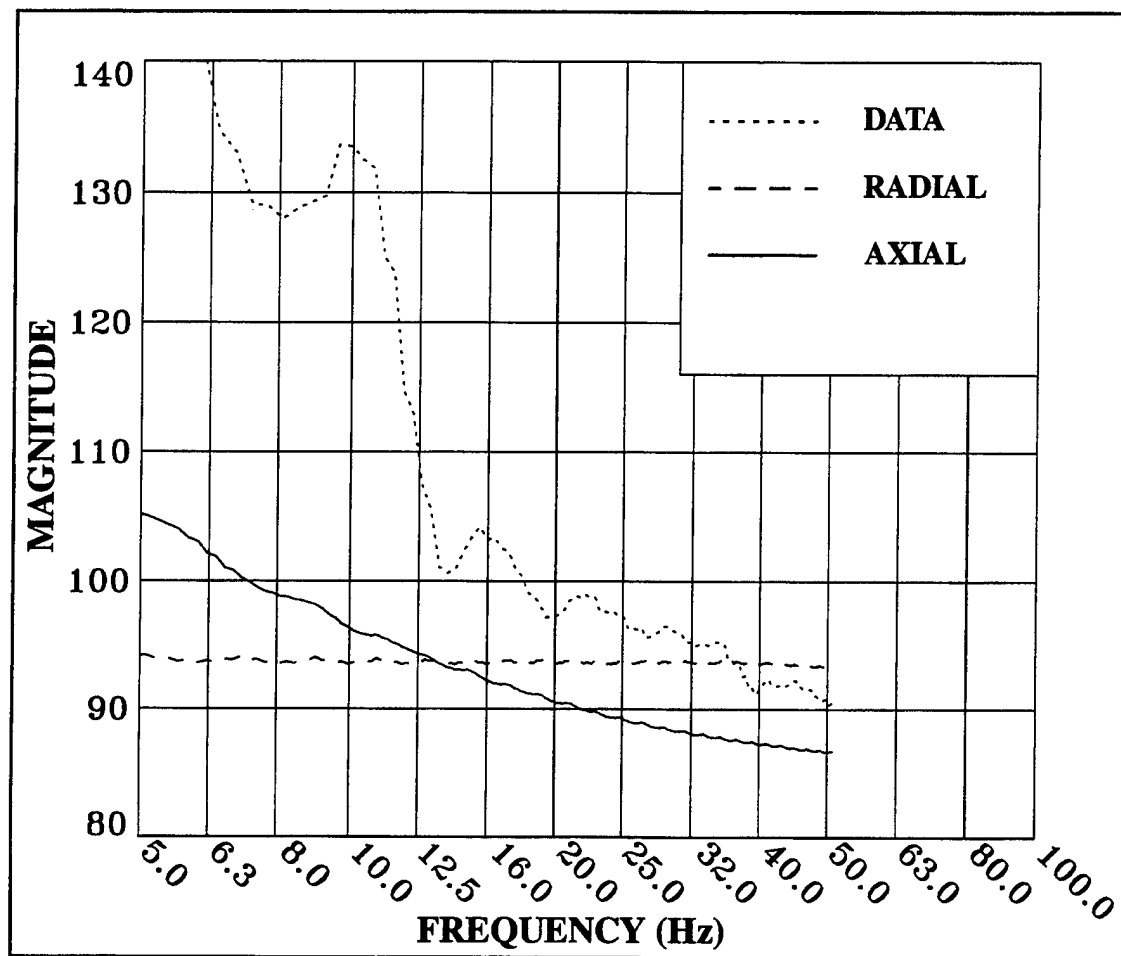


Figure 57. Convective Ridge Magnitude Comparison of Experimental Data with Wall Pressure and Wall Shear Stress Simulations at a Flow Speed of 2.62 m/sec (Magnitude = $10 \log(P_o(k, \omega)^2) \text{ re } \mu\text{Pa}^2/\text{Hz}/\text{rad}/\text{m}$)

COMPARISON OF EXPERIMENTAL DATA AND MODEL PREDICTIONS (OIL-FILLED CYLINDER)

In this section, experimental data from the OFC arrays are compared with theoretical model predictions. Equation (1) defines the theoretical calculation to be performed. A choice of models is available for the hose wall transfer function for wall pressure, $T^2(k, \omega)$. The hose wall transfer function calibration results, obtained earlier in this report, prompt a brief comparison of the two pertinent hose wall models (orthotropic bending shell and isotropic dynamic elasticity) before proceeding to the simulations performed with the bending shell model.

Equation (1) requires mathematical models for all its terms. The OFC transfer function for wall pressure will use equations (87) through (92) from reference 2, tailored for the specially orthotropic bending shell case and $n = 0$. Following this approach, a simulation of the beamformed surface of the high-wavenumber array is shown in the upper image of figure 58. The dynamic elasticity model (isotropic cylinder) uses equations (C-1) and (C-2), along with the necessary solution for the system matrix, equation (150), all from reference 3. The beamformed surface using the elasticity model is displayed in the lower image of figure 58.

Unlike the transfer function for the ABC, the transfer function for the OFC does not require normalization to low wavenumber and frequency. In this case,

$$T(k, \omega) = T_{OFC}(k, \omega) = \frac{P_i}{P_o}(k, \omega, r) , \quad (29)$$

which is dimensionless, directly provides the ratio of inner to outer pressure needed for the self-noise calculation in equation (1).

Comparison of both models in figure 58 at 246 Hz is displayed in figure 59. The bending shell model has a steeper rolloff in wavenumber, attenuating the pressure field more than the elasticity model. A beam cut made at -215 m/sec for the two images of figure 58 is displayed in figure 60. The elasticity model predicts several decibels of increase in pressure, at low wavenumber, due to the retention of radial changes through the cross section of the

cylinder. The magnitude of the elasticity model's transfer function at $k = 0$ is actually slightly greater than 1 (see reference 3, figure 52).

In the earlier discussion of hose wall calibration, it was found that the bending shell model more closely approximates the experimental measurements at higher frequency. While an elasticity model, in general, preserves more of the true physics of the cylinder, its isotropic formulation neglects an important aspect of cylinder construction, which is the longitudinal reinforcement. Therefore, in this case, the bending shell model is the better compromise between the two choices for the medium- to high-wavenumber region and will be used for comparison against experimental data in the remainder of the report. In the low-wavenumber ($k = 0$) region, the simulations should be performed with the elasticity model to engage the true behavior of the thick-wall cylinder, which increases the pressure by several decibels.

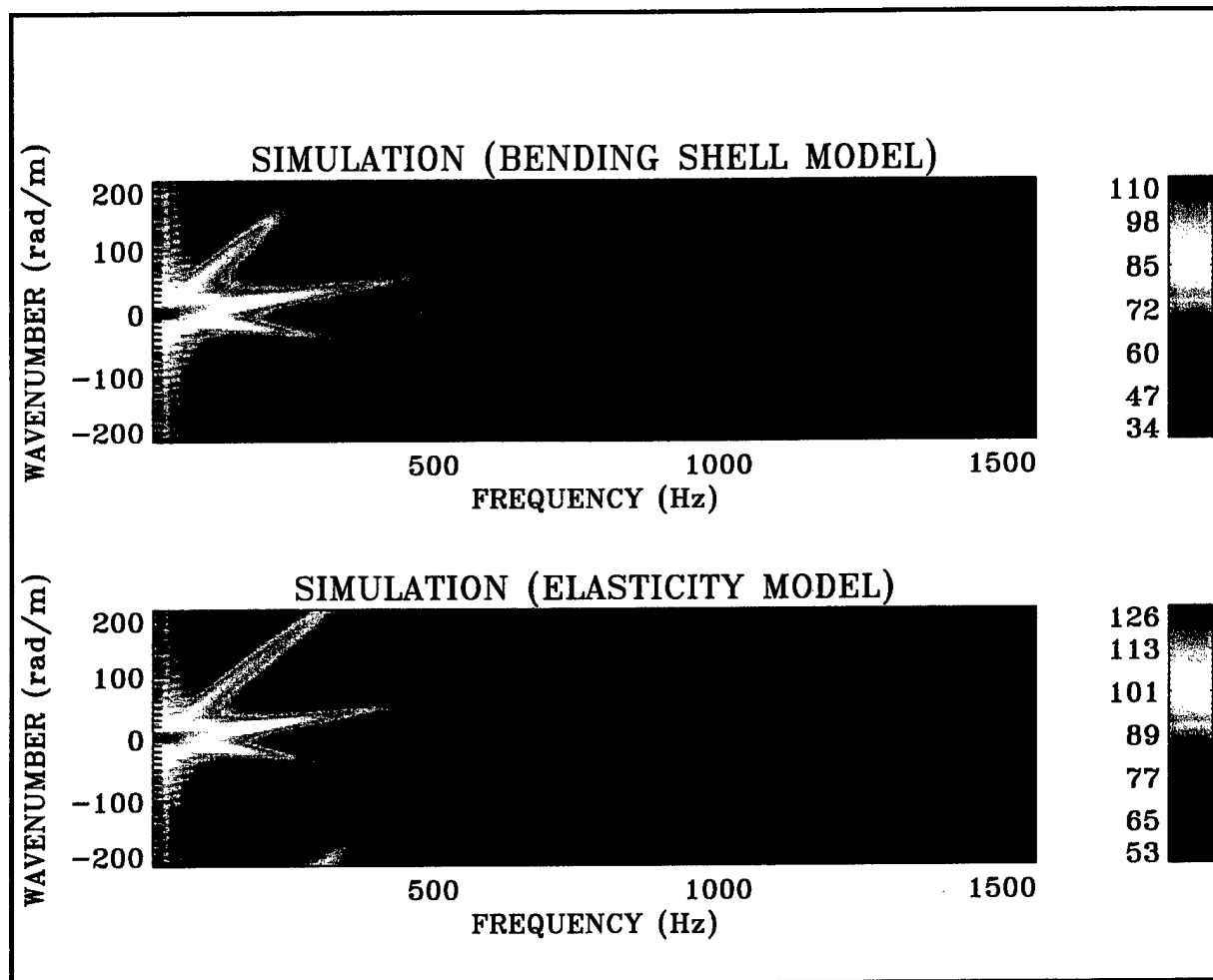


Figure 58. High- k Array Beamformed Surface Simulation of the Inner Pressure $P_i(k, \omega)$ Using the Bending Shell and Elasticity Models at a Flow Speed of 8.9 m/sec

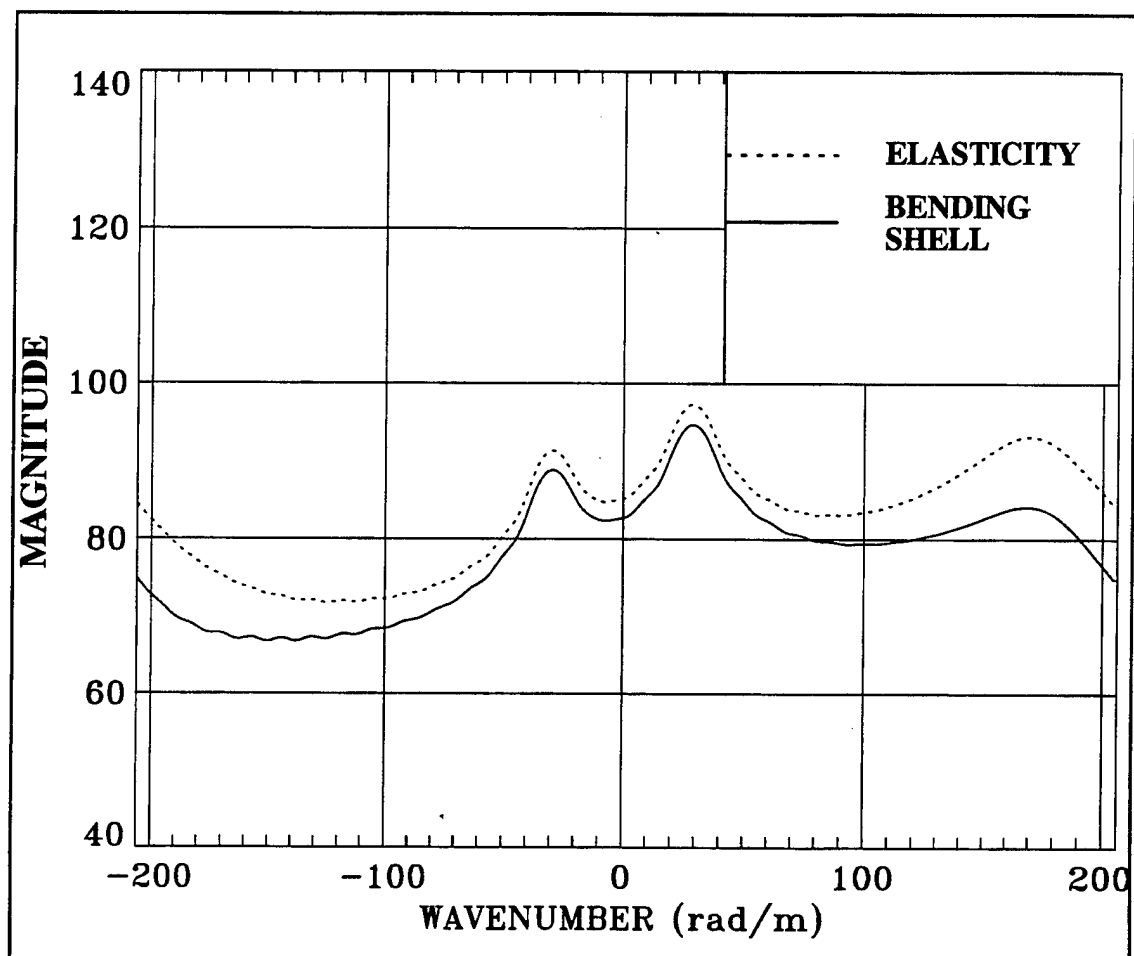


Figure 59. Comparison of the Elasticity and Bending Shell Models from Figure 58 at 246 Hz (Magnitude = $10 \log(P_f(k, \omega)^2)$ re $\mu\text{Pa}^2/\text{Hz}/\text{rad}/\text{m}$)

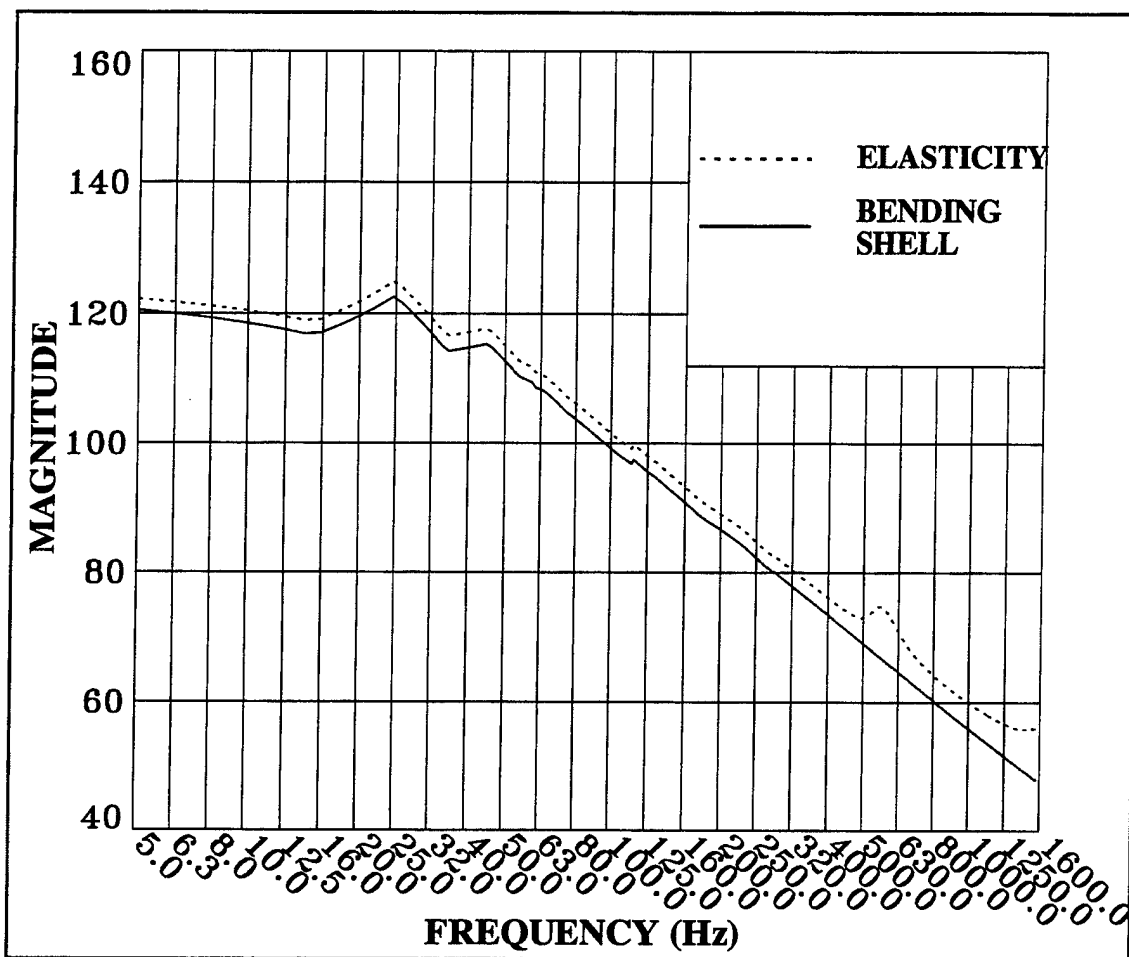


Figure 60. Comparison of the Elasticity and Bending Shell Models from Figure 58 at -215 m/sec (Magnitude = $10 \log(P_f(k, \omega)^2)$ re $\mu Pa^2/Hz/rad/m$)

20-Knot Freestream Velocity

Wall Pressure Excitation. Figures 61 through 63 compare the high-wavenumber array with a theoretical prediction for the 20-knot (10.3-m/sec) freestream flow speed. In figure 61, where the simulation is shown as the upper image and the experimental data as the lower image, a general similarity is observed between the prediction and the measurement. In this figure, the breathing wave is seen to exist as an organized structure well above 1000 Hz, and the convective ridge is of comparable amplitude. The simulation was performed, as in the ABC case, with uniform array shading, which results in the first sidelobe being 16 dB below the mainlobe and the rest of the sidelobes rolling off at 6 dB per octave.

The experimental data exhibit sidelobe leakage that produces stripes of energy parallel to the convective ridge that are higher in level than those predicted by use of a spatial Hanning window. This is somewhat enigmatic since the array shading should produce first sidelobe levels 28 dB below the mainlobe (28 dB was actually achieved in the suppression of the low-frequency $k = 0$ response that leaks across wavenumber). The phase and amplitude were uniform during the original frequency calibration. At this point, there is no clear explanation for what appears to be convective ridge sidelobe leakage.

Even during the second calibration in the anechoic chamber (August 1997), the amplitude variation was very small (± 1.0 dB). The phase variation between channels was also insignificant; most of the channels overlaid each other, achieving ± 2.0 degrees of phase variation, with the greatest variation reaching ± 4.0 degrees. The highest amplitude component of the pressure spectra filtered by the hose wall is the breathing wave; the convective ridge is actually lower in level. Thus, if any component of the pressure spectra is going to cause sidelobe leakage, it most logically would be the breathing wave. Several channels had obviously been damaged since the time of the original experiments (April 1994), which could also explain the sidelobe leakage observed in the measurement.

Cuts through the images of figure 61 have been made at 204 Hz and overplotted in figure 62. The same forcing function for the TBL wall pressure in the ABC simulation is used here for the OFC simulation. As seen earlier in the case of the ABC experimental data, the convective

ridge for the OFC data displays an asymmetry with respect to wavenumber. These high- k wavenumber-filter data thus confirm the asymmetric convective ridge observed earlier in the ABC data measured on the surface of the array. The asymmetric OFC experimental data depart from the simulation on the low-wavenumber edge of the convective ridge (figure 62).

The downstream breathing wave peak in the prediction is aligned perfectly, in both amplitude and speed, with the peak in the experimental data. This result illustrates the strong agreement between theory and experiment in this region.

Figure 63 compares convective ridge levels from the simulation and experimental data shown in figure 61. The curve seems to divide into three regions. As was previously discussed, the first region, below 16 Hz, is dominated by longitudinal vibration, not by TBL wall pressure. The second region, between 16 and 160 Hz, is marked by close agreement in the range of 0 to 10 dB. The third region, 160 to 275 Hz, shows close agreement between 0 and 3 dB, which is remarkable, considering the complexity of the problem. If the magnitude of the wall pressure is adjusted up, as the ABC data suggest (figure 44), overall agreement will be improved for this case.

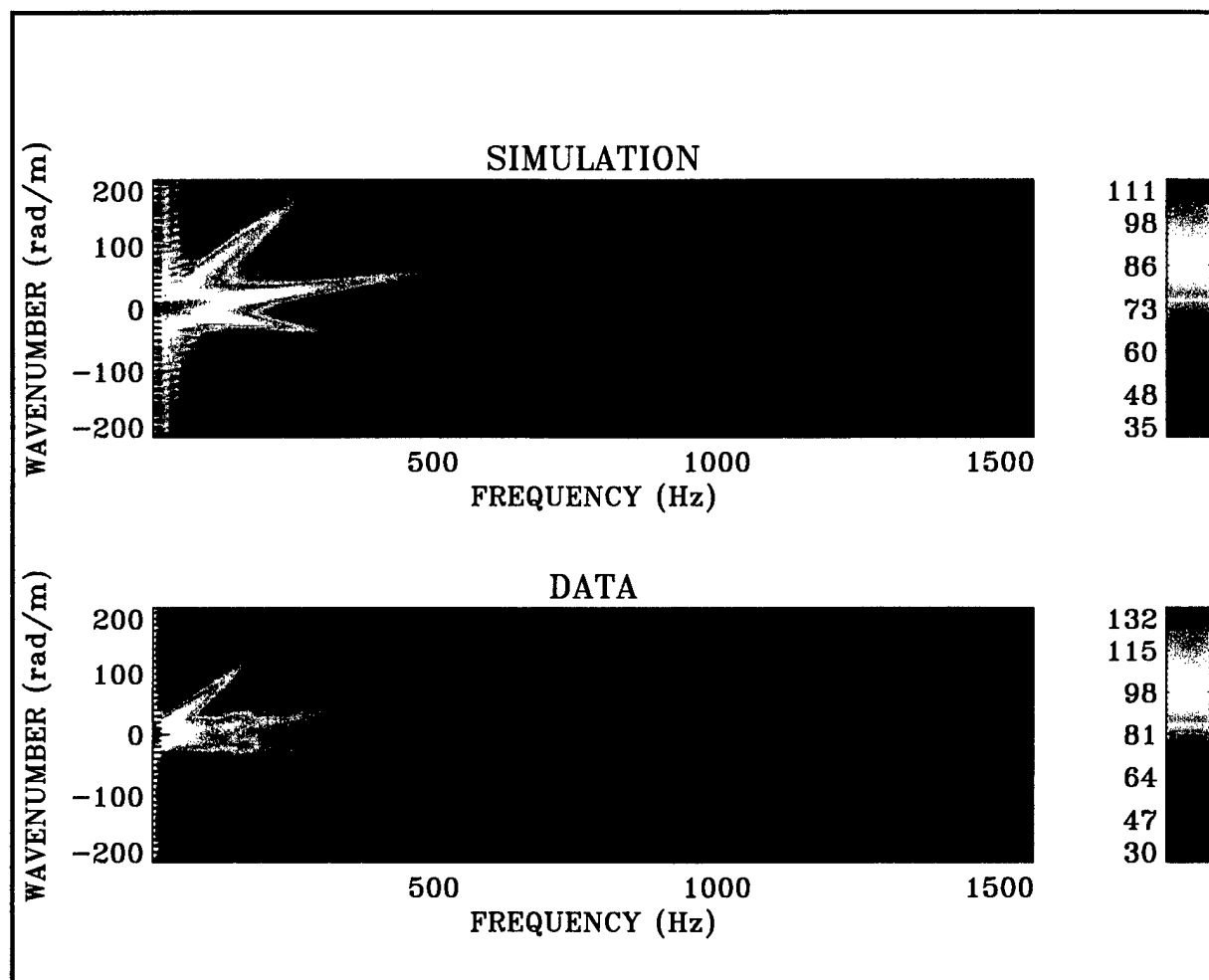


Figure 61. Comparison of Experimental Data $P_i(k, \omega)$ and Model Simulation Using a Wall Pressure Excitation at a Flow Speed of 10.3 m/sec

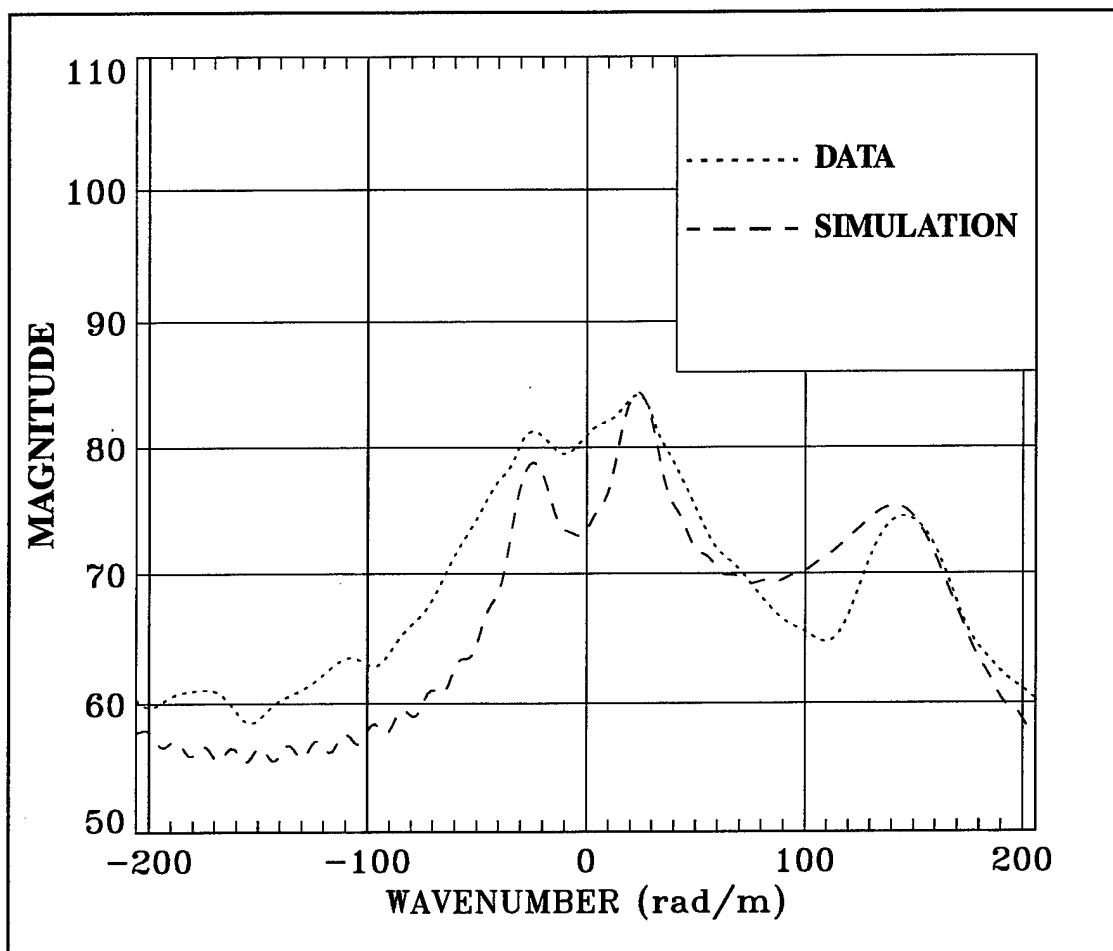


Figure 62. Comparison of Levels in Figure 61 at 204 Hz and a Flow Speed of 10.3 m/sec
(Magnitude = $10 \log(P_f(k, \omega)^2)$ re $\mu\text{Pa}^2/\text{Hz}/\text{rad/m}$)

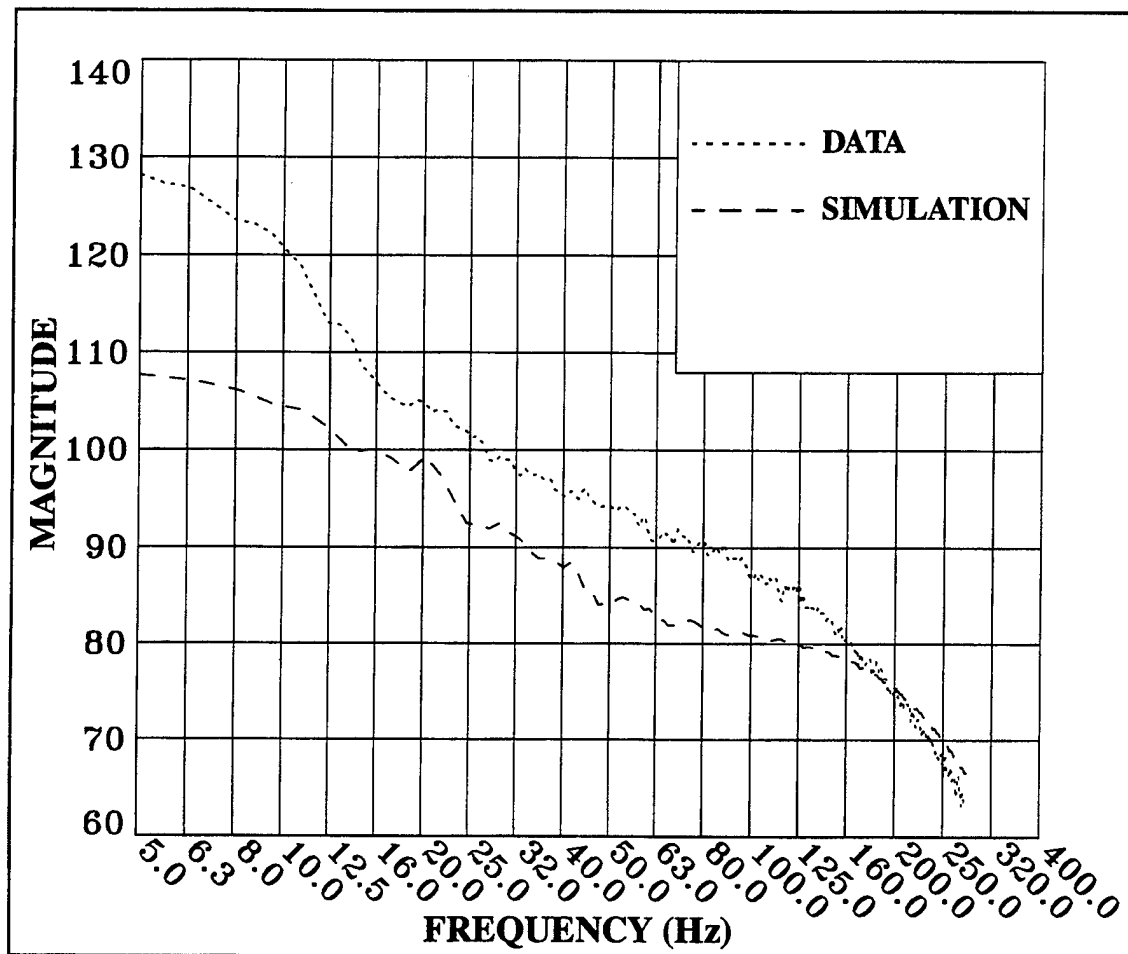


Figure 63. Convective Ridge Magnitude Comparison of Experimental Data and Bending Shell Model Simulation from Figure 61 at a Convective Velocity of 9.5 m/sec (Magnitude = $10 \log(P_i(k, \omega)^2)$ re $\mu\text{Pa}^2/\text{Hz}/\text{rad}/\text{m}$)

Shear Stress Excitation. In this section, simulations for the high- k wavenumber-filter response to longitudinal shear stress excitation have been performed and compared with the same experimental data used for the wall pressure comparison. The simulations are performed with the current semiempirical model for wall shear stress, the magnitude of which is approximately 18 dB lower than the wall pressure surface shown in figure 2. The OFC response to the longitudinal shear stress, T_x^2 , is given by equations (89), (90), (91), and (93) from reference 2. The calculation results in the upper image shown in figure 64.

Cuts are made through the images of figure 64 at 204 Hz and displayed in figure 65. Cuts at the convective velocity of 9.5 m/sec are made from the images in figure 64 and displayed in figure 66. From these comparisons, it is clear that the predicted magnitude of the pressure spectra developed by the longitudinal shear stress excitation is well below that of the measured data in the region of the convective ridge. The contribution to the measured pressure spectra by the longitudinal shear stress is therefore negligible (30 to 40 dB down from the wall pressure contribution) and can be safely ignored. The dominant feature in the response surface is the extensional wave, evident in the simulation at low wavenumber.

In figure 64, the extensional wave appears resonant, with high-amplitude spots showing up and leaking across wavenumber. This is an undersampling limitation due to the sparseness of the evaluation in wavenumber and frequency that is applied to the theoretical solution for the beamformed surface. The theoretical solution is evaluated at finite intervals of wavenumber and frequency, which misses the sharply resonant extensional wave response most of the time and finds the resonant peak only four times, as seen in figure 64. In reality, the extensional wave amplitude should not be resonant in frequency along the 775-m/sec propagation direction as figure 67 indicates; it should be at a uniform, but declining, level.

The uniform array shading that has been applied to the theoretical prediction allows energy to leak across wavenumber in figure 64 because the simulation is based on only the longitudinal shear stress component. The actual experimental data from the sensor are the sum of both the wall pressure and longitudinal shear stress excitations; therefore, the leaking is not observed. The experimental data have been processed with a Hanning window, which has first sidelobes that

are theoretically 32 dB below the mainlobe response. This window is sufficient to suppress most leakage that is likely to occur in the pressure spectra within an OFC.

The interesting feature in figure 67 is that the theoretical peak values of the extensional wave are equivalent to the measured data. The most likely explanation then, for the energy at $k = 0$ in figure 64, is a longitudinal shear-excited extensional wave response.

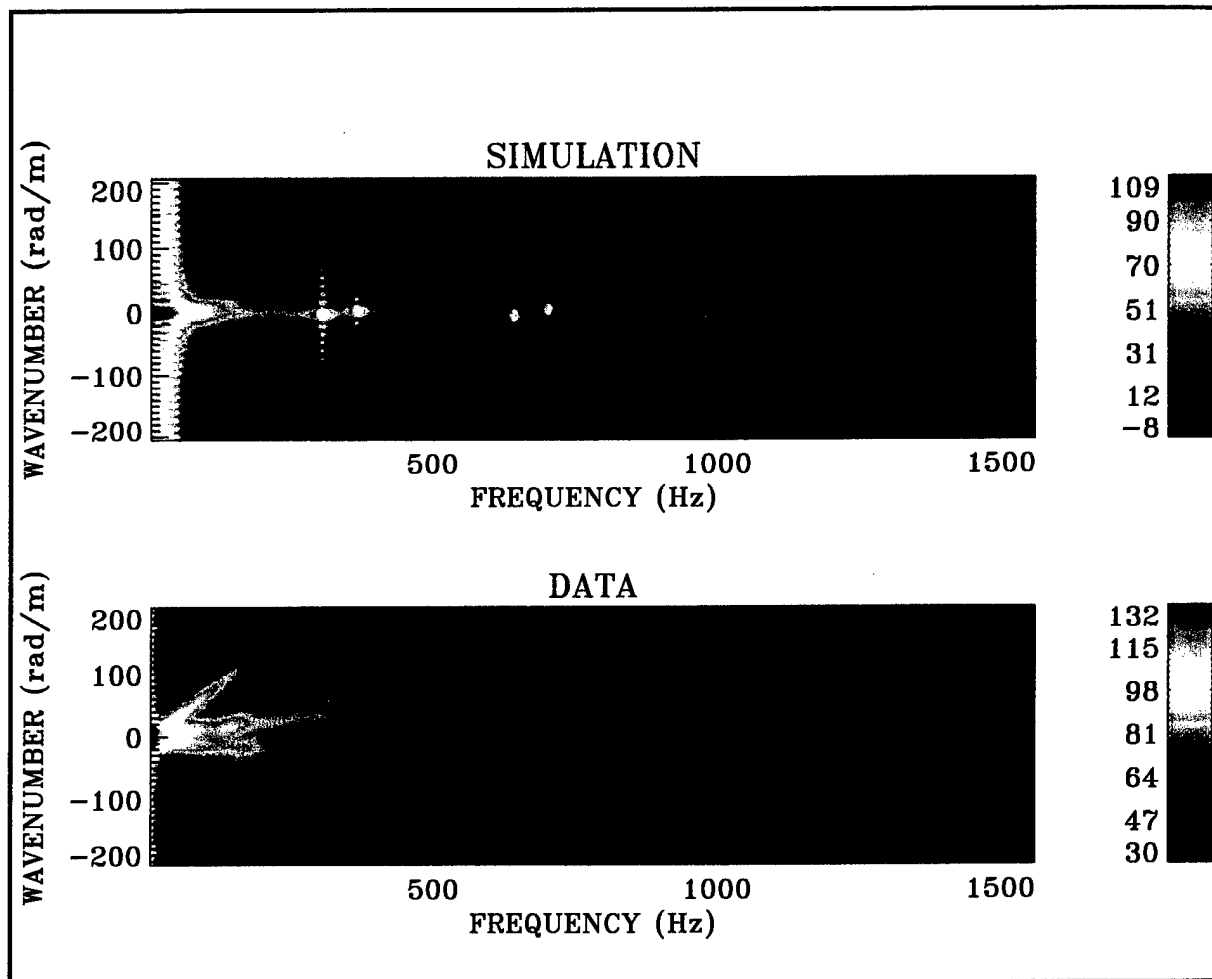


Figure 64. Comparison of Experimental Data $P_i(k, \omega)$ and Model Simulation Using a Longitudinal Shear Stress Excitation at a Flow Speed of 10.3 m/sec

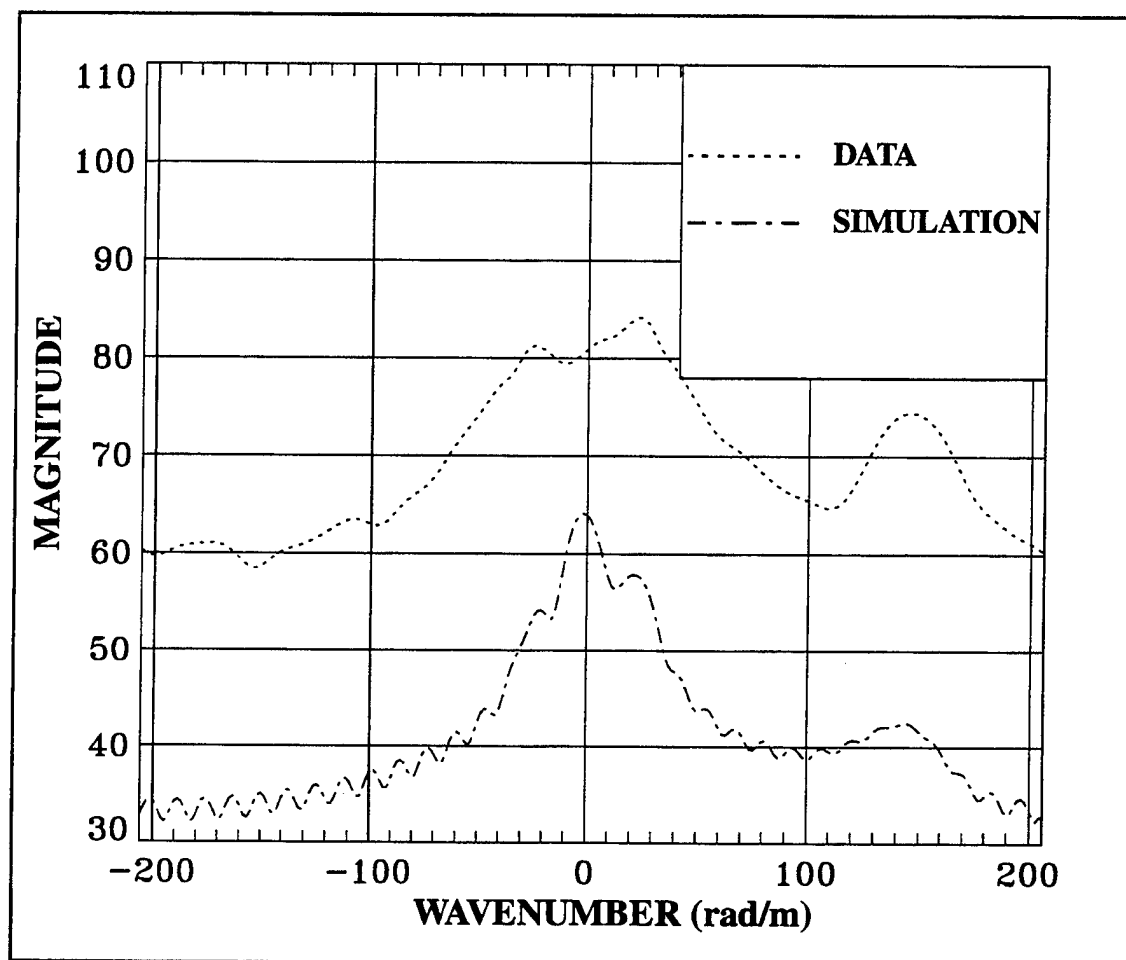


Figure 65. Comparison of Levels in Figure 64 at 204 Hz and a Flow Speed of 10.3 m/sec
 (Magnitude = $10 \log(P_f(k, \omega)^2)$ re $\mu\text{Pa}^2/\text{Hz}/\text{rad}/\text{m}$)

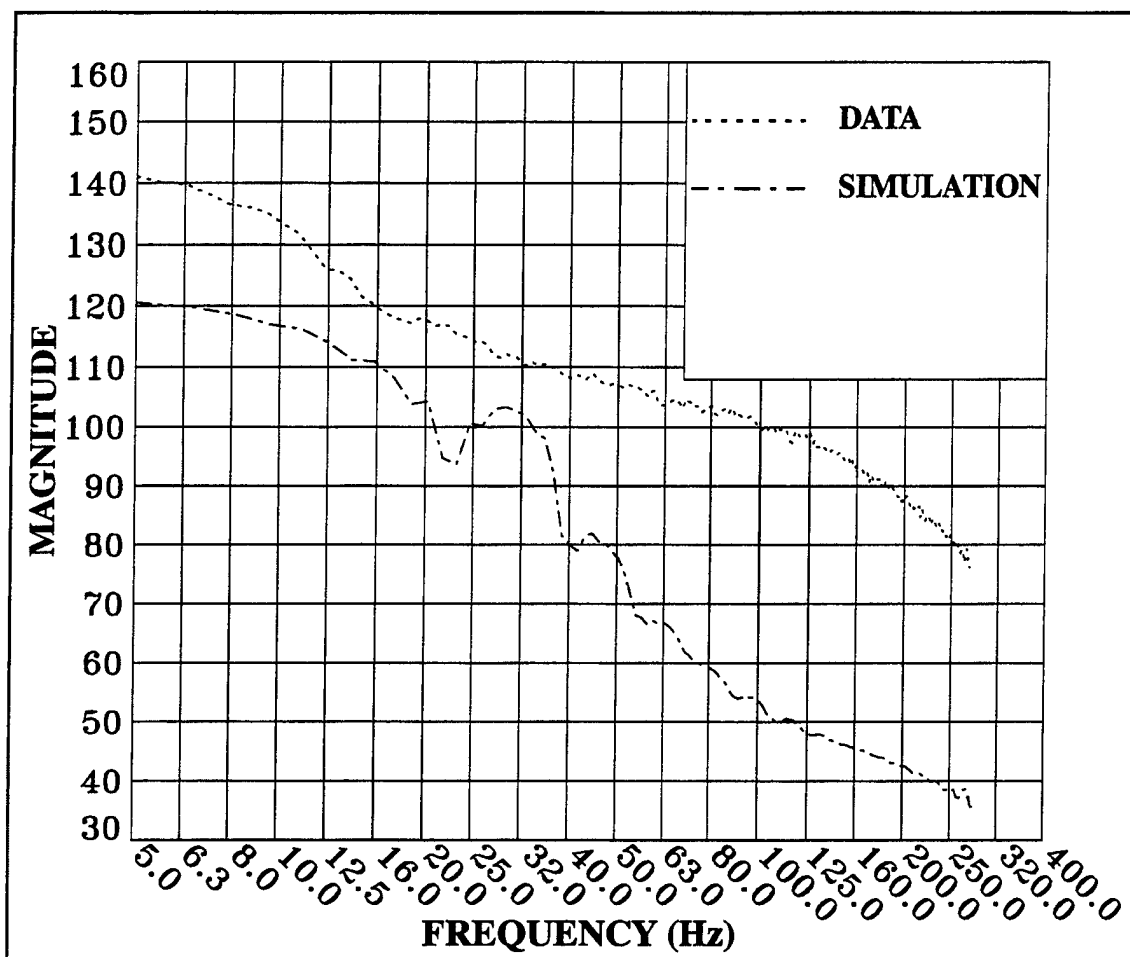


Figure 66. Convective Ridge Magnitude Comparison of Experimental Data and Bending Shell Model Simulation from Figure 64 at a Convective Velocity of 9.5 m/sec (Magnitude = $10 \log(P_i(k, \omega)^2)$ re $\mu\text{Pa}^2/\text{Hz}/\text{rad}/\text{m}$)

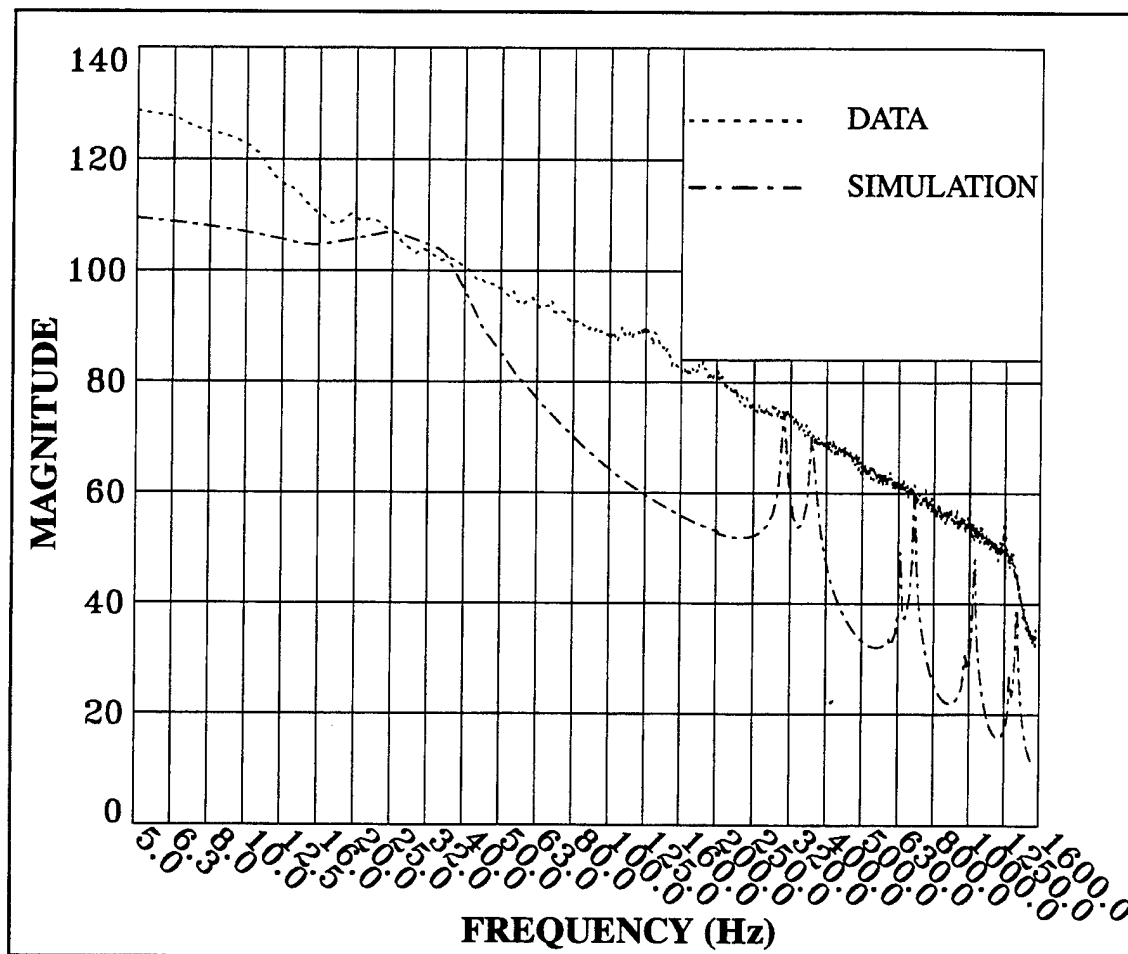


Figure 67. Extensional Wave Magnitude Comparison of Experimental Data and Bending Shell Model Simulation from Figure 64 with a Beam Cut at 775 m/sec (Magnitude = $10 \log(P_i(k, \omega)^2)$ re $\mu\text{Pa}^2/\text{Hz}/\text{rad}/\text{m}$)

10-Knot Freestream Velocity

Wall Pressure Excitation. Theoretical simulation of the high- k wavenumber-filter array response for a wall pressure excitation with a 10-knot flow speed is computed and displayed as the upper image of figure 68. The corresponding experimental data file is displayed as the lower image of the same figure.

There is acoustic energy visible at low-wavenumber $k = 0$. It is possible to differentiate acoustic energy from a smooth longitudinal shear-driven TBL response by the tonal quality of the energy. Three cuts through the images of figure 68 at 84, 345, and 445 Hz are displayed in figures 69, 70, and 71, respectively. In general, these frequency cuts show very good agreement between prediction and experiment for the amplitude of the breathing wave peaks and the subsequent rolloff to higher wavenumber.

The low-wavenumber level is underpredicted by several decibels, as was pointed out earlier; therefore, the agreement between prediction and experiment is actually better than what would be inferred from the figures. Figure 72 contains a comparison of the magnitude of the convective ridge at a velocity of 4.5 m/sec for the images of figure 68. There is an agreement of 0 to 8 dB above 20 Hz. Below 20 Hz, the array output is probably influenced by vibration, and the agreement decreases.

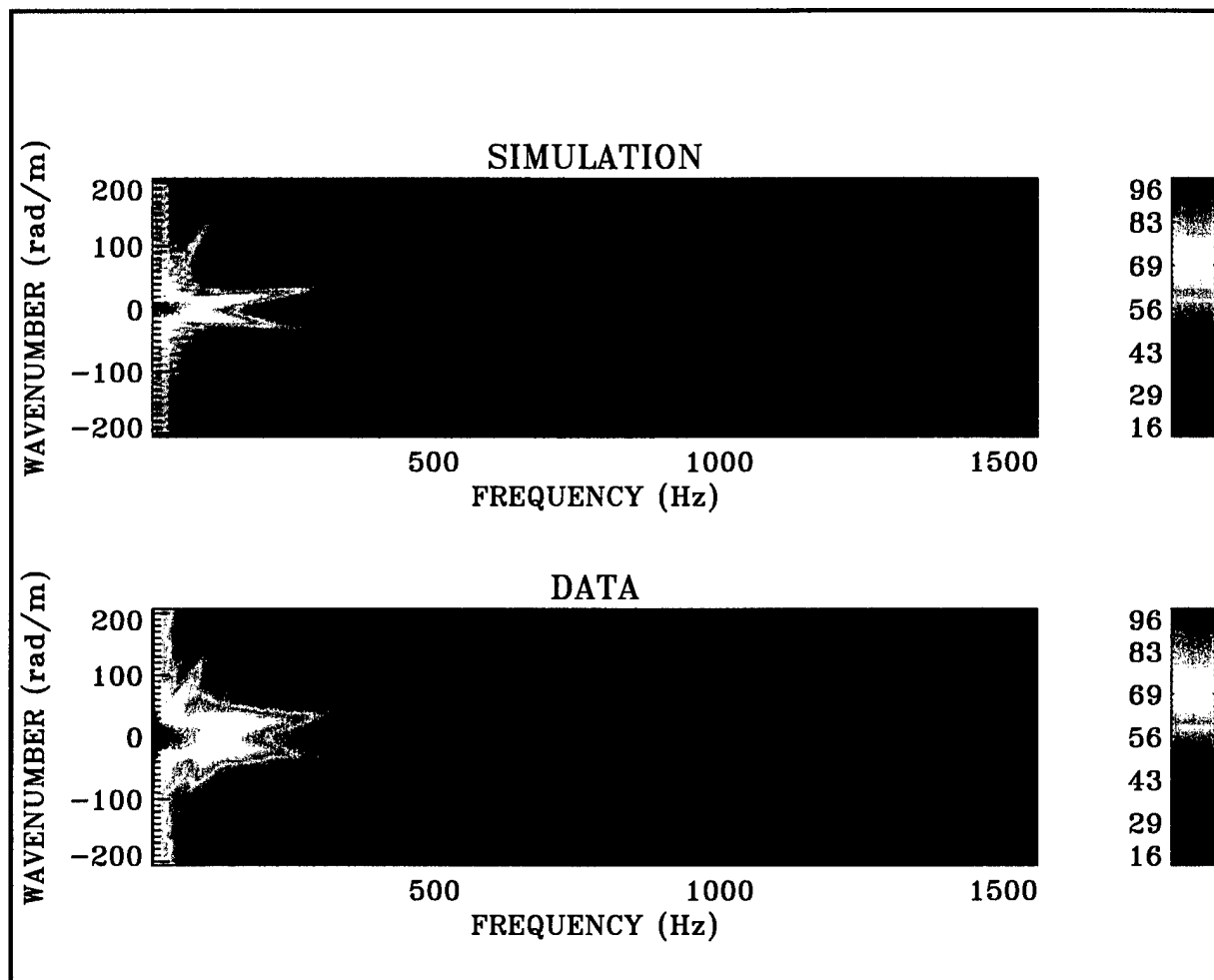


Figure 68. Comparison of Experimental Data $P_i(k, \omega)$ and Model Simulation Using a Wall Pressure Excitation at a Flow Speed of 4.9 m/sec

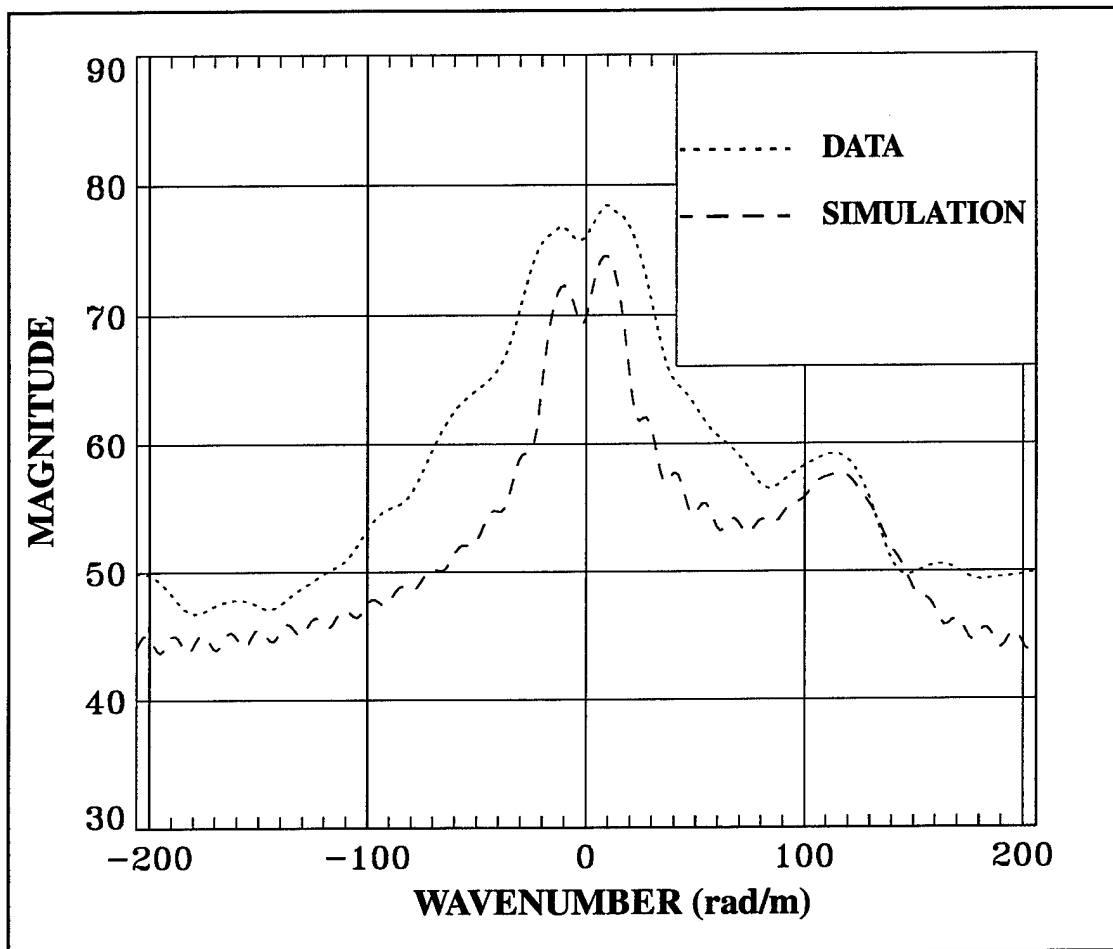


Figure 69. Comparison of Levels in Figure 68 at 84 Hz and a Flow Speed of 4.9 m/sec
 (Magnitude = $10 \log(P_i(k, \omega)^2)$ re $\mu Pa^2/Hz/rad/m$)

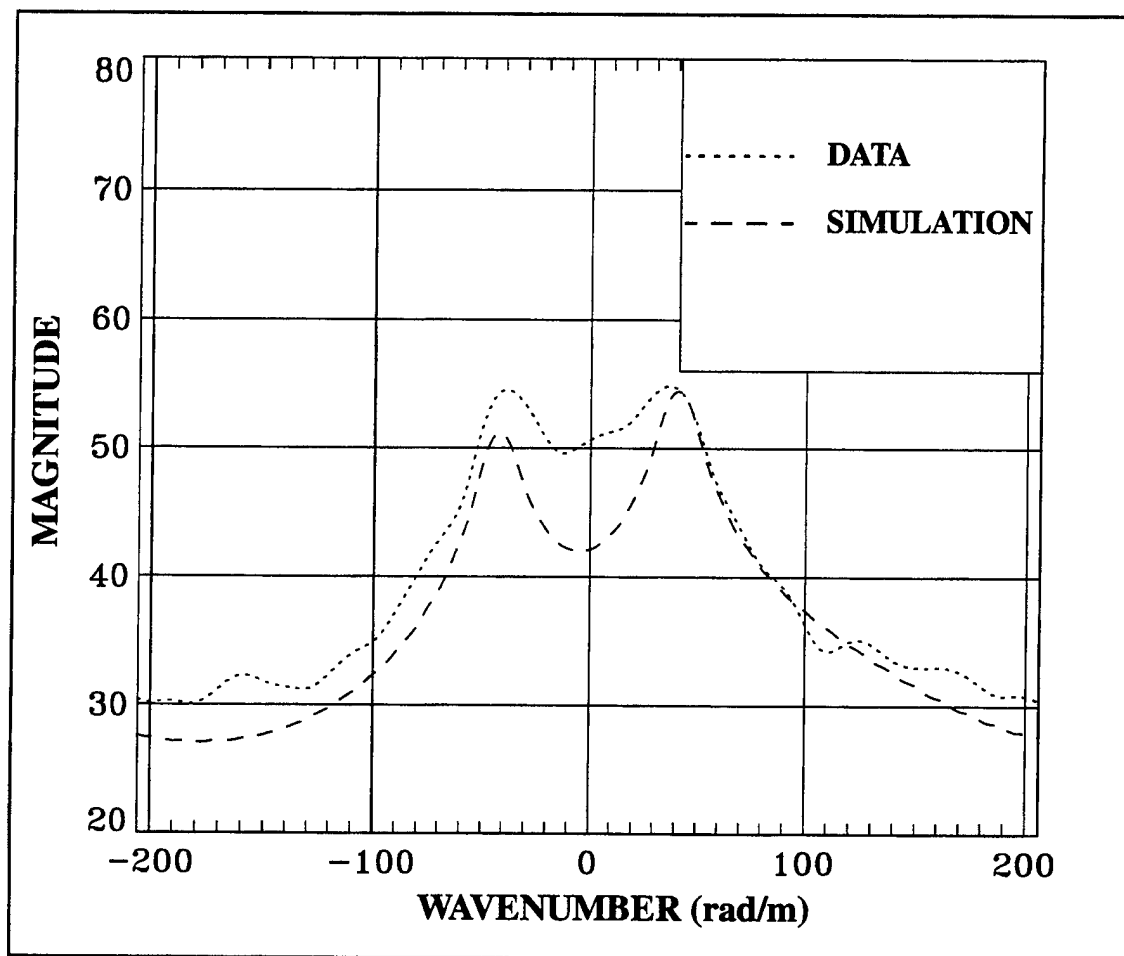


Figure 70. Comparison of Levels in Figure 68 at 345 Hz and a Flow Speed of 4.9 m/sec
(Magnitude = $10 \log(P_i(k, \omega)^2)$ re $\mu\text{Pa}^2/\text{Hz}/\text{rad}/\text{m}$)

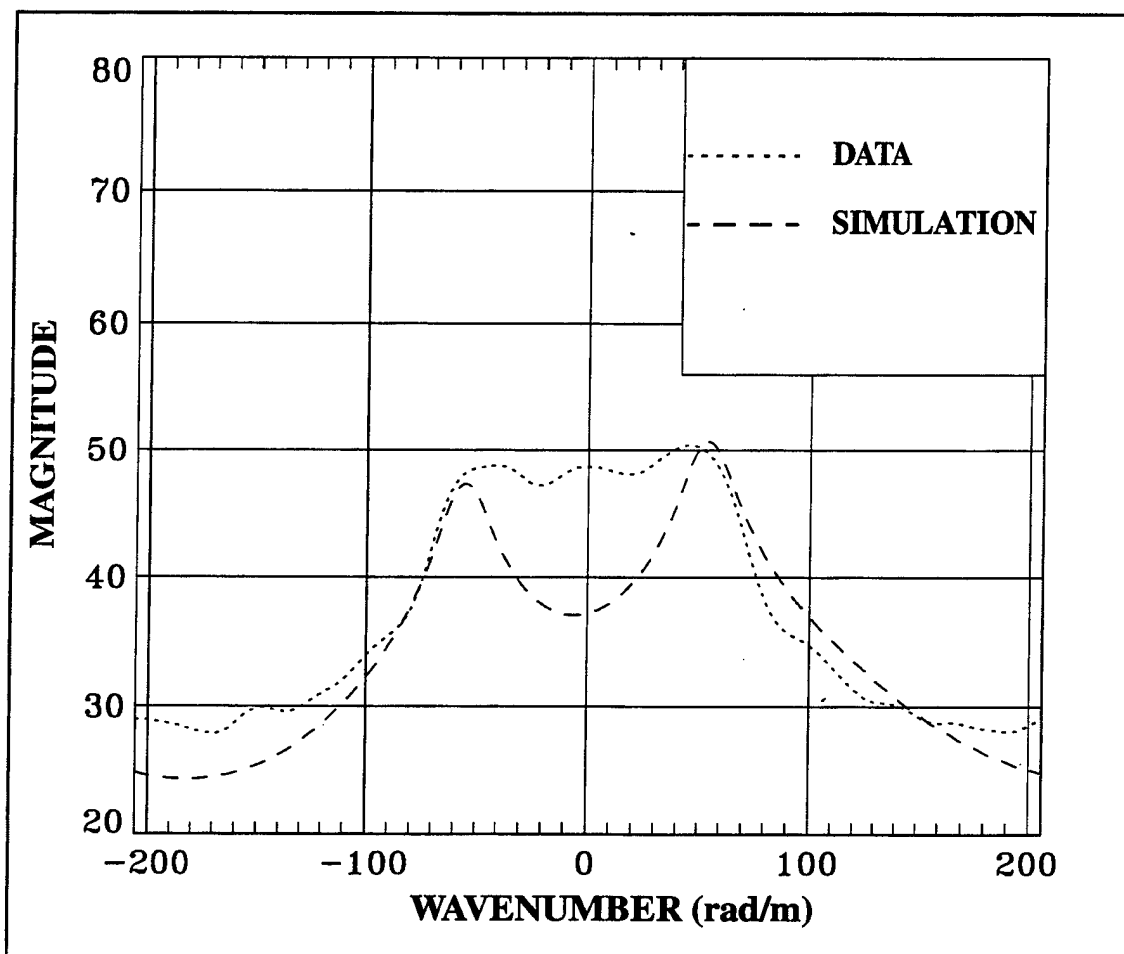


Figure 71. Comparison of Levels in Figure 68 at 445 Hz and a Flow Speed of 4.9 m/sec
 (Magnitude = $10 \log(P_i(k, \omega)^2)$ re $\mu\text{Pa}^2/\text{Hz}/\text{rad}/\text{m}$)

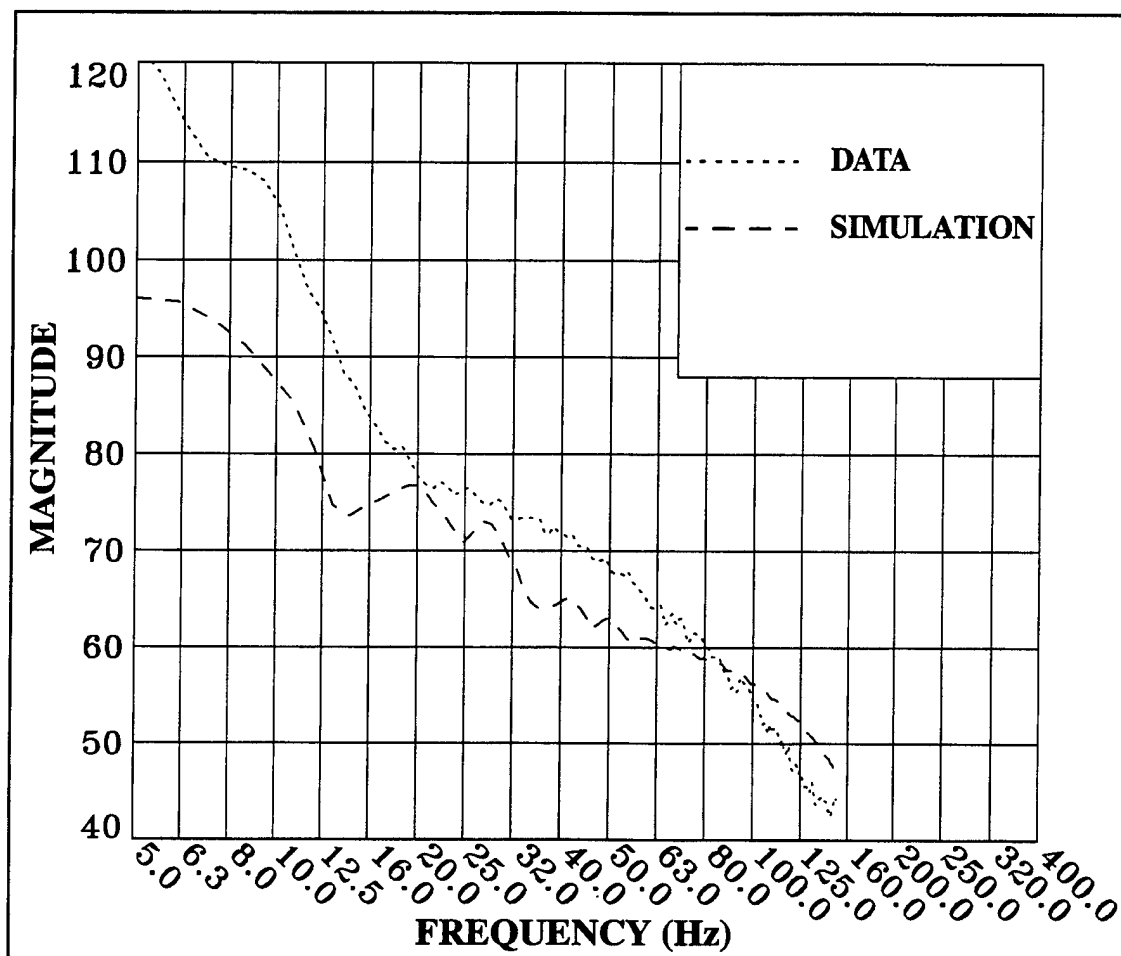


Figure 72. Convective Ridge Magnitude Comparison of Experimental Data and Bending Shell Model Simulation from Figure 68 at a Convective Velocity of 4.5 m/sec (Magnitude = $10 \log(P_i(k, \omega)^2)$ re $\mu Pa^2/Hz/rad/m$)

Shear Stress Excitation. The longitudinal shear stress comparison for the 10-knot flow speed is shown in figure 73. A cut at 445 Hz is made through the images of figure 73 and then displayed in figure 74. The magnitude of the convective ridge from the images of figure 73 is compared in figure 75 for a convective velocity of 4.5 m/sec. Both of these comparisons clearly illustrate how far down the convective contribution from the longitudinal shear stress is at this flow speed. The longitudinal shear stress thus contributes an insignificant amount of energy to the measured convective ridge level. For all practical purposes, the measured convective ridge level can be assumed to arise totally from the TBL wall pressure.

In figure 76, a comparison is made of the magnitude of the pressure spectra along the extensional wave velocity of 775 m/sec. At this flow speed, the extensional wave magnitude predicted by theory is barely equivalent to the experimentally measured level. The acoustic energy is evident, as well as its associated tonal quality.

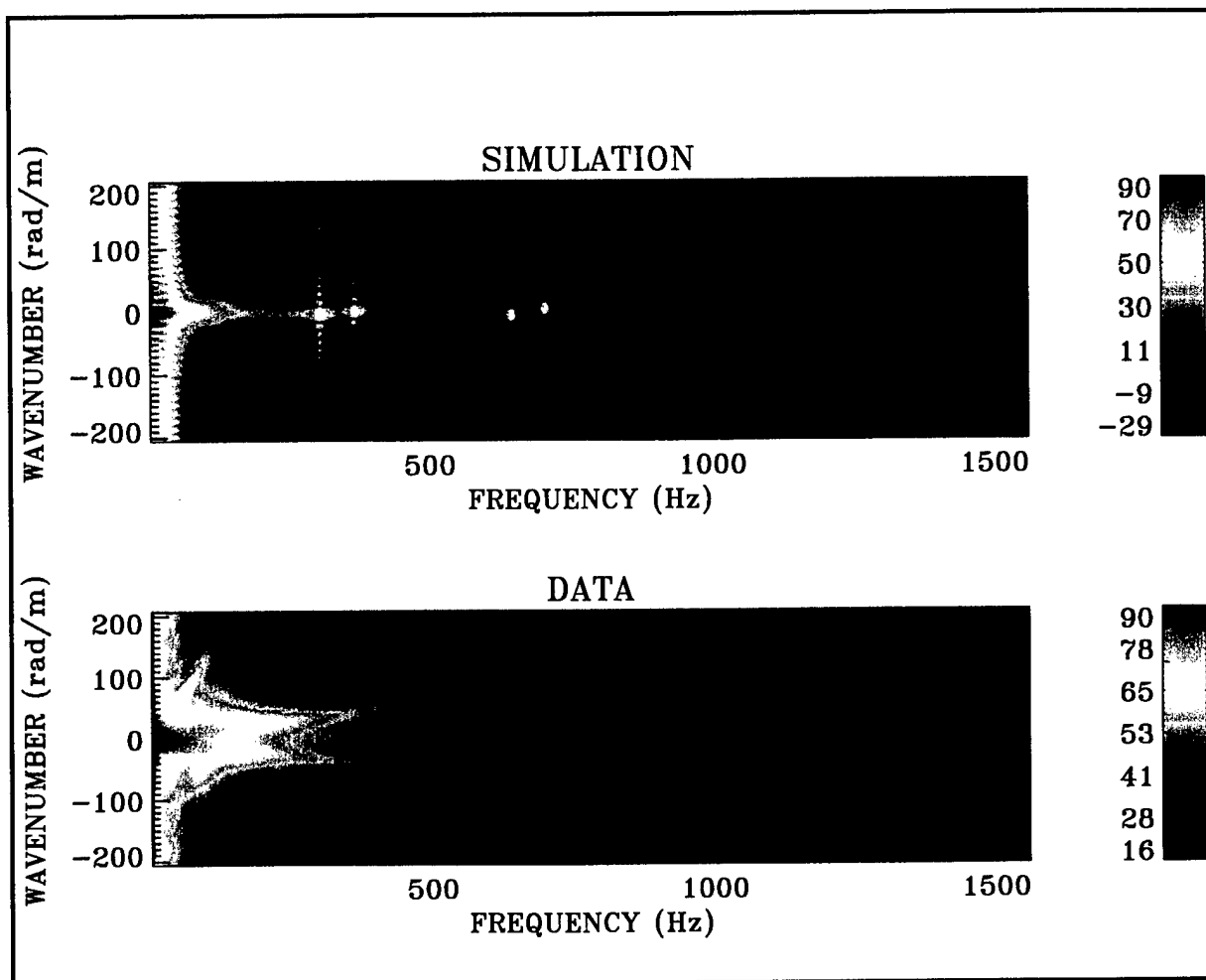


Figure 73. Comparison of Experimental Data $P_i(k, \omega)$ and Model Simulation Using a Longitudinal Shear Stress Excitation at a Flow Speed of 4.9 m/sec

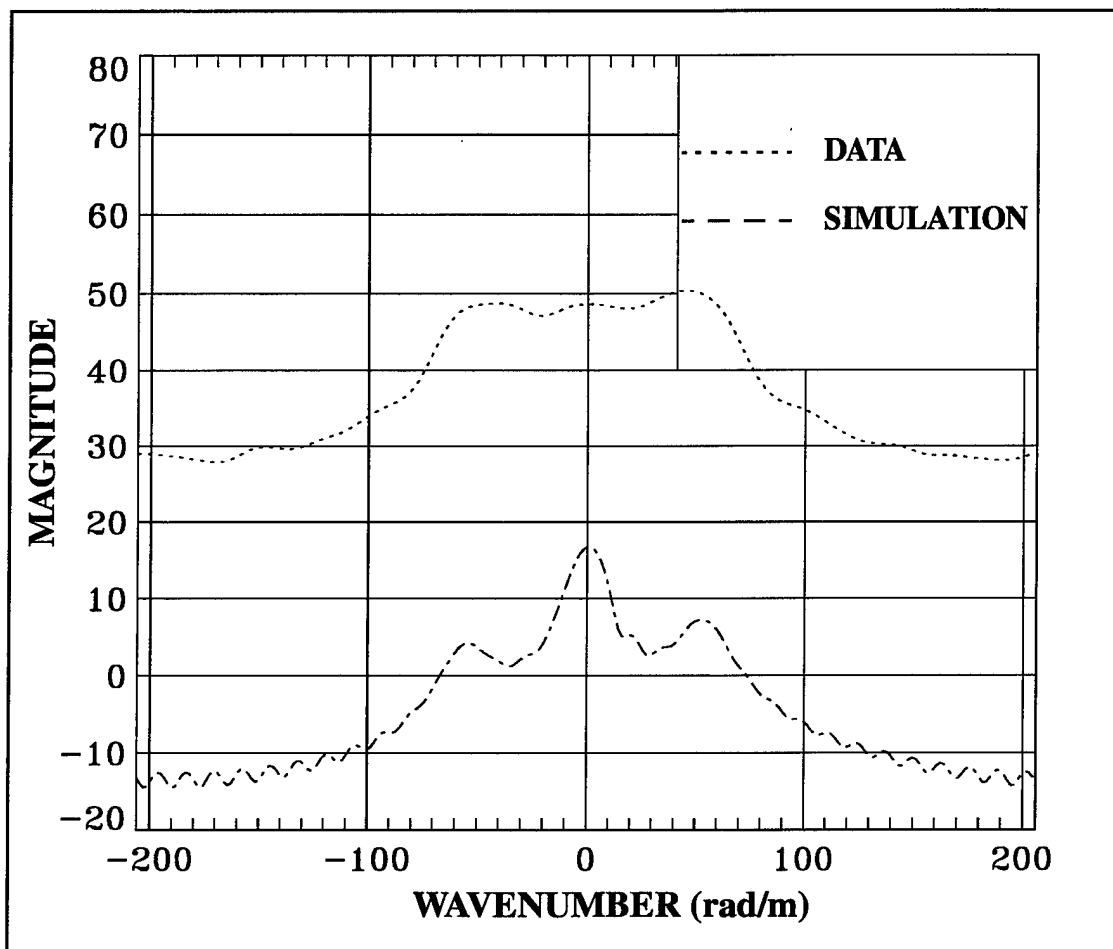


Figure 74. Comparison of Levels in Figure 73 at 445 Hz and a Flow Speed of 4.9 m/sec
 (Magnitude = $10 \log(P_f(k, \omega)^2)$ re $\mu\text{Pa}^2/\text{Hz}/\text{rad}/\text{m}$)

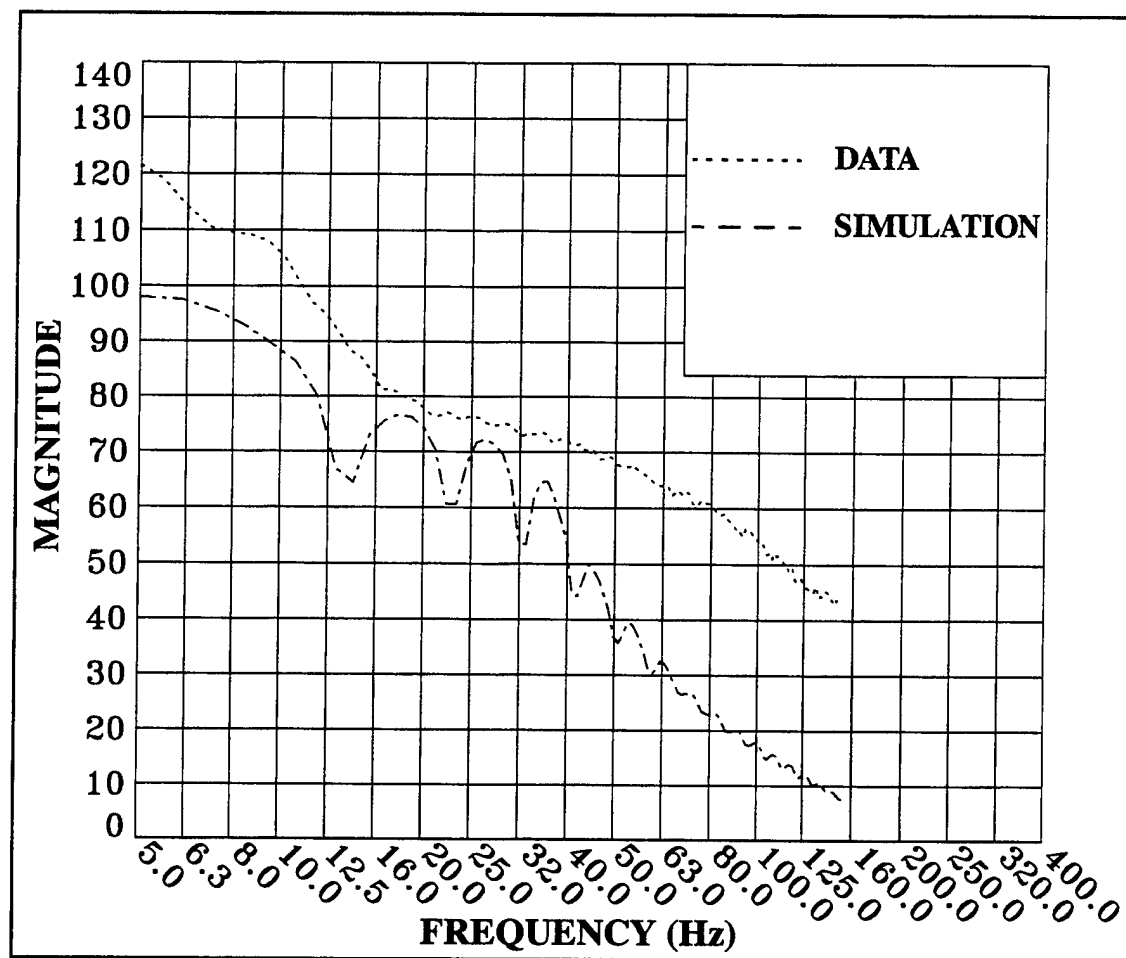


Figure 75. Convective Ridge Magnitude Comparison of Experimental Data and Bending Shell Model Simulation from Figure 73 at a Convective Velocity of 4.5 m/sec (Magnitude = $10 \log(P_i(k, \omega)^2)$ re $\mu\text{Pa}^2/\text{Hz}/\text{rad}/\text{m}$)

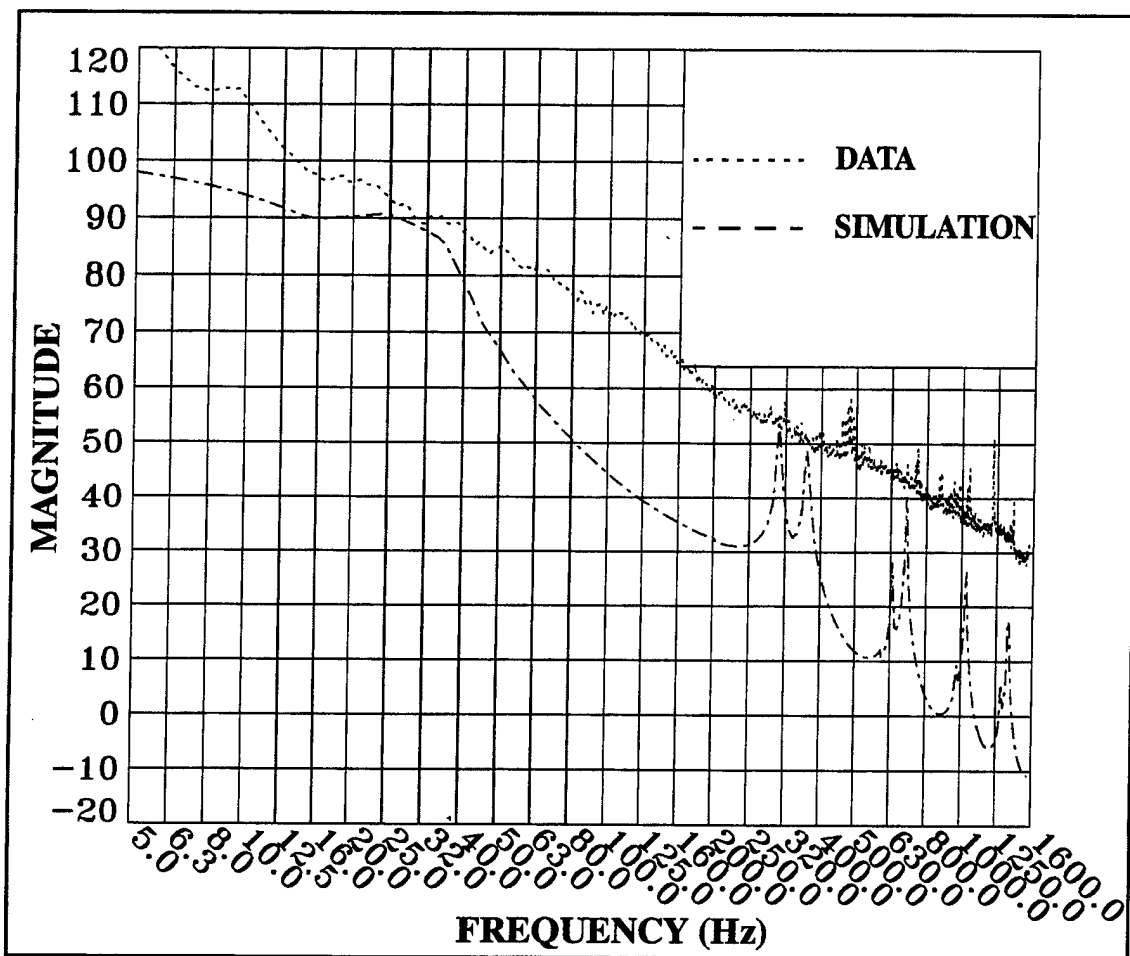


Figure 76. Extensional Wave Magnitude Comparison of Experimental Data and Bending Shell Model Simulation from Figure 73 with a Beam Cut at 775 m/sec (Magnitude = $10 \log(P_i(k, \omega)^2)$ re $\mu\text{Pa}^2/\text{Hz}/\text{rad}/\text{m}$)

5-Knot Freestream Velocity

Wall Pressure Excitation. In figure 77, which is a comparison between theory and experimental data at a 5-knot flow speed, the simulation is displayed as the upper image and the corresponding experimental data as the lower image. There is a slight trace of a convective ridge in the experimental data at this flow speed. Comparison cuts made between the figures at 117, 245, 345, and 445 Hz are plotted in figures 78, 79, 80, and 81, respectively.

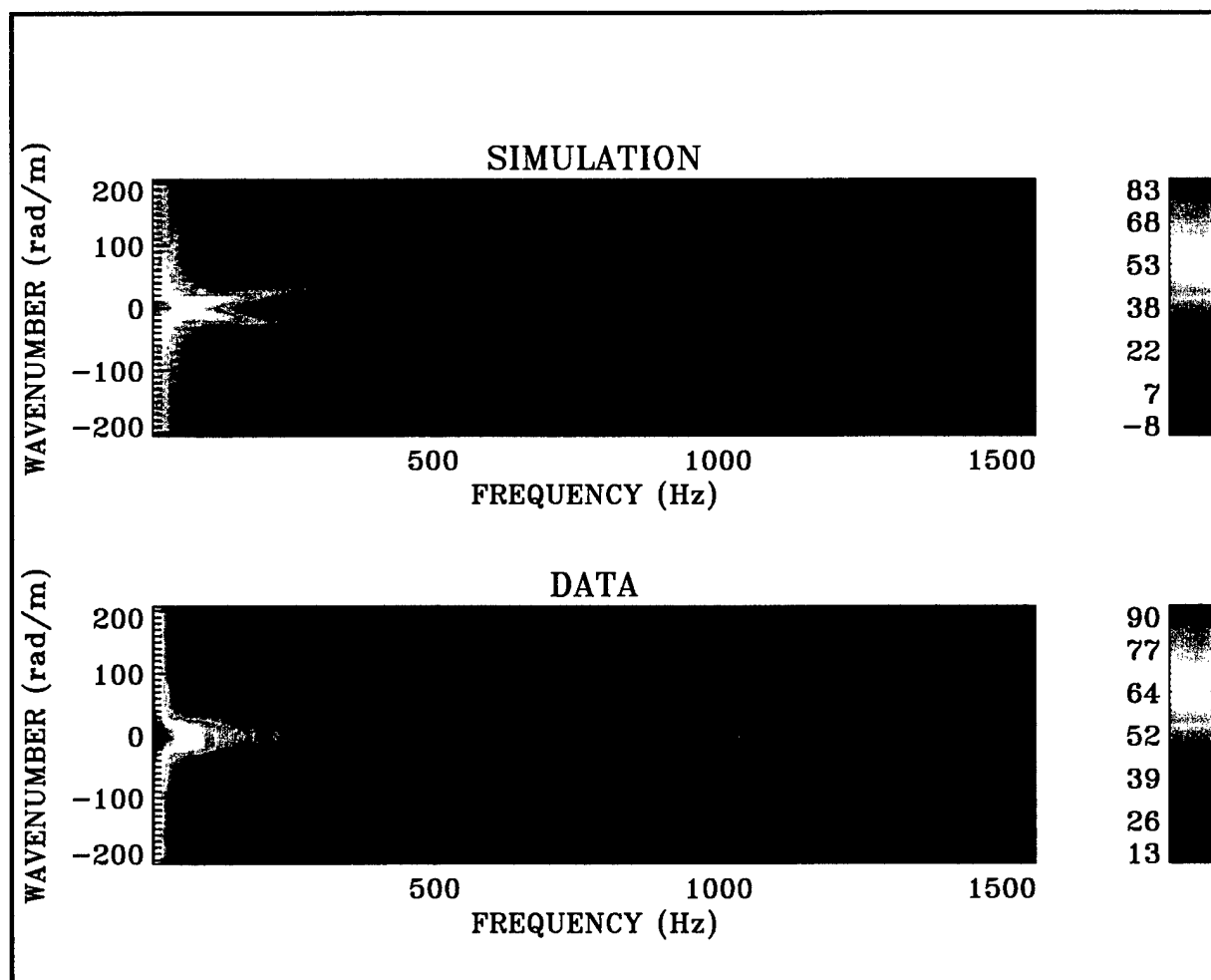


Figure 77. Comparison of Experimental Data $P_i(k, \omega)$ and Model Simulation Using a Wall Pressure Excitation at a Flow Speed of 2.5 m/sec

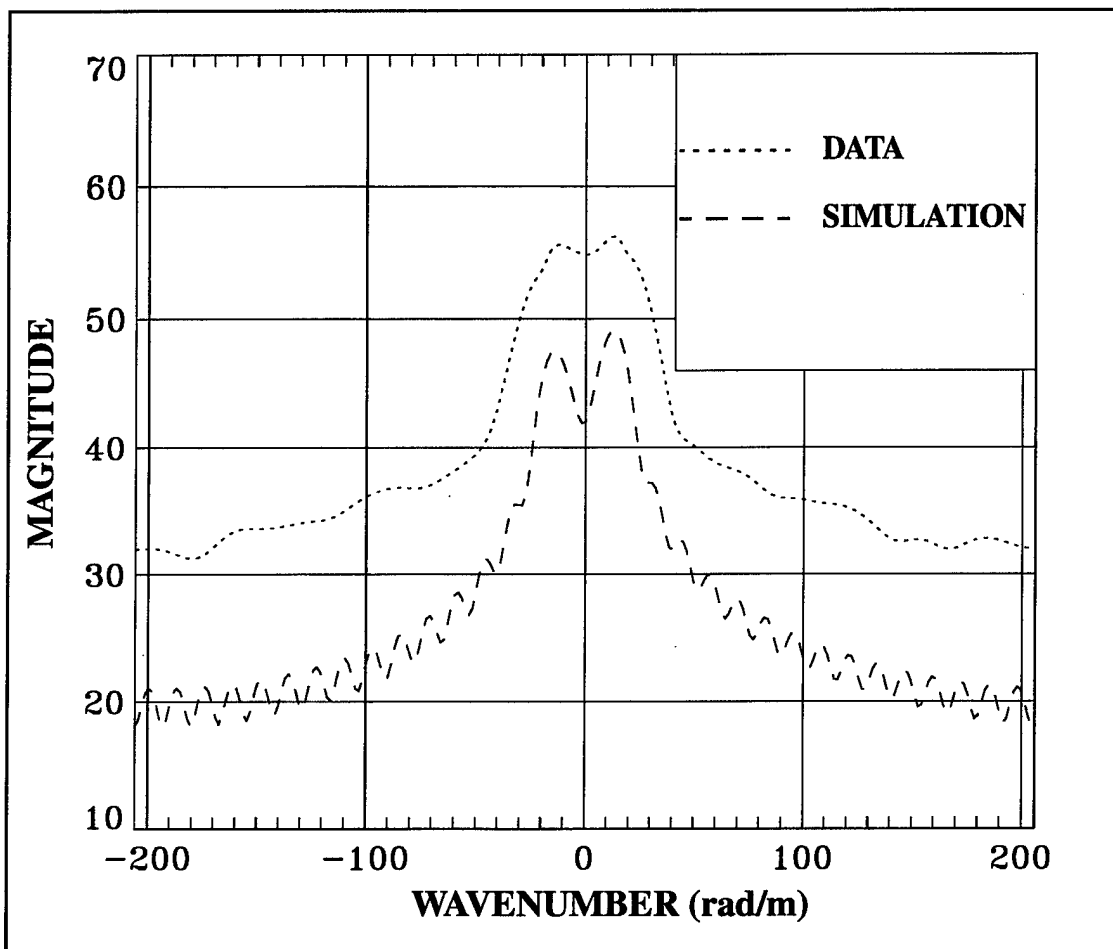


Figure 78. Comparison of Levels in Figure 77 at 117 Hz and a Flow Speed of 2.5 m/sec
 (Magnitude = $10 \log(P_f(k, \omega)^2)$ re $\mu\text{Pa}^2/\text{Hz}/\text{rad}/\text{m}$)

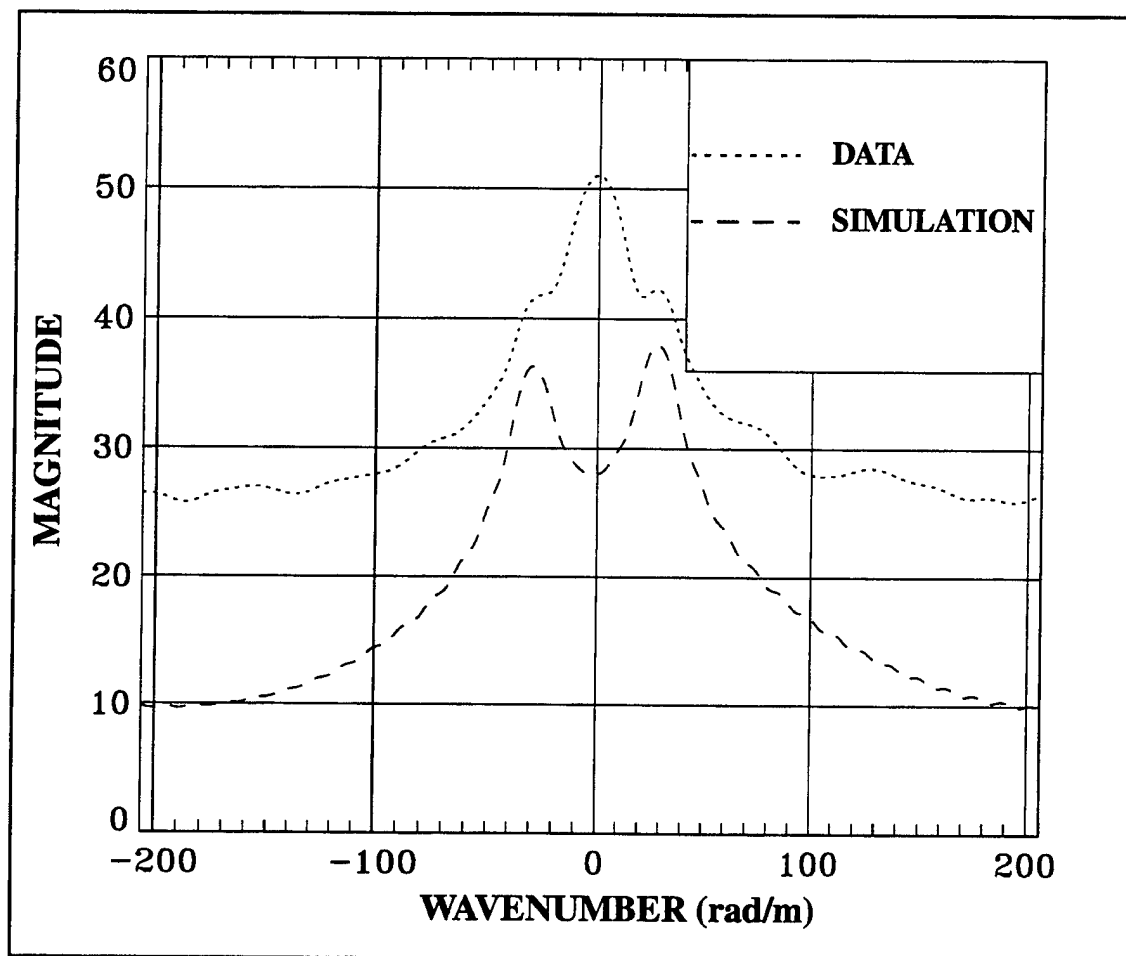


Figure 79. Comparison of Levels in Figure 77 at 245 Hz and a Flow Speed of 2.5 m/sec
 (Magnitude = $10 \log(P_i(k, \omega)^2)$ re $\mu\text{Pa}^2/\text{Hz}/\text{rad}/\text{m}$)

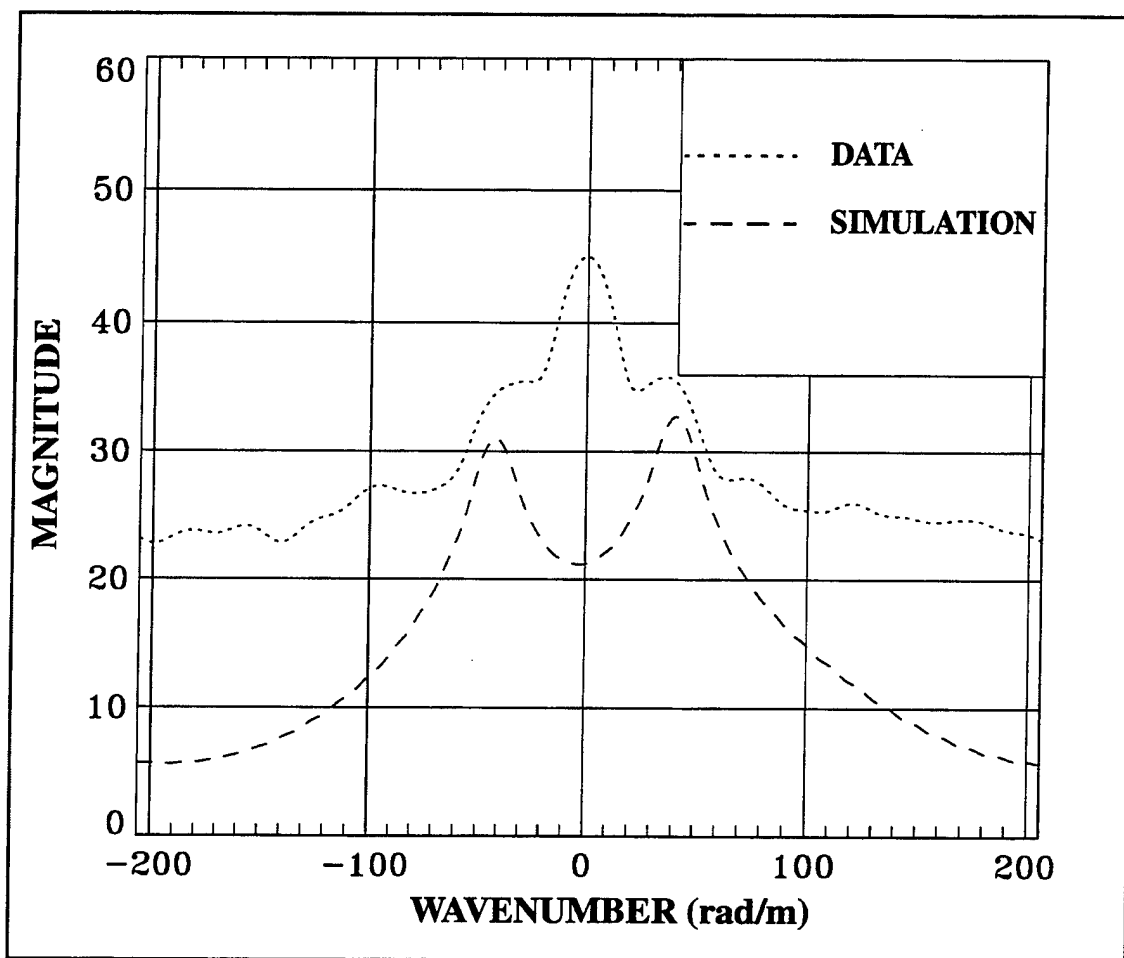


Figure 80. Comparison of Levels in Figure 77 at 345 Hz and a Flow Speed of 2.5 m/sec
 (Magnitude = $10 \log(P_i(k, \omega)^2)$ re $\mu\text{Pa}^2/\text{Hz}/\text{rad}/\text{m}$)

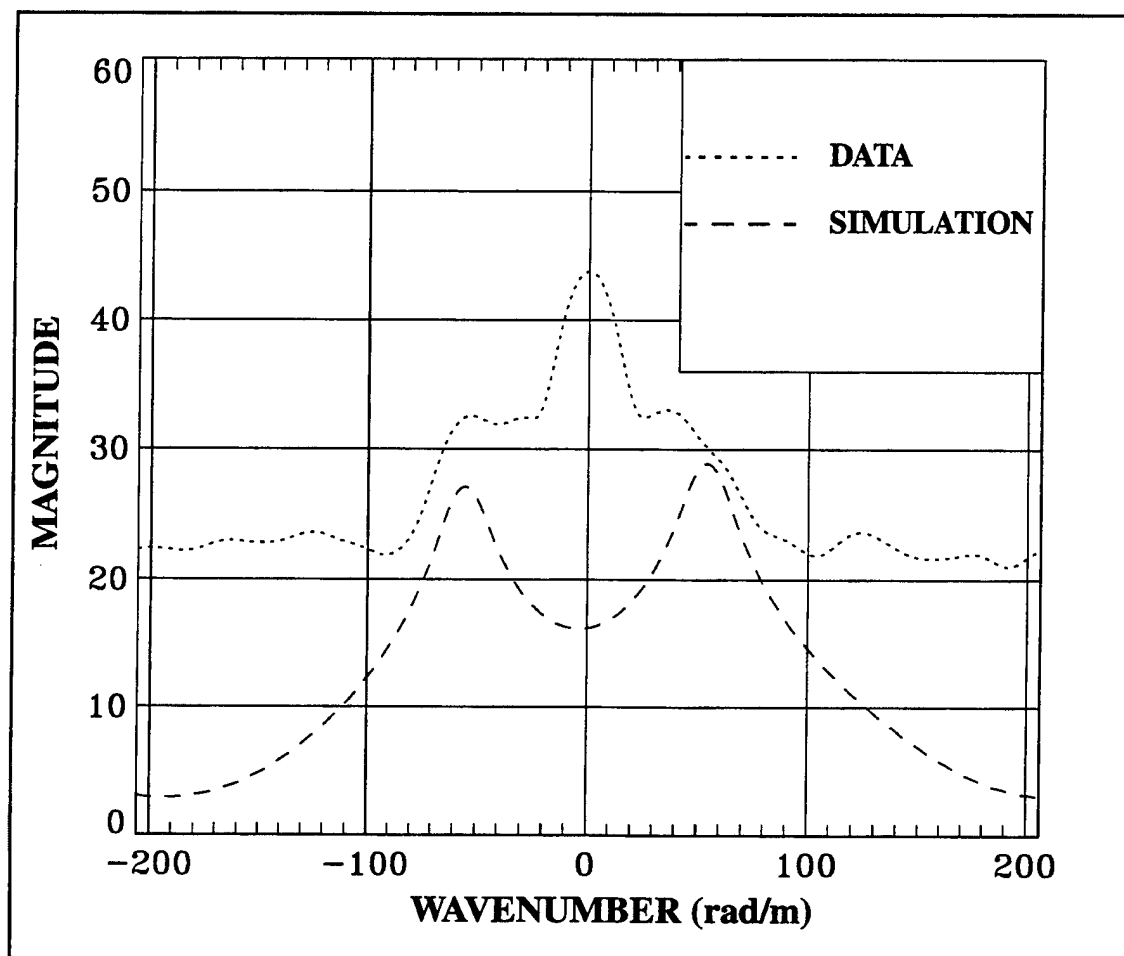


Figure 81. Comparison of Levels in Figure 77 at 445 Hz and a Flow Speed of 2.5 m/sec
(Magnitude = $10 \log(P_f(k, \omega)^2)$ re $\mu\text{Pa}^2/\text{Hz}/\text{rad}/\text{m}$)

Shear Stress Excitation. The longitudinal wall shear stress comparison for the 5-knot flow speed is shown in figure 82. A cut at 445 Hz is made through the images of figure 82 and then displayed in figure 83. Although there is a significant discrepancy between the levels of the experiment and prediction, their character is similar. Note also that the convective ridge has disappeared from both the measured data and the theoretical predictions, being attenuated by the OFC hose wall transfer function.

In figure 84, a comparison is made of the magnitude of the pressure spectra along the convective ridge at a convective velocity of 2.3 m/sec. Figure 85 compares the magnitude of the pressure spectra along the extensional wave velocity of 775 m/sec. At this 5-knot flow speed, the extensional wave magnitude predicted by theory is barely equivalent to the experimentally measured level. The acoustic energy is evident, as well as its associated tonal quality, in figure 82.

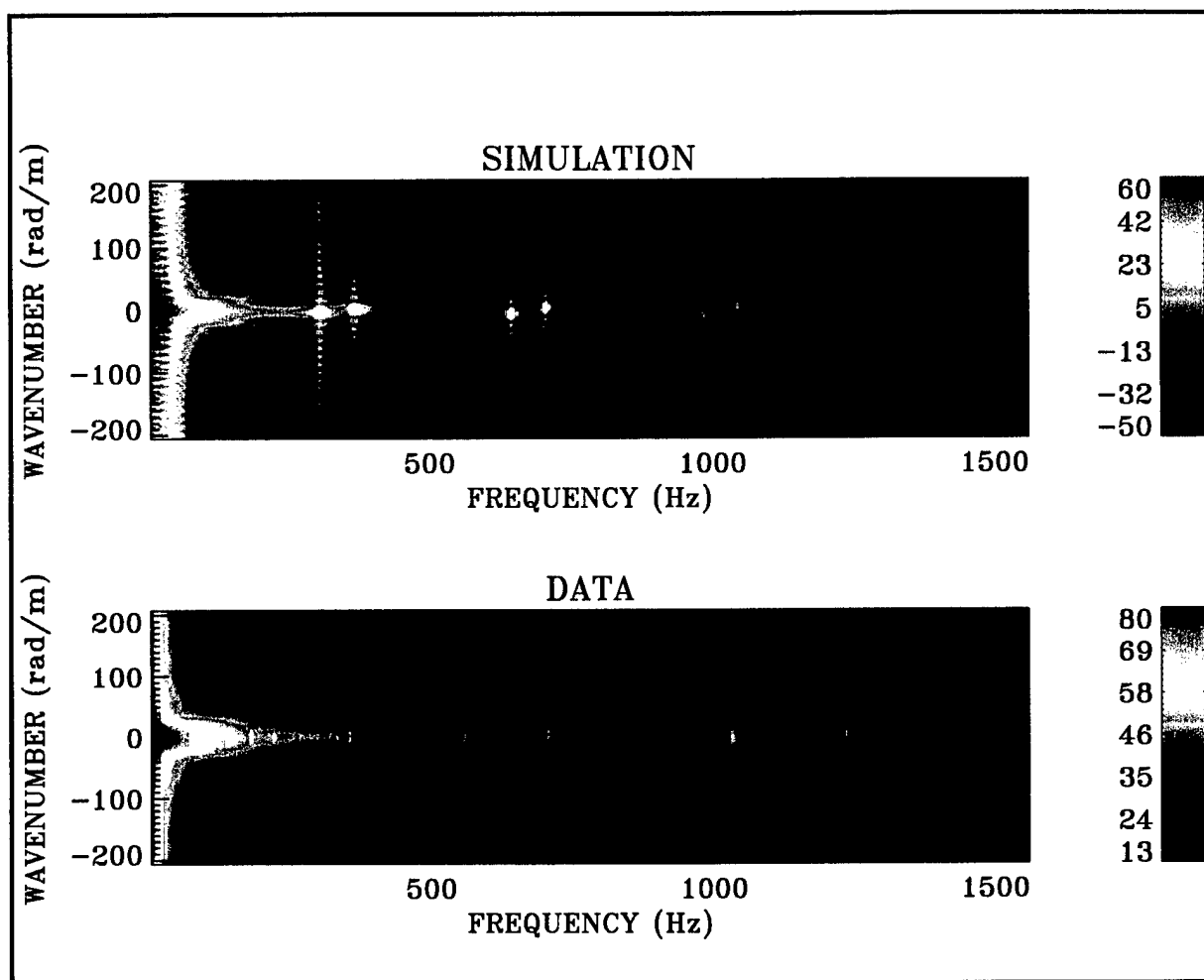


Figure 82. Comparison of Experimental Data $P_i(k, \omega)$ and Model Simulation Using a Longitudinal Shear Stress Excitation at a Flow Speed of 2.5 m/sec

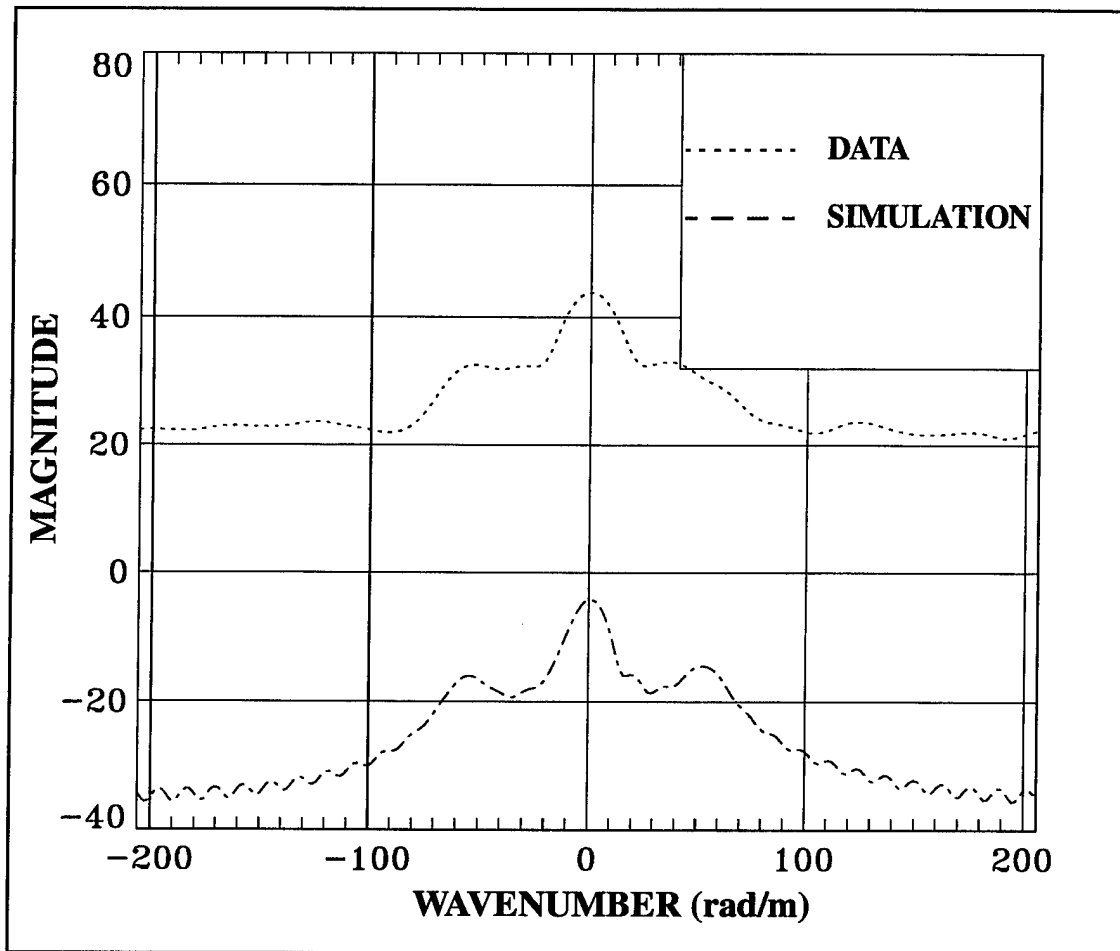


Figure 83. Comparison of Levels in Figure 82 at 445 Hz and a Flow Speed of 2.5 m/sec
 (Magnitude = $10 \log(P_i(k, \omega)^2)$ re $\mu\text{Pa}^2/\text{Hz}/\text{rad}/\text{m}$)

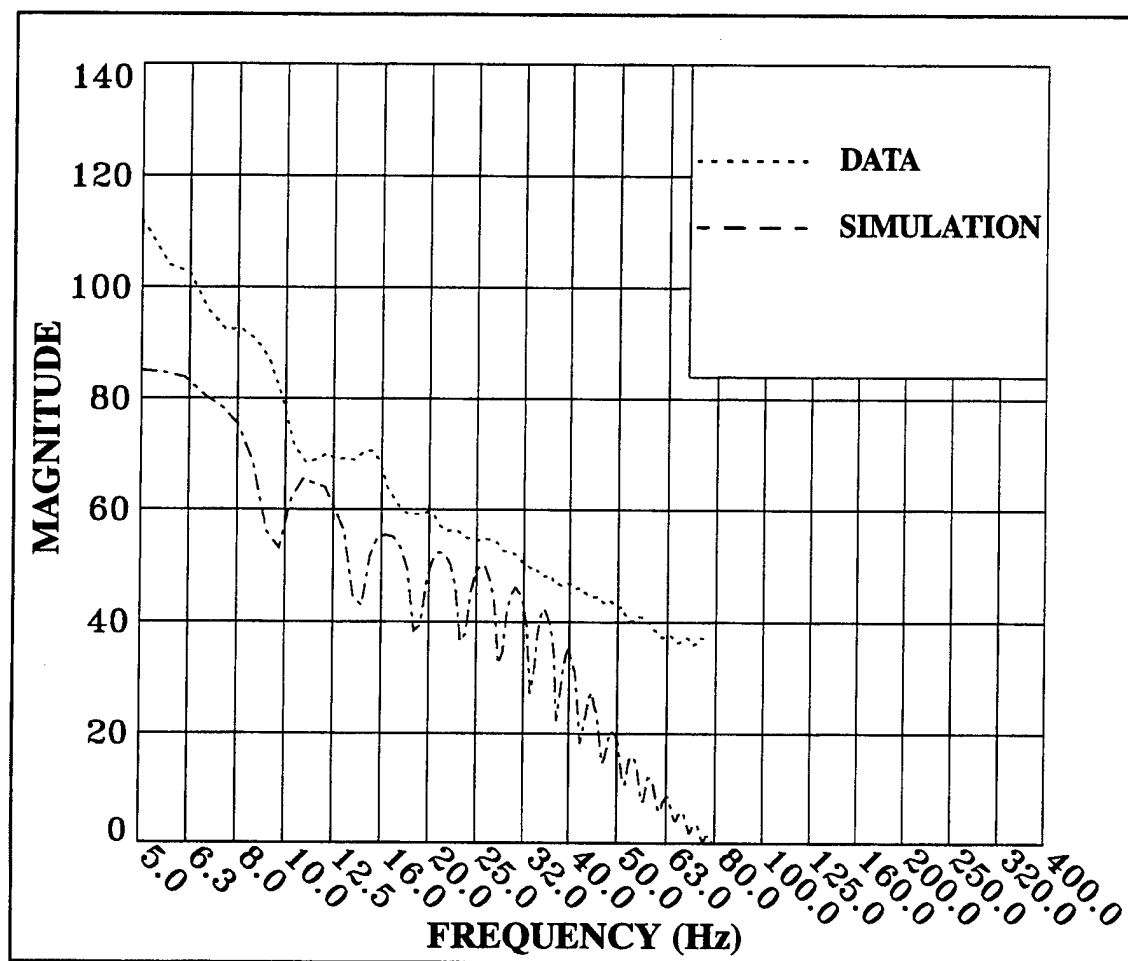


Figure 84. Convective Ridge Magnitude Comparison of Experimental Data and Bending Shell Model Simulation from Figure 82 at a Convective Velocity of 2.3 m/sec (Magnitude = $10 \log(P_i(k, \omega)^2)$ re $\mu\text{Pa}^2/\text{Hz}/\text{rad}/\text{m}$)

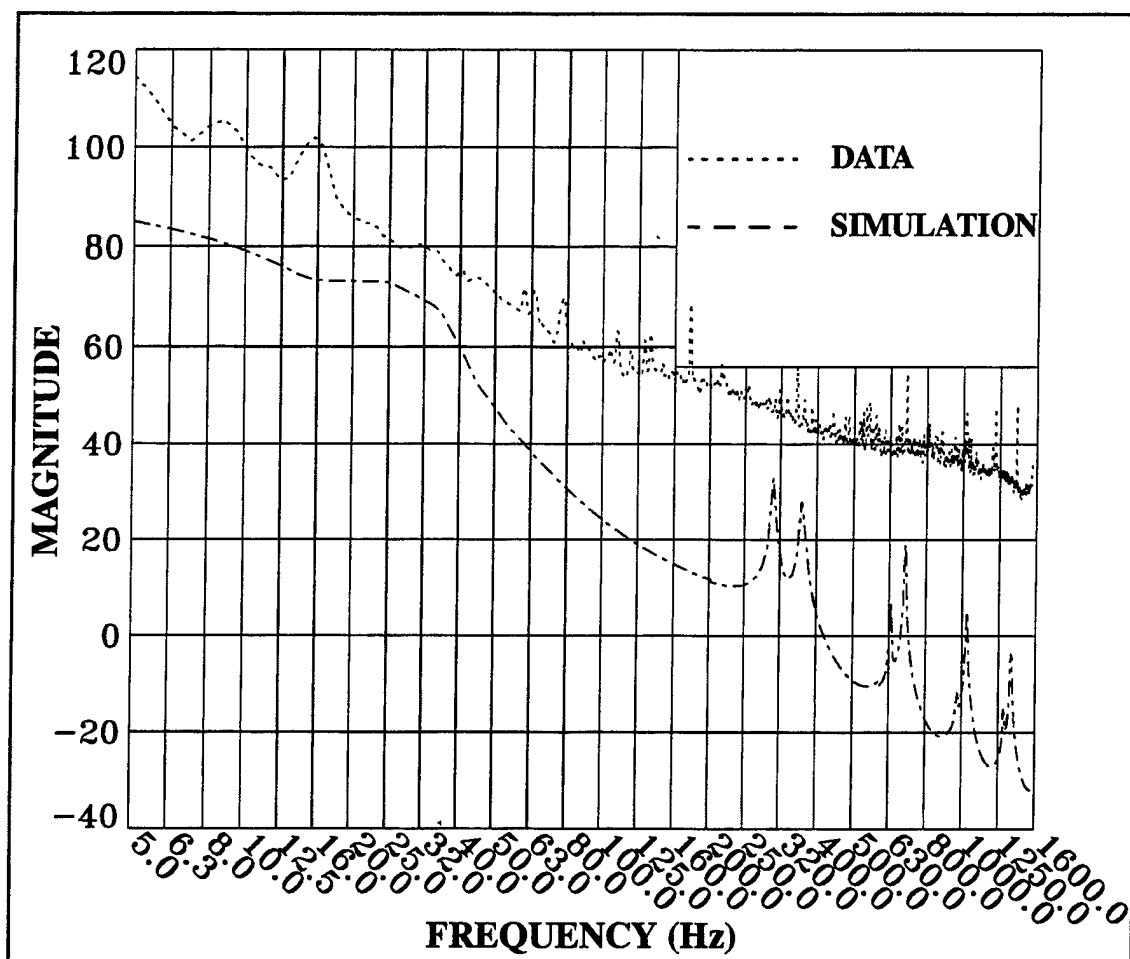


Figure 85. Extensional Wave Magnitude Comparison of Experimental Data and Bending Shell Model Simulation from Figure 82 with a Beam Cut at 775 m/sec (Magnitude = $10 \log(P_i(k, \omega)^2)$ re $\mu\text{Pa}^2/\text{Hz}/\text{rad}/\text{m}$)

CONCLUSIONS

Both ABC and OFC structures have been used with multichannel arrays to measure the wall pressure spectra beneath a cylindrical TBL. These measurements have spanned the wavenumber spectrum over the ± 206 -rad/m range and have included measurements at $k = 0$ that are free from acoustic contamination. The successful design of these experiments has required that careful attention be given to the response of the ABC to both radial (wall pressure) and longitudinal shear stress excitations.

Calibration of the ABC involves both the traditional frequency calibration in an acoustic field (low wavenumber) and a full-field calibration (k - ω) to account for the nonflat character of the ABC response from low to high wavenumbers. The high-wavenumber, full-field calibration is important because disregarding the nonflat structure response would introduce error into the estimation of the wall pressure in the vicinity of the convective ridge, which is, for the most part, a high-wavenumber feature of the k - ω plane. Since, at the present time, the state of the art does not include a broadband spatially harmonic wavenumber generator, the full-field calibration had to be implemented as a theoretical dynamic elasticity model simulation.

Calibration of the OFC hose wall transfer function is accomplished with experimental wall pressure data from both the OFC and the ABC. Theoretical dynamic elasticity simulations are required to assist in the calibration of the ABC data as previously discussed and to remove the effects of the surface-generated pressure fields, which, although different for each structure, will not simply cancel each other out.

The ABC array is sensitive to two components of the TBL wall stress field. From a freestream velocity of 10 knots and above, the ABC array produces a direct measurement of the convective ridge wall pressure spectra. Below a freestream velocity of 10 knots, however, the output of the ABC array is due to the longitudinal shear component of the TBL wall stress spectra.

Experimental data from the air-backed array, figures 37 through 40, reveal the asymmetric nature of the convective ridge with respect to wavenumber. At flow speeds of 5 and 10 knots (figures 37 and 38), the width of the mainlobe of the ABC array does not limit the resolution of the convective ridge, allowing the shape of the ridge to be accurately seen. However, at freestream velocities of 15 and 20 knots (figures 39 and 40), where wavenumber resolution is limited by the width of the mainlobe, the low-wavenumber side of the ridge steepens such that the true slope of the low-wavenumber side of the ridge is not visible.

Because the ABC array output was calibrated to normal (wall) pressure, only these values are compared to theoretical predictions for both wall pressure and wall shear stress. Current models for the TBL wall pressure spectra underpredict the convective ridge level at a 20-knot freestream flow speed (figure 44) by about 6 dB. This underprediction decreases to 3 dB at 10 knots (figure 49). A reversal then occurs at a freestream velocity of 5 knots, where the predicted wall pressure exceeds the actual level of the convective ridge. The amount of overprediction remains unknown, although a suggestion for determining the correct level at 5 knots is made in the report.

Past research has shown that the magnitude of the wall shear stress surface is less than the magnitude of the wall pressure surface by approximately 18 dB for moderate to high wavenumbers. This expectation holds for the 10- to 20-knot freestream flow speed region, but seems to reverse itself at a freestream flow speed of 5 knots, as shown in figure 57, where the longitudinal shear stress component is dominant over the wall pressure component. Although it is not possible to infer absolute values for longitudinal shear stress from the ABC data because the air-backed array output has not been calibrated for longitudinal shear excitation, this reversal at 5 knots does indicate that the theoretical prediction for wall pressure is greater than the actual level by some undetermined amount. However, since the longitudinal shear levels have exceeded the wall pressure levels at 5 knots, the amount of wall pressure overprediction by the model cannot be determined.

Comparisons between the OFC data and theoretical model simulations were within 0 to 4 dB in the region of the breathing wave peaks. The shape of the rolloff following the peaks for the model was a very precise match to that of the experiment. Incorporation of the changes

suggested by the ABC measurements into the TBL wall pressure model promises to produce even better agreement for the OFC comparisons.

RECOMMENDATIONS FOR FUTURE RESEARCH

More information could be obtained about the shape of the convective ridge by using experimental data from the medium- k wavenumber filter to resolve the sharpness of the low-wavenumber side of the ridge to a greater degree.* Low-wavenumber tones existing in the medium- k data (uncorrected for the hose wall transfer function) are sharper than the convective ridge, which leads to the supposition that the true shape of the convective ridge could likely be extracted from the experimental data after correction for the hose wall transfer function. However, there may be a limitation to this approach due to the double-peak phenomena, which could cast doubt on exactly what was measured with the medium- k filter. The medium- k convective ridge data would need to be compared with the high- k data to achieve some degree of confidence in the measurement. Another method for acquiring additional information on the ridge would be to perform the shift applied to figures 18 through 20 on the calibrated ABC data to double their useful frequency range.

Information on the absolute value of the longitudinal shear stress levels could be obtained by calibrating the response of the ABC data to longitudinal shear stress and then comparing this response to theoretical predictions. The calibration can be obtained most efficiently with the dynamic elasticity models used previously for the full-field calibration of the wall pressure. This suggestion should improve the understanding of the relationship between the wall pressure and longitudinal shear stress levels as a function of freestream flow speed in light of the reversal earlier observed at 5 knots where the level of the longitudinal wall shear stress exceeded that of the wall pressure.

* The width in wavenumber is 4.14 rad/m for the medium- k filter, which gives it greater resolving power than the ABC filter at a width of 9.18 rad/m.

REFERENCES

1. M. S. Peloquin, "Composite Hydrophone Array Assembly and Shading," U.S. Patent 5,550,791, 27 August 1996.
2. M. S. Peloquin, "Forced Harmonic Vibration of the Generally Orthotropic Cylindrical Shell with Inner and Outer Fluid Loading," NUWC-NPT Technical Report 10,199, Naval Undersea Warfare Center Detachment, New London, CT, November 1992, p. 40.
3. M. S. Peloquin, "A Closed-Form Dynamic Elasticity Solution to the Fluid/Structure Interaction Problem of a Two-Layered Infinite Viscoelastic Cylinder with Inner and Outer Fluid Loading Subject to Forced Harmonic Excitation," NUWC-NPT Technical Report 11,067, Naval Undersea Warfare Center Detachment, New London, CT, 30 December 1995.
4. M. S. Peloquin, "A Measurement Calibration of the Transfer Function of a Compliant Fluid-Filled Cylinder," Patent Pending (Navy Case No. 78106, 1 June 1997).

APPENDIX A

FREQUENCY CALIBRATIONS

The hydrophone signal amplification path is shown in figure A-1, with the numerically labeled points corresponding to the column numbers in tables A-1 through A-4. Table A-1 lists the final calibration performed at Dodge Pond for the ABC array. The same array was calibrated again in the anechoic chamber at NUWC Division Newport, with the results presented in table A-2. Table A-3 shows the calibration for the OFC long, single-channel hydrophone used in the low-wavenumber measurements, and tables A-4 and A-5 list calibrations for the medium- k and high- k arrays, respectively. The measurements in these latter three tables were taken at Dodge Pond. All sensitivities are given in units of dB re 1 V/ μ Pa and gains are given in decibels (dB).

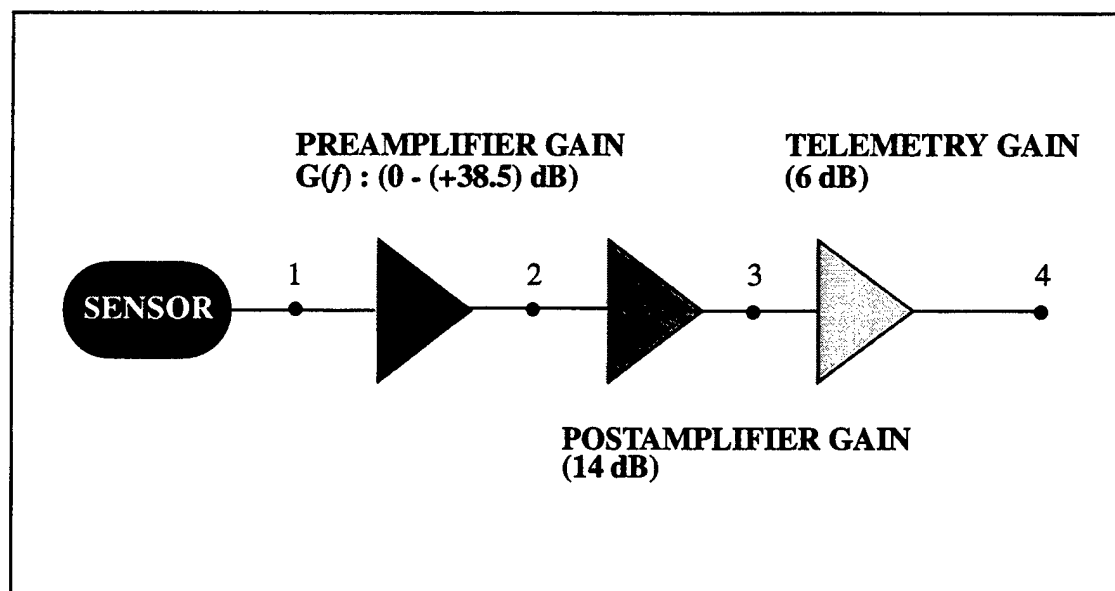


Figure A-1. Signal Amplification Diagram

Table A-1. ABC Calibrations at Dodge Pond

Hz	Raw ABC / Piezo Film Sensitivity 1	Array Sensitivity with Preamp (3/94) 2	Postamp and Telemetry Gain	Final Calibration 4
5.0	-	-216.6	+20.0	-196.6
6.3	-	-215.3	+20.0	-195.3
8.0	-	-213.5	+20.0	-193.5
10.0	-	-211.8	+20.0	-191.8
12.5	-	-210.8	+20.0	-190.8
16.0	-	-209.0	+20.0	-189.0
20.0	-	-207.0	+20.0	-187.0
25.0	-	-205.6	+20.0	-185.6
32.0	-	-204.5	+20.0	-184.5
40.0	-	-200.8	+20.0	-180.8
50.0	-	-197.9	+20.0	-177.9
63.0	-	-196.5	+20.0	-176.5
80.0	-	-195.4	+20.0	-175.4
100.0	-223.9	-194.2	+20.0	-174.2
125.0	-	-192.8	+20.0	-172.8
160.0	-	-192.4	+20.0	-172.4
200.0	-224.1	-190.5	+20.0	-170.5
250.0	-	-189.7	+20.0	-169.7
320.0	-	-189.3	+20.0	-169.3
400.0	-	-188.5	+20.0	-168.5
500.0	-225.9	-188.4	+20.0	-168.4
630.0	-	-188.4	+20.0	-168.4
800.0	-	-188.2	+20.0	-168.2
1000.0	-226.5	-188.0	+20.0	-168.0
1250.0	-	-188.2	+20.0	-168.2
1600.0	-	-188.3	+20.0	-168.3

Table A-2. ABC Calibrations in the Anechoic Chamber

Hz	Anechoic Chamber (7/8/97) 1	Array Sensitivity with Preamp (Table A-1) (3/94) 2
5.0	-	-216.6
6.3	-	-215.3
8.0	-	-213.5
10.0	-	-211.8
12.5	-	-210.8
16.0	-	-209.0
20.0	-	-207.0
25.0	-	-205.6
32.0	-	-204.5
40.0	-	-200.8
50.0	-	-197.9
63.0	-	-196.5
80.0	-	-195.4
100.0	-	-194.2
125.0	-	-192.8
160.0	-187.5	-192.4
200.0	-187.0	-190.5
250.0	-185.5	-189.7
320.0	-183.5	-189.3
400.0	-183.0	-188.5
500.0	-182.5	-188.4
630.0	-182.5	-188.4
800.0	-182.5	-188.2
1000.0	-182.5	-188.0
1250.0	-182.5	-188.2
1600.0	-182.5	-188.3

Table A-3. Calibrations of OFC Single-Channel Hydrophone (EDO) at Dodge Pond

Hz	Array Sensitivity with Preamp 2	Postamp Telemetry Gain (14 dB + 6 dB)	Final Calibration 4
5.0	-189.9	+20.0	-169.9
6.3	-188.1	+20.0	-168.1
8.0	-186.0	+20.0	-166.0
10.0	-184.2	+20.0	-164.2
12.5	-182.4	+20.0	-162.4
16.0	-180.3	+20.0	-160.3
20.0	-178.4	+20.0	-158.4
25.0	-176.6	+20.0	-156.6
32.0	-174.7	+20.0	-154.7
40.0	-172.7	+20.0	-152.7
50.0	-170.9	+20.0	-150.9
63.0	-169.0	+20.0	-149.0
80.0	-167.2	+20.0	-147.2
100.0	-165.5	+20.0	-145.5
125.0	-164.0	+20.0	-144.0
160.0	-162.3	+20.0	-142.3
200.0	-160.9	+20.0	-140.9
250.0	-159.5	+20.0	-139.5
320.0	-158.2	+20.0	-138.2
400.0	-157.1	+20.0	-137.1
500.0	-156.2	+20.0	-136.2
630.0	-155.7	+20.0	-135.7
800.0	-155.5	+20.0	-135.5
1000.0	-155.5	+20.0	-135.5
1250.0	-155.5	+20.0	-135.5
1600.0	-155.5	+20.0	-135.5

Table A-4. Calibrations of OFC Medium-k Array at Dodge Pond

Hz	Array Sensitivity with Preamp 2	Postamp Telemetry Gain (14 dB + 6 dB)	Final Calibration 4
5.0	-208.5	+20.0	-188.5
6.3	-206.7	+20.0	-186.7
8.0	-204.8	+20.0	-184.8
10.0	-203.0	+20.0	-183.0
12.5	-201.2	+20.0	-181.2
16.0	-199.2	+20.0	-179.2
20.0	-197.4	+20.0	-177.4
25.0	-195.6	+20.0	-175.6
32.0	-193.8	+20.0	-173.8
40.0	-191.9	+20.0	-171.9
50.0	-190.1	+20.0	-170.1
63.0	-188.3	+20.0	-168.3
80.0	-186.4	+20.0	-166.4
100.0	-184.6	+20.0	-164.6
125.0	-182.9	+20.0	-162.9
160.0	-181.0	+20.0	-161.0
200.0	-179.5	+20.0	-159.5
250.0	-178.1	+20.0	-158.1
320.0	-176.8	+20.0	-156.8
400.0	-175.8	+20.0	-155.8
500.0	-175.2	+20.0	-155.2
630.0	-175.0	+20.0	-155.0
800.0	-175.1	+20.0	-155.1
1000.0	-175.1	+20.0	-155.1
1250.0	-175.1	+20.0	-155.1
1600.0	-175.1	+20.0	-155.1

Table A-5. Calibrations of OFC High-k Array at Dodge Pond

Hz	Anechoic Chamber (7/8/97) 2	Array Sensitivity with Preamp (3/94) 2	Postamp Telemetry Gain (14 dB + 6 dB)	Final Calibration 4
5.0	-	-204.3	+20.0	-184.3
6.3	-	-202.6	+20.0	-182.6
8.0	-	-200.7	+20.0	-180.7
10.0	-	-199.0	+20.0	-179.0
12.5	-	-197.2	+20.0	-177.2
16.0	-	-195.3	+20.0	-175.3
20.0	-	-193.6	+20.0	-173.6
25.0	-	-191.9	+20.0	-171.9
32.0	-	-190.1	+20.0	-170.1
40.0	-	-188.2	+20.0	-168.2
50.0	-	-186.5	+20.0	-166.5
63.0	-	-183.7	+20.0	-163.7
80.0	-	-182.8	+20.0	-162.8
100.0	-183.0	-181.1	+20.0	-161.1
125.0	-	-179.4	+20.0	-159.4
160.0	-	-177.5	+20.0	-157.5
200.0	-178.0	-175.9	+20.0	-155.9
250.0	-177.5	-174.6	+20.0	-154.6
320.0	-176.5	-173.5	+20.0	-153.5
400.0	-176.0	-172.7	+20.0	-152.7
500.0	-175.0	-172.2	+20.0	-152.2
630.0	-174.0	-172.0	+20.0	-152.0
800.0	-173.0	-171.9	+20.0	-151.9
1000.0	-173.0	-171.9	+20.0	-151.9
1250.0	-173.0	-171.9	+20.0	-151.9
1600.0	-173.0	-171.9	+20.0	-151.9

APPENDIX B

WAVENUMBER CALIBRATIONS

Table B-1 shows the decrease in sensitivity between broadside and endfire for several frequencies. Table B-2 shows the decrease in sensitivity for a 35-degree acoustic plane wave arrival angle measured from broadside. Both sets of measurements were made for the ABC array in the NUWC Division Newport anechoic chamber, with all sensitivities given in dB re 1 V/ μ Pa.

Table B-1. Comparison of Endfire and Broadside Measurements in the Anechoic Chamber for the ABC Array

Hz	Broadside (7/8/97) 2	Air Endfire (7/8/97) 2	Decrease in Sensitivity at Endfire
800.0	-182.5	-190.0	-7.5
1000.0	-182.5	-188.0	-5.5
1250.0	-182.5	-188.0	-5.5
1600.0	-182.5	-189.0	-6.5

Table B-2. Sensitivity of an Acoustic Plane Wave Arrival Angle (35 degrees) Measured in the Anechoic Chamber for the ABC Array

Hz	Broadside (7/8/97) 2	Air 35 deg (7/8/97) 2	Decrease in Sensitivity at 35 deg
800.0	-182.5	-193.5	-11.0
1000.0	-182.5	-197.5	-15.0
1250.0	-182.5	-196.0	-13.5
1600.0	-182.5	-190	-7.5

INITIAL DISTRIBUTION LIST

Addressee	No. of Copies
Office of Naval Research (Code 321SS—K. Dial, D. Davison, J. Lindberg, R. Elswick)	4
Naval Sea Systems Command (PMS 425—CAPT T. O'Connor, J. Smerchansky, B. Kinsey, A. Karagiorgis, B. Alves; ASTO—J. Thompson, A. Hommel, C. Lim, J. Jones, R. Zarnich, M. Traweck)	11
Naval Surface Warfare Center, Carderock Division (T. Farabee)	1
Defense Technical Information Center	2
Mantech Applied Systems, Inc., New London, CT (B. Douglas)	1
Hauptmann Associates, Groton, CT (R. Hauptmann (2), J. Diggs)	3